PREDICTING THE THERMODYNAMIC PROPERTIES OF COMPLEX FLUIDS AND THEIR MIXTURES

By

Alyssa K. Nelson

Dissertation

Submitted to the Faculty of the

Graduate School of Vanderbilt University

in partial fulfillment of the requirements

for the degree of

DOCTOR OF PHILOSOPHY

in

CHEMICAL AND BIOMOLECULAR ENGINEERING

December 16, 2023

Nashville, Tennessee

Approved:

Clare M^{c}Cabe, Ph.D.

Peter Cummings, Ph.D.

Kane Jennings, Ph.D.

Paul Laibinis, Ph.D.

Shihong Lin, Ph.D.

Dedicated to my two grandmas, Naomi and Marsha,
who would've marveled in the completion of my Ph.D. and never hesitated to tell me how proud they were.

Acknowledgments

First, I would like to thank my Ph.D. advisor Dr. Clare McCabe who I appreciate immensely for her support, knowledge, encouragement, and expertise. Under her guidance I have become a true scientist, from her extensive feedback to ensure my presentations are always polished to her ideas always encouraging me to think outside the box, she has been a constant through a very unique Ph.D. process. Despite a pandemic and an international move, her support never wavered. I'll always value our lighthearted meetings and her encouragement of my independence and ownership over my work. I would also like to thank my committee members, Peter Cummings for his support and enthusiastic talks about theoretical methods and math, Kane Jennings for his encouragement and for always taking a personal interest in my work, Paul Laibinis for his mentorship, thoughtful questions, and inspiring dedication to educating undergraduates, and Shihong Lin for stepping outside his comfort zone and always bringing a unique perspective to my presentations. Finally, I would also like to thank the National Science Foundation for their support of my research under grant CBET-1805126.

Furthermore, my lab members, Justin Gilmer, Ray Matsumoto, Chloe Frame, and Co Quach, who have made this process especially enjoyable are so appreciated for their interest in my work, their endless support and assistance, and our long lunches to discuss science and life. I would further like to thank Yura Kalyuzhnyi for his training during the first year of my Ph.D., I would not have learned as quickly as I did without his dedicated training and patience. Moreover, I would like to thank all of the friends I made in Nashville, my time here would not have been nearly as eventful without them. They made the long days much more enjoyable and were always there to commiserate in the difficult moments and rejoice in the positive moments. I would specifically like to thank Murt Zohair, John Waugh, and Loren Kreider, despite each of them moving away

from Nashville, their support continued to be unwavering, and I am grateful to have met each of them. I would also like to thank Ryan Kowalski and Cal Craven for all the fun times while still debating science with me regularly.

Additionally, I would like to show my appreciation to the community I have found here in Nashville in animal welfare. Fostering over 50 cats and kittens throughout my graduate work has been exceptionally challenging and beyond rewarding. The friends I have made along the way throughout my volunteer and foster efforts at local shelters, specifically Lena Hooker and Sam Talbot, have been instrumental in making my time in Nashville special and I am so grateful to know each of them. Similarly, as silly as it sounds, I would like to thank my two cats, Jack Muffin and Nikki Nugget for the constant support and love throughout this process. I truly could not have done any of this without them and all their funny antics, cute poses, and loving purrs.

Finally, I would especially like to thank my parents, without whom I never would've been able to pursue or complete my graduate work. My mom who answered countless calls and talked me through every stressful and exciting moment of this process without fail and my dad who inspired my chemical engineering major and always pushes me to pursue my dreams and "use my smarts" simultaneously. Both have provided me with endless support, encouragement, and love throughout not just my graduate studies but also my entire life. Though a cliché, I would not be where I am today without them and cannot express my appreciation of being raised by such amazing and supportive people. Despite knowing little about the process, they have never shied away from wanting to learn more about what I do and are endlessly explaining my research and the Ph.D. process to their friends. In a similar vein, the support and encouragement of my siblings, Ian and Claire, has been instrumental. Through their teasing me of being the "book-smart" one, I

always know how proud they are, and I am exceptionally grateful to have them as my siblings and I likewise am so proud of the people they have grown into.

Table of Contents

LIST OF TABLES

LIST OF FIGURES

Figure Page

Chapter 1

Introduction

As non-renewable resources continue to deplete, global warming intensifies, and environmental regulations continue to call for less pollution, finding greener replacements to current high pollution processes has become a priority. Both governments and industries have been encouraging environmentally conscious redesigns[1]. While stricter environmental regulations help hold industries accountable, replacements for the many greenhouse gas compounds in use have not been identified. With large gaps in the information needed to design greener processes, complying with environmental regulations and moving toward greener manufacturing remains a challenge.

While some novel compounds have been identified as possible replacement fluids, without reliable methods to identify their properties, environmental advancements cannot be made. Therefore, developing a reliable model that can identify the thermodynamic properties of promising molecules is essential in moving towards increased sustainability. This thesis focuses on developing a predictive model to describe new molecules that could replace existing technology and would make applications greener. We also consider the challenge of describing confined fluids.

In the area of confined fluids, this work specifically considers confined fluids in porous materials. Such systems have a wide range of applications, such as for filtration, purification, and adsorption. As confined fluids can have significantly different properties from bulk fluids even at the same temperature and pressure, their properties are of great interest. Experiments are labor intensive and potentially costly, making it difficult to broadly study confined fluid properties. There are well established theoretical approaches for bulk fluids, but fewer for confined fluids. Additionally, due to the wide range of media types for confinement, i.e., cylindrical pores[2],

corrugated substrates[3], carbon nanotubes[4], narrow pores[5], etc., a theoretical approach that can be expanded to represent multiple media types is especially desirable. The most popular theoretical approach to describe confined fluids is the Ornstein-Zernike relation[6–8]. While this approach can predict the properties of confined fluids, it requires a closure expression to fully define the Ornstein-Zernike relation, which can affect the results depending on the closure chosen. Furthermore, none of the closures for the Ornstein-Zernike relation are fully analytical. In Chapter 3, we introduce an analytical theoretical approach that can accurately describe fluids confined in a hard-sphere matrix[9].

In Chapter 4, sulfur containing systems[10] as well as fatty acid methyl ester (FAME) molecules[11] are considered. Petroleum is a major pollutant that wreaks havoc on the environment, especially on marine life and soil contamination[12–14]. A primary contributor to air pollution for petroleum fuels is sulfur impurities in the fuel. One approach to remove a primary sulfur contaminant, thiophene, is to use carbon dioxide because of its nontoxic and nonflammable properties[10, 16]. Extensive information for mixtures of thiophene with carbon dioxide and other solvents is required for designing and implementing a sulfur removal process. While there have been experimental studies on thiophene mixtures with solvents that are correlated by the Peng-Robinson equation of state[17–19], a full picture of thiophene mixtures from experiments would be extremely time and labor intensive.

A theoretical model provides a more efficient way to predict the properties of thiophene mixtures. Most theoretical studies for sulfur molecules like thiophene have used the perturbed chain statistical associating fluid theory (PC-SAFT)[19–21]. While this model is predictive, it neglects the structural information of the molecules, such as thiophene's cyclic structure. Here, a group

contribution approach based on a version of SAFT for potentials of variable range (GC-SAFT-VR[23]) is used to describe sulfur molecules and their mixtures.

FAME molecules, a primary component of biodiesel, are considered next. Biodiesel is a promising alternative to traditional diesel fuel as no engine modifications are required to maintain the same performance. Furthermore, biodiesel is much more environmentally friendly than conventional diesel as it is biodegradable and nontoxic[23]. Biodiesel has the potential to reduce pollutants across many industries, and greatly reduce greenhouse gas emissions[23]. While biodiesel has been studied experimentally[25–27], variations in FAME blends and compositions complicate determining what makes the most efficient biodiesel. A more complete picture of the thermodynamic and phase behavior of FAME molecules, could ensure that the most efficient and effective biodiesel blend can be generated. FAME molecules have been widely studied by various SAFT approaches[27–35], but in each of these studies, the parameters were fit to pure component FAME data or to data for mixtures involving FAME molecules. A fully predictive model for FAME molecules would allow more efficient screening across FAME molecules without needing experimental data to fit model parameters.

The most prominent molecules studied in this work, explored in chapters 5-7, are fluorinated molecules as they have vast environmental applications[36]. Fluorinated molecules contain a dense electron cloud around the fluorine atoms that lead to low surface tensions and dielectric constants as well as high fluidity, vapor pressure, and compressibility. Perfluoroalkanes, specifically, are known for dissolving more carbon dioxide than their hydrogenated counterparts giving them promising applications in carbon capture[37,38]. Another class of fluorinated molecules of interest are hydrofluoroethers (HFEs), due to their promising applications as alternative refrigerants with lower greenhouse gas properties[39,40]. HFEs have low global warming potentials,

zero ozone depletion potential, and short atmospheric lifetimes. In most applications of fluorinated molecules, mixtures are considered to lower flammability and toxicity. Specifically, mixtures with carbon dioxide are of great interest as carbon dioxide is nontoxic and inflammable, however due to the toxicity and flammability of the HFEs, experimental studies have been very limited[42–47]. Additionally, HFEs are quite cost prohibitive to acquire making broad experimental studies expensive.

While theoretical approaches, including SAFT-based methods, have been used to represent fluorinated molecules and their mixtures, many of these studies consider only a small set of molecules with limited predictive power[42, 46–51]. Therefore, a model that can not only predict the phase behavior of pure fluorinated molecules, including both simple and complex fluorinated molecules like perfluoroalkanes and HFEs, respectively, but also of fluorinated mixtures is vital towards further utilization of these compounds. The common feature among these molecule types is that a reliable predictive method is lacking with which to study their thermodynamic properties and phase behavior. To advance environmentally friendly design and lower pollution, more must be known about the possible alternatives. The approach used herein, GC-SAFT-VR, allows the development of a predictive model to describe the phase behavior and thermodynamic properties of fluids with minimal or no experimental data to fit making it an attractive tool for studying these systems.

Chapter 2

Background

2.1 Statistical Associating Fluid Theory (SAFT)

Amid everchanging environmental regulations and compliance concerns, the need for novel fluid properties is growing constantly. An efficient and accurate way to determine the thermodynamic properties and phase behavior of fluids is through theoretical models as calculations take significantly less time and labor than both experimental and molecular simulation methods. Accuracy is of the utmost importance in these methods and has led to the development of numerous equations of state. Perhaps the most successful are those based on the Statistical Associating Fluid Theory (SAFT) originally proposed by Chapman et al.[52,53]. SAFT, based on Wertheim's thermodynamic perturbation theory (TPT)[54–57], represents molecules as chains of tangentially bonded spherical segments that interact via repulsive and dispersive interactions and association (attractive) interactions, where applicable. The repulsive and dispersive interactions in the original SAFT expressions were described by the Lennard-Jones potential.

While the original SAFT expressions were to describe a Lennard-Jones chain fluid, SAFT has been extensively expanded through different levels of theory as well as adjustments to utilize different potentials. The main SAFT expression are described as the summation of four contributions to the Helmholtz free energy (A), as shown in equation 2.1.

$$\frac{A}{Nk_BT} = \frac{A^{\text{ideal}}}{Nk_BT} + \frac{A^{\text{mono}}}{Nk_BT} + \frac{A^{\text{chain}}}{Nk_BT} + \frac{A^{\text{assoc}}}{Nk_BT} \tag{2.1}$$

Here, N is the number of chain molecules, k_B is Boltzman's constant, and T is temperature, while A^{ideal} is the ideal free energy contribution, A^{mono} is the free energy contribution from the monomer

fluid, typically represented as a perturbation on the properties of a reference fluid, A^{chain} is the free energy contribution due to the formation of the chains from the monomer fluid and A^{assoc} is the free energy contribution of association interactions (e.g., hydrogen bonding interactions).

After the initial introduction of SAFT, variations were quickly introduced that built upon the original model. The first variation was introduced by Huang and Radosz[58,59] and is referred to as SAFT-HR. In SAFT-HR, the monomer term is described by a hard-sphere reference plus the mean field dispersion term proposed by Chen and Kreglewski[59]. Size and energy parameters were fitted to experimental data for alkanes[57,58,60], alcohols[57,58], carbon dioxide[61–63], polymers[64–67], electrolytes[68], supercritical fluids[69], and more.

A simpler version of SAFT was introduced by Chapman et. al, known as SAFT hard-sphere or SAFT-HS[70]. SAFT-HS describes hard-sphere segments through the Carnahan and Starling expression, combined with a van der Waals mean field attractive term to represent the dispersive interactions. The expressions for SAFT-HS are simpler than the original SAFT approach as the description of the monomer fluid is much less complex than the expressions for the Lennard-Jones fluid used in the original version of SAFT. SAFT-HS has been shown to accurately represent the phase behavior of a wide variety of molecules such including alkanes[71], water[72,73], alcohols[73], surfactants[73–75], and small fluorinated molecules[72,76]. SAFT-HS in particular finds success for systems with strong association interactions, where the hydrogen bonding interactions dominate.

The soft-SAFT approach was introduced by Blas and Vega[77], using the Lennard-Jones fluid as the reference fluid for the monomer, chain, and association terms. The introduction of soft-SAFT allowed more complex fluids to be considered, like ionic liquids[78–80], biodiesels[31], perfluoroalkanes[41,43,81,82], hydrofluoroethers[46] and oligomers[83], while still being able to accurately

represent simpler molecules such as alkanes[64,84–86], alkenes[87], alcohols[87], water[88], dinitrogenoxide[89], carbon dioxide[89], and polymers[90].

Gross and Sadowski developed perturbed-chain SAFT (PC-SAFT)[19], which was the first method to consider a hard chain reference model instead of the hard sphere reference model. PC-SAFT uses dispersive interactions and association interactions that are dependent on the chain-length as described by Liu and Hu[91] to describe the attractive potentials. Due to its more complex representation of molecules, PC-SAFT has been able to accurately represent a wide variety of molecules including polar compounds, which have previously been difficult to represent, as well as other molecules such as hydrocarbons[19], benzene[92], ionic liquids[93], pharmaceuticals[94–96], asphaltenes[97], and hydrofluoroethers[49,98].

Another of the most prominent SAFT approaches is the SAFT for potentials of variable attractive range, or SAFT-VR[99]. SAFT-VR uses a hard-sphere reference fluid to describe the monomer term and represents the dispersion term via potentials of variable range including the square-well, Lennard-Jones, Mie, or Yukawa potentials. To better describe the dispersion interactions, SAFT-VR treats them by a second-order high-temperature perturbation expansion. SAFT-VR has been used to describe a wide range of fluids and their mixtures; some examples include alkanes[100–102], perfluoroalkanes[48,50,103,104], alcohols[105,106], water[107,108], carbon dioxide[109–111], and polymers[106].

Despite the accuracy and efficiency of the SAFT-family of methods, the approach relies on experimental data for the vapor pressure and saturated liquid density of the fluid of interest being available to fit model parameters to. While this is typically not an issue for common organic molecules, as we search for new molecules a lack of data can prevent the application of SAFT based approaches. In a GC approach, molecules are deconstructed into functional groups and

parameterized independently, rather than parameterizing the molecule as a whole. Therefore, parameters can be determined for simpler molecules that contain the functional group of interest and then applied to molecules where experimental data may not be readily available. While there are other methods that consider group contribution such as GC-PC-SAFT[112–114] and GC-SAFT[36,115,116], we note they use averaged parameters to describe the molecules. Specifically, in GC-sPC-SAFT, a homonuclear model is utilized where the group parameters are weighted based on their thermodynamic and structural impact in the molecule. GC-sPC-SAFT has a large set of parameterized functional groups and is mainly used for polymer systems. Similarly, GC-SAFT uses a homonuclear chain as the model parameters are found by averaging the parameters for different groups. GC-SAFT provides good predictions for smaller molecules but shows increased deviations for longer-chained molecules. GC-SAFT also has limited predictive ability due to the often necessary binary interaction parameters.

Two main group contribution methods that have been widely used and expanded recently are SAFT-γ[117] and GC-SAFT-VR[22]. In SAFT-γ, the molecules are represented by heteronuclear segments fused to form homonuclear chains using effective parameters. SAFT-γ was initially developed using square-well potentials but has also been expanded to use Mie potentials. The functional groups that are parameterized can be used to construct other molecules from classes outside those that they were initially parameterized. SAFT-γ has been accurately applied to study both associating and non-associating systems, including alkanes, alcohols, alkylbenzenes, ketones, amines, and carboxylic acids[117–119]. Similarly, GC-SAFT-VR utilizes transferable functional group parameters, but these functional groups are tangentially bonded to form a heteronuclear chain. A visual representation of the GC-SAFT-VR method is shown in Figure 2.1. GC-SAFT-VR is the only version of SAFT that explicitly considers the heterogeneity of molecules by retaining the

molecule's structural information. GC-SAFT-VR has been able to accurately represent a wide range of molecules including for example alkanes, esters, ethers, alcohols, polymers[22,120,121], cyclic molecules[122] and FAME[11] molecules.

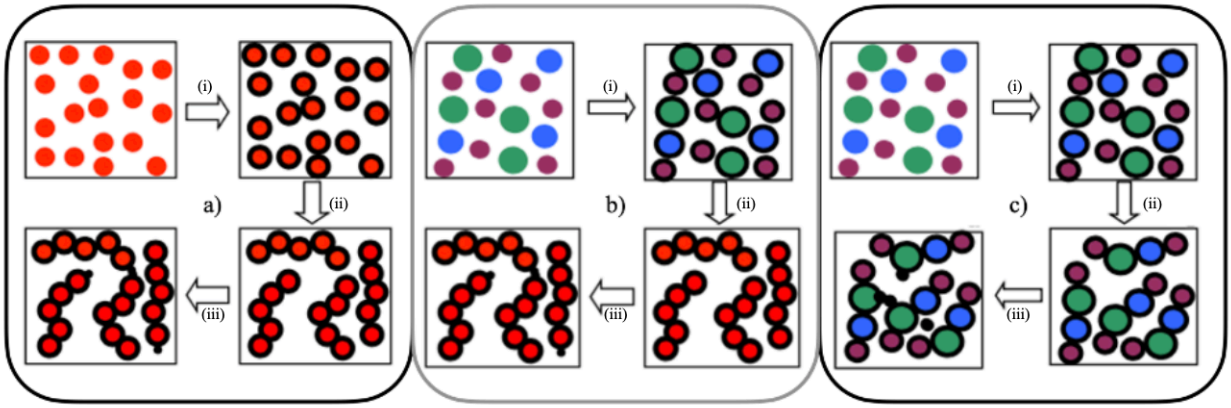

Figure 2.1 Schematic representation of a) a fluid that consists of spherical hard segments where dispersion interactions are added (i), chains are formed through covalent bonds (ii), and then association sites are added to the chains in nonspecific locations (iii), which represents non-group contribution SAFT methods like SAFT, SAFT-HR, SAFT-HS, and SAFT-VR, b) fluid that consists of spherical hard segments of different sizes that interact through group-averaged dispersion interactions (i), chains are formed through covalent bonds (ii), and finally association sites are added to the chains in nonspecific locations (iii), which represents most group contribution methods, such as GC-SAFT and SAFT-γ and c) fluid that consists of spherical hard segments of different sizes that interact through different sized dispersion interactions (i), chains are formed through covalent bonds (ii), and finally association sites are added to specific segments (iii), which represents the GC-SAFT-VR method.

2.2 Group Contribution SAFT of Variable Range (GC-SAFT-VR)

As this work utilizes GC-SAFT-VR, which is built upon the SAFT-VR equation, both methods are outlined in the following sections.

2.2.1 SAFT-VR

SAFT-VR represents molecules as a homonuclear chain formed of hard-core monomers plus attractive potentials of variable range. In this work the attractive interactions are described by a square-well potential (Figure 2.2) which is as follows

$$u_{ij}(r) = \begin{cases} +\infty & \text{if} \quad r < \sigma_{ij} \\ -\varepsilon_{ij} & \text{if} \quad \sigma_{ij} \leq r \leq \lambda_{ij}\sigma_{ij} \\ 0 & \text{if} \quad r > \lambda_{ij}\sigma_{ij} \end{cases} \tag{2.2}$$

where r is the distance between the two segments, σ_{ij} the monomer segment diameter, and ε_{ij} and λ_{ij} are the square-well potential depth and range, respectively.

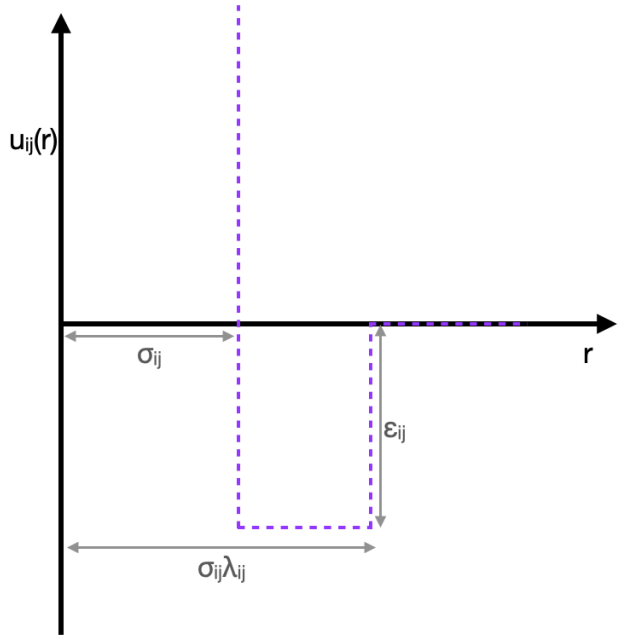

Figure 2.2. Illustration of a square-well potential where σ_{ij} is the interaction diameter and ε_{ij} and λ_{ij} are the square-well potential depth and range, respectively.

Looking at Equation 2.1, the first contribution to the Helmholtz free energy is the ideal term given by,

$$\frac{A^{ideal}}{Nk_BT} = ln(\rho\Lambda^3) - 1 \tag{2.3}$$

where N is the total number of molecules, k_B is the Boltzmann constant, $\rho = N/V$ is the molecular number density, and Λ is the de Broglie wavelength.

The contribution to the Helmholtz free energy from the monomer segments is given by a second-order high-temperature expansion using Barker and Henderson perturbation theory as

$$\frac{A^{mono}}{Nk_BT} = m\frac{A^M}{N_sk_BT} = ma^M = m(a^{HS} + \beta a_1 + \beta^2 a_2) \tag{2.4}$$

where N, k_B, and T are the same as previously defined, N_s is the number of segments, m is the number of square-well dispersive spherical monomer segments in each chain, $\beta = 1/k_B T$, a^M is the excess Helmholtz free energy per segment, a^{HS} is the free energy contribution given by the hard-sphere reference system from Carnahan and Starling[123] as expressed in equation 2.5, and a_1 and a_2 are the first and second order perturbation terms, respectively. In equation 2.4, a^{HS} is described by

$$a^{HS} = \frac{4\eta - 3\eta^2}{(1-\eta)^2} \tag{2.5}$$

where η is the packing fraction of the system and is expressed as $\eta = \frac{\pi}{6}\rho\sigma^3$ where ρ and σ have already been defined as the molecular number density and segment diameter, respectively.

The first order perturbation term a_1 is given by[124–126]

$$a_1 = -2\pi\rho_s\varepsilon \int_0^\infty r^2 \phi(r) g^{HS}(r)\, dr \tag{2.6}$$

where $\rho_s = N_s/V$ is the number density of spherical segments, ε is the energy well depth, $\phi(r)$ is the shape of the interaction potential, and $g^{HS}(r)$ is the pair radial distribution function of the hard-sphere reference system. For the integral above as solved by Gil-Villegas and colleagues[99] using the mean-value theorem with the van der Waals attractive constant, the first order perturbation term simplifies to,

$$a_1 = a_1^{VDW} g^{HS}(\xi;\eta) \tag{2.7}$$

where ξ represents a certain distance in the expression, which is dependent on density and range. Using the square-well potential, the attractive van der Waals parameter is given by,

$$a_1^{VDW} = 4\eta\varepsilon(\lambda^3 - 1). \tag{2.8}$$

Gil-Villegas et al.[99] showed that simplifying g^{HS} by a Taylor expansion around the contact value, the leading term $g^{HS}(1;\eta)$ can be evaluated at an effective packing fraction η^{eff},

$$g^{HS}(\xi;\eta) = g^{HS}(1;\eta^{eff}) \tag{2.10}$$

which allows the first-order perturbation term to be written as

$$a_1 = a_1^{VDW} g^{HS}(1;\eta^{eff}) = 4\eta\varepsilon(\lambda^3 - 1)g^{HS}(1;\eta^{eff}). \tag{2.11}$$

Now, the pair radial distribution function, g^{HS}, is given by

$$g^{HS}(1;\eta^{eff}) = \frac{1 - \eta^{eff}/2}{(1-\eta^{eff})^3} \tag{2.12}$$

as obtained by Carnahan and Starling[123], where the effective packing fraction, η^{eff}, is defined as

$$\eta^{eff} = c_1\eta + c_2\eta^2 + c_3\eta^3 \tag{2.13}$$

for the range $1.1 \leq \lambda \leq 1.8$, where the coefficients in the polynomial above are given by the following matrix[127]

$$\begin{pmatrix} c_1 \\ c_2 \\ c_3 \end{pmatrix} = \begin{pmatrix} 2.25855 & -1.50349 & 0.249434 \\ -0.669270 & 1.40049 & -0.827739 \\ 10.1576 & -15.0427 & 5.30827 \end{pmatrix} \begin{pmatrix} 1 \\ \lambda \\ \lambda^2 \end{pmatrix}. \tag{2.14}$$

In order to represent longer ranges, Patel and coworkers[128] increased the range to $\lambda < 3$ using Padé approximations to give

$$\eta^{eff}(\eta,\lambda) = \frac{c_1\eta + c_2\eta^2}{(1 + c_3\eta)^3}, \tag{2.15}$$

with the coefficients given by

$$\begin{pmatrix} c_1 \\ c_2 \\ c_3 \end{pmatrix} = \begin{pmatrix} -3.16492 & 13.35007 & -14.80567 & 5.07286 \\ 43.00422 & -191.66232 & 273.89686 & -128.93337 \\ 65.04194 & -266.46273 & 361.04309 & -162.69963 \end{pmatrix} \begin{pmatrix} 1/\lambda \\ 1/\lambda^2 \\ 1/\lambda^3 \\ 1/\lambda^4 \end{pmatrix}. \tag{2.16}$$

Next, the second-order perturbation term, a_2, based on the expression by Barker and Henderson[125–127] is given by

$$a_2 = \frac{1}{2} K^{HS} \varepsilon \eta \frac{\partial a_1}{\partial \eta}, \tag{2.17}$$

where K^{HS} is the hard-sphere isothermal compressibility, which can be obtained from the Percus-Yevick expression[124] as

$$K^{HS} = \frac{(1-\eta)^4}{1+4\eta+\eta^2}, \tag{2.18}$$

which is the final term needed to fully define the monomer contribution.

Furthermore, the contribution to the Helmholtz free energy for the chain formation, $\frac{A^{chain}}{Nk_BT}$, from *m* monomer segments is given by,

$$\frac{A^{chain}}{Nk_BT} = -(m-1)ln\big(y^{SW}(\sigma)\big) \tag{2.19}$$

where $y^{SW}(\sigma)$ is the background correlation function as obtained from the high temperature expansion of the pair radial distribution function. The background correlation function is represented as,

$$y^{SW}(\sigma) = exp\big(\beta u^{SW}(\sigma)\big) g^{SW}(\sigma), \tag{2.20}$$

which evaluated at the hard-core contact value for the square-well potential, $u^{SW}(\sigma)$, can be simplified to,

$$y^{SW}(\sigma) = exp(-\beta\varepsilon) g^{SW}(\sigma) \tag{2.21}$$

where $g^{SW}(\sigma)$ is the radial distribution function at the contact distance, which is truncated at the first-order term using the high-temperature perturbation expansion given by,

$$g^{SW}(\sigma) = g^{HS}(\sigma) + \beta\varepsilon g_1(\sigma) \tag{2.22}$$

where $g^{HS}(\sigma)$ is obtained from the Carnahan and Starling[123] equation of state as,

$$g^{HS}(\sigma) = \frac{1-\eta/2}{(1-\eta)^3}. \tag{2.23}$$

$g_1(\sigma)$ is derived using the Clausius virial theorem and the density derivative of the Helmholtz free energy is given by,

$$g_1(\sigma) = \frac{1}{4\varepsilon}\left[\frac{\partial a_1}{\partial \eta} - \frac{\lambda}{3\eta}\frac{\partial a_1}{\partial \lambda}\right]. \tag{2.24}$$

Finally, the contribution to the Helmholtz free energy from the association energy, based on Wertheim's thermodynamic perturbation theory[54,99], is given by,

$$\frac{A^{assoc}}{Nk_BT} = \left[\left(\sum_{a=1}^{s} lnX_a - \frac{X_a}{2}\right) + \frac{s}{2}\right] \tag{2.25}$$

where the sum is over all association sites, *s*, of type *a* on a molecule and X_a is the fraction of molecules not bonded to site *a*. X_a is given by[52,70]

$$X_a = \frac{1}{1 + \sum_{b=1}^{s} \rho X_b \Delta_{a,b}}, \tag{2.26}$$

where $\Delta_{a,b}$ is the association strength between sites of types *a* and *b* on different molecules, as no intramolecular association is allowed, only intermolecular association, and is given by,

$$\Delta_{a,b} = K_{a,b} f_{a,b} g^{SW}(\sigma) \tag{2.27}$$

where $f_{a,b}$ is the Mayer *f* function for the *a*-*b* site-site interaction and $K_{a,b}$ is the bonding volume[70] and both are given by,

$$f_{a,b} = exp\left(-\psi_{a,b}/k_BT\right) - 1 \tag{2.28}$$

$$K_{a,b} = 4\pi\frac{\sigma^2}{72r_d^2}\left[\begin{array}{c} ln\left(\frac{r_c + 2r_d}{\sigma}\right)(6r_c^3 + 18r_c^2 r_d - 24r_d^3) + \cdots \\ (r_c + 2r_d - \sigma)(22r_d^2 - 5r_c r_d - 7r_d\sigma - 8r_c^2 + r_c\sigma + \sigma^2) \end{array}\right] \tag{2.29}$$

where $K_{a,b}$ is typically obtained by directly fitting to experimental phase behavior but can also be found using the position of the site within the molecule and the range of the association site, r_d and r_c, respectively.

The above expressions are used to represent pure fluids using SAFT-VR. Each of these expressions can be expanded to represent mixtures using the appropriate mixing rules[99]. The mixture expressions for SAFT-VR are not required in this work as GC-SAFT-VR is built upon the mixture version of SAFT-VR to account for each functional group parameters, so including those expressions here would be repetitive; however, any molecule includes only one functional group, such as carbon dioxide for example, is represented by SAFT-VR as there are no groups for the group contribution.

2.2.2 GC-SAFT-VR

Group contribution SAFT for potentials of variable range (GC-SAFT-VR)[22,121] is the only GC-based SAFT method that explicitly considers the heterogeneity of the molecules. GC-SAFT-VR breaks each molecule into functional groups, each with their own size and interaction parameters. The functional group parameters are fit to pure molecules containing the functional groups of interest, making all mixture calculations purely predictive. GC-SAFT-VR is represented by the sum of contributions to the Helmholtz free energy from the ideal, monomer, chain, and association terms in equation 2.1 and is designed to utilize the square-well potential in equation 2.2 and figure 2.2 above.

The segment diameter and cross interactions for size and energy between unlike segments can be expressed by the Lorentz-Berthelot combining rules[129],

$$\sigma_{ki,lj} = \frac{\sigma_{ki,ki} + \sigma_{lj,lj}}{2} \tag{2.30}$$

$$\varepsilon_{ki,lj} = \xi_{ki,lj}\sqrt{\varepsilon_{ki,ki}\varepsilon_{lj,lj}} \tag{2.31}$$

$$\lambda_{ki,lj} = \gamma_{ki,lj}\left(\frac{\sigma_{ki,ki}\lambda_{ki,ki} + \sigma_{lj,lj}\lambda_{lj,lj}}{\sigma_{ki,ki} + \sigma_{lj,lj}}\right) \tag{2.32}$$

where $\xi_{ki,lj}$ and $\gamma_{ki,lj}$ are binary interaction parameters that enable adjustments to the cross interactions from the geometric and arithmetic mean values, respectively. Binary interaction parameters allow better parameterization, specifically between two strongly polar components where the Lorentz-Berthelot combining rules do not adequately describe the interactions.

The ideal contribution to the Helmholtz free energy is given by,

$$\frac{A^{ideal}}{Nk_BT} = \sum_{k=1}^{n_{components}} x_k ln\left(\rho_k {\Lambda_k}^3\right) - 1 \tag{2.33}$$

where $n_{components}$ represents the number of pure components in the system, x_k is the mole fraction of component k, ρ_k is the molecular number density, N_k/V, where N_k is the number of molecules of component k and V is the volume of the system, and Λ_k is the de Broglie wavelength of component k.

The monomer contribution to the Helmholtz free energy is given by the high temperature expansion of the second-order Barker Henderson perturbation theory for mixtures[125,130],

$$\frac{A^{mono}}{Nk_BT} = \sum_{k=1}^{n}\sum_{i=1}^{n'_k} m_{ki}x_k\left(a^{HS} + \frac{a_1}{k_BT} + \frac{a_2}{(k_BT)^2}\right), \tag{2.34}$$

where n'_k is the number of functional groups of type i in a chain of component k, m_{ki} is the number of segments of type i in chains of component k, and a^{HS}, a_1, and a_2 represent the hard-sphere reference term and the first and second order perturbation terms, respectively. The hard-sphere reference term, a^{HS}, as derived by Boublik[131] and Mansoori[132], is given as

$$a^{HS} = \frac{6}{\pi\rho_s}\left[\left(\frac{\zeta_2^3}{\zeta_3^2} - \zeta_0\right) ln(1-\zeta_3) + \frac{3\zeta_1\zeta_2}{1-\zeta_3} + \frac{\zeta_2^3}{\zeta_3(1-\zeta_3)^2}\right] \tag{2.35}$$

where ρ_s is the total number density of segments, the same as was defined above and ζ_i is the reduced density given by a sum over all segments as

$$\zeta_l = \frac{\pi}{6}\rho_s\left[\sum_{k=1}^{n}\sum_{i=1}^{n_k'} x_{s,ki}\left(\sigma_{ki,ki}\right)^l\right], \qquad l = 0,1,2,3 \tag{2.36}$$

where $\sigma_{ki,ki}$ is the diameter of segments of type *i* in chain *k,* and $x_{s,ki}$ is the mole fraction of segments of type *i* in chain *k*, which is expressed as

$$x_{s,ki} = \frac{x_k m_{ki}}{\sum_{k=1}^{n} x_k m_{ki}}. \tag{2.37}$$

The first perturbation term, a_1 describing the mean-attractive energy is obtained from the sum of all pairwise interactions and is given by the series of summations,

$$a_1 = \sum_{l=1}^{n}\sum_{j=1}^{n_l'}\sum_{k=1}^{n}\sum_{i=1}^{n_k'} x_{s,ki}x_{s,lj}(a_1)_{ki,lj} \tag{2.38}$$

where $(a_1)_{ki,lj}$ is obtained from the mean-value theorem[99] and expressed through the hard-sphere radial distribution function $g_0^{HS}\left[\sigma_x; \zeta_x^{eff}\left(\lambda_{ki,lj}\right)\right]$ using the van der Waals one fluid theory obtained from the Carnahan and Starling equation of state[123]. Both expressions are given as

$$(a_1)_{ki,lj} = -\rho_s\frac{2\pi}{3}\sigma_{ki,lj}^3\varepsilon_{ki,lj}\left(\lambda_{ki,lj}^3 - 1\right)g_0^{HS}\left[\sigma_x; \zeta_x^{eff}\left(\lambda_{ki,lj}\right)\right] \tag{2.39}$$

$$g_0^{HS}\left[\sigma_x; \zeta_x^{eff}\left(\lambda_{ki,lj}\right)\right] = \frac{1 - \zeta_x^{eff}/2}{\left(1 - \zeta_x^{eff}\right)^3} \tag{2.40}$$

where the effective packing fraction ζ_x^{eff} was obtained from the Padé expression[128]

$$\zeta_x^{eff} = \frac{c_1\zeta_x + c_2{\zeta_x}^2}{(1 + c_3\zeta_x)^3} \tag{2.41}$$

with coefficients given by

$$\begin{pmatrix} c_1 \\ c_2 \\ c_3 \end{pmatrix} = \begin{pmatrix} -3.16492 & 13.35007 & -14.80567 & 5.07286 \\ 43.00422 & -191.66232 & 273.89686 & -128.93337 \\ 65.04194 & -266.46273 & 361.04309 & -162.69963 \end{pmatrix}\begin{pmatrix} 1/\lambda_{ki,lj} \\ 1/\lambda_{ki,lj}^2 \\ 1/\lambda_{ki,lj}^3 \\ 1/\lambda_{ki,lj}^4 \end{pmatrix} \tag{2.42}$$

and

$$\zeta_x^{eff} = \frac{\pi}{6}\rho_s\sigma_x^3 = \frac{\pi}{6}\rho_s\sum_{l=1}^{n}\sum_{j=1}^{n_l'}\sum_{k=1}^{n}\sum_{i=1}^{n_k'}x_{s,ki}x_{s,lj}\sigma_{ki,lj}^3 \tag{2.43}$$

The second-order perturbation term for the monomer Helmholtz free energy contribution is given by,

$$a_2 = \sum_{l=1}^{n}\sum_{j=1}^{n_l'}\sum_{k=1}^{n}\sum_{i=1}^{n_k'}x_{s,ki}x_{s,lj}(a_2)_{ki,lj}\,, \tag{2.44}$$

where $(a_2)_{ki,lj}$ is obtained through a local compressibility approximation given as,

$$(a_2)_{ki,lj} = \frac{1}{2}K^{HS}\varepsilon_{ki,lj}\rho_s\frac{\partial(a_1)_{ki,lj}}{\partial\rho_s}. \tag{2.45}$$

Here K^{HS} is the hard-sphere mixture isothermal compressibility obtained from the Percus-Yevick expression[124]

$$K^{HS} = \frac{\zeta_0(1-\zeta_3)^4}{\zeta_0(1-\zeta_3)^2 + 6\zeta_1\zeta_2(1-\zeta_3) + 9\zeta_2^3}. \tag{2.46}$$

The contributions to the Helmholtz free energy from chain formation and the associating segments are also described briefly here with more information available in the original publication by dos Ramos et al.[133]. The chain contribution is modeled by a hetero-segmented monomer fluid represented by,

$$\frac{A^{chain}}{Nk_BT} = -\sum_{k=1}^{n}x_k\sum_{ij}ln\,y_{ki,kj}^{SW}\left(\sigma_{ki,kj}\right) \tag{2.47}$$

where the first sum is over all components, *n*, in the mixture, x_k is the mole fraction of component *k*, and the second sum considers the chain formation and the connectivity of the segments within a given component *k*. The background correlation function $y_{ki,kj}^{SW}$ is given by,

$$y_{ki,kj}^{SW}(\sigma_{ki,kj}) = exp\left(\frac{-\varepsilon_{ki,kj}}{k_B T}\right) g_{ki,kj}^{SW}(\sigma_{ki,kj}) \tag{2.48}$$

where $\varepsilon_{ki,kj}$ is the segment-segment dispersion energy well depth and $g_{ki,kj}^{SW}(\sigma_{ki,kj})$ is the radial distribution function for the square-well monomers at the contact distance of $\sigma_{ki,kj}$ which is approximated by a first-order high temperature expansion.[99]

The association interaction of a site *a* on a functional group type *i* within the molecule *k* with a site *b* on a group of type *j* within molecule *l* is modeled by a square-well potential as

$$u_{kia,ljb}^{HB}(r_{ab}) = \begin{cases} -\varepsilon_{kia,ljb}^{HB} & if \;\; r_{ab} \leq r_{c_{kia,ljb}} \\ 0 & if \;\; r_{ab} > r_{c_{kia,ljb}} \end{cases} \tag{2.49}$$

where r_{ab} represents the distance between the center of sites *a* and *b,* and $\varepsilon_{kia,ljb}^{HB}$ and $r_{c_{kia,ljb}}$ are the association energy and range, respectively. Unlike association interactions are given by the combining rules,

$$\varepsilon_{kia,ljb}^{HB} = \sqrt{\varepsilon_{kia,kib}^{HB} \varepsilon_{lja,ljb}^{HB}} \tag{2.50}$$

$$K_{kia,ljb}^{HB} = \left(\frac{\left(K_{kia,kib}^{HB}\right)^{1/3} + \left(K_{lja,ljb}^{HB}\right)^{1/3}}{2} \right)^3 \tag{2.51}$$

where K^{HB} is the bonding volume between association sites. The association cross interactions can deviate from the ideal combining rules, similar to that described for equations 2.31 and 2.32.

The association contribution to the Helmholtz free energy between association sites on different functional groups comprising a molecule is defined as,

$$\frac{A^{assoc}}{N k_B T} = -\sum_{k=1}^{n} x_k \sum_{i=1}^{n_k'} v_{ki} \sum_{a=1}^{ns_i'} n_{ia} \left(\ln X_{kia} + \frac{1 - X_{kia}}{2} \right) \tag{2.52}$$

where the first sum is over the number of components *n*, the second is over all the types of functional groups in a molecule *k* (n_k'), and the final is over the total number of site types in a

functional group i (ns_i'). Furthermore, n_{ia} represents the number of associating sites of type a while X_{kia} is the fraction of component k not bonded at site a both on functional group i. The fractions X_{kia} are obtained from solution of the mass-action equations[52,134] which when expressed in terms of the total number density of the system is

$$X_{kia} = \frac{1}{1 + \rho \sum_{l=1}^{n} x_l \sum_{j=1}^{n_l'} v_{ij} \sum_{b=1}^{ns'} n_{jb} X_{ljb} \Delta_{kia,ljb}}. \tag{2.53}$$

Here $\Delta_{kia,ljb}$ depends on the strength of the association sites a and b located on groups i and j of components k and l, respectively, and is defined by,

$$\Delta_{kia,ljb} = K_{kia,ljb}^{HB} f_{kia,ljb} g_{ki,lj}^{SW}(\sigma_{ki,lj}) \tag{2.54}$$

where $K_{kia,ljb}^{HB}$, $f_{kia,ljb}$, and $g_{ki,lj}^{SW}(\sigma_{ki,lj})$ are the volume available for bonding, the Mayer f-function and the radial distribution function for the square-well monomers, respectively. The Mayer f-function is represented as

$$f_{kia,ljb} = exp\left(\frac{\varepsilon_{kia,ljb}^{HB}}{k_B T}\right) - 1 \tag{2.55}$$

where $\varepsilon_{kia,ljb}^{HB}$ is the well depth of the square-well site-site interactions between sites a and b located on segments i and j of components k and l, respectively, and $K_{kia,ljb}^{HB}$ is the volume available for bonding. Once the Helmholtz free energy is obtained, other thermodynamic properties, such as chemical potential and pressure can be calculated through standard thermodynamic relationships with the definition for Helmholtz free energy $A = -PV + \mu N$.

The process used to fit the main parameters m_{ki}, $\sigma_{ki,ki}$, $\varepsilon_{ki,lj}$, and $\lambda_{ki,lj}$, binary interaction parameters $\xi_{ki,lj}$ and $\gamma_{ki,lj}$, and association parameters $\varepsilon_{kia,ljb}^{HB}$ and $K_{kia,ljb}^{HB}$ as applicable for each functional group segment is known as simulated annealing[135–137]. Simulated annealing is a global optimization process that is able to distinguish from local optima in order to find the global

optimization solution. In essence, after providing a set of initial guesses and minimization criteria, the calculation steps through the parameter space within a given set of bounds for each parameter being fit searching for the minimum. The advantage of this method is that although "downhill" steps are always accepted to minimize the function, "uphill" steps can also be accepted based on the Metropolis criteria[138], which allows the optimization to escape the local minima. The simulated annealing method is used when fitting a new functional group to a pure component that contains that functional group's experimental vapor pressure and saturated liquid density. Once a components m_{ki}, $\sigma_{ki,ki}$, $\varepsilon_{ki,lj}$, and $\lambda_{ki,lj}$ parameters are optimized, they can be used to represent other components to optimize any binary interaction parameters that deviate from the Lorentz-Berthelot combining rules between functional groups that were not included in the original fit. If a group requires cross interactions with any groups in the molecules that are used to complete the fitting, they are fit simultaneously with the baseline parameters, m_{ki}, $\sigma_{ki,ki}$, $\varepsilon_{ki,lj}$, and $\lambda_{ki,lj}$. For any associating functional group that needs to be fit, the association parameters, $\varepsilon^{HB}_{kia,ljb}/k_B$ and $K^{HB}_{kia,ljb}$, are fit simultaneously with m_{ki}, $\sigma_{ki,ki}$, $\varepsilon_{ki,lj}$, and $\lambda_{ki,lj}$. In order to ensure an optimized fit, the difference between the theoretical and experimental data is minimized using the squared difference.

When a group is not contained within any other molecules, such as carbon dioxide, any required binary interaction parameters are necessarily fit to the mixture. This is unavoidable as these small molecules are not contained within larger molecules with other functional groups. In this event, the necessary binary interaction parameters are fit by hand, by guessing sets of binary interaction parameters and choosing the set that best minimizes the AAD values. Although this hand-fitting process is less efficient, it is necessary for these molecules and been successful[11,45,47,139].

2.3 Second-Order Barker-Henderson Perturbation Theory and Scaled Particle Theory

Chapter 3 is the only work in this thesis that does not utilize GC-SAFT-VR as it introduces a new analytical theoretical model to describe confined fluids. Therefore, the entirety of this new theoretical method is detailed in Chapter 3.

Chapter 3

Liquid-Vapor Phase Equilibrium of a Simple Liquid Confined in a Random Porous Media

This chapter was taken from the published work of A. K. Nelson et al.[9]

3.1 Introduction

Understanding the thermodynamic properties and phase behavior of fluids and fluid mixtures adsorbed in porous media is of substantial interest for both fundamental science and engineering applications[140–143]. Porous materials are widely used as adsorbents in numerous technological processes, such as filtration and purification, heterogeneous catalysis, adsorption and separations. The properties of the fluids confined in porous media are known to be markedly different from those in the bulk, which represents a challenge for their understanding and description on the molecular level. For example, the liquid-gas phase diagrams of ^{4}He[144], N_2[145], and the mixture of isobutyric acid and water[146] confined in dilute silica gel are much narrower than those in the bulk, with the critical points shifted toward the lower temperatures.

Describing the thermodynamics and phase behavior of fluids in porous media is challenging due to the necessity of considering the effects of confinement, the fluid-media interaction, the random nature of the pores and their interconnection, etc. Additionally, the phase behavior of adsorbed fluids is very sensitive to the microscopic structure of the adsorbent. Even for porous materials with the same geometrical and statistical properties, such as porosity, size of the obstacles, and distribution of pore sizes, the corresponding fluid phase diagrams can be qualitatively quite different, e.g. having either one or two critical points[147]. However, since the pioneering work of Madden and Glandt[148], Madden[149] and subsequent important work of Given and Stell[150], considerable progress has been achieved in the theoretical description of the structural

properties and thermodynamics of fluids confined in porous media. In[148–150], the porous medium is modeled as a quenched disordered configuration of particles. The properties of the liquids adsorbed in such medium (the so-called matrix) are described using the corresponding version of the Ornstein-Zernike (OZ) equation called the replica OZ (ROZ) equation, supplemented by analogs of the standard closures of the OZ equation utilized in liquid state theory. In the meantime a number of extensions and modifications of the ROZ approach have been developed and applied (see[143,151] and references therein). These include extensions of the ROZ theory in the framework of the reference interaction site model (RISM) approach[152–154] and multi-density integral equation formalism of Wertheim for associating fluids[155–160], extensions of the ROZ equation's treatment of systems with Coulombic interactions[161–171] and inhomogeneous systems[172,173]. In addition to the ROZ approach density functional theory based approaches for inhomogeneous systems have also been proposed[174–176].

Similar to the regular OZ approach, straightforward application of the ROZ theory is difficult as there is a substantial region of thermodynamic states for which no convergent solutions to the ROZ equation can be found. In addition, none of the closures of the ROZ equation proposed are amenable to an analytical solution. Therefore, most of the theoretical studies of the phase behavior of liquids confined in porous media are based on the application of different approximate perturbation schemes with ROZ equations used to calculate the thermodynamic and/or structural properties of the corresponding reference system[6–8,177–181]. In the papers of Kierlik et al.[7,8,180], Trokhymchuk et al.[179] and Patsahan et al.[181] the contribution of the attractive part of the interaction was calculated using the numerical solution of the ROZ with a mean spherical approximation (MSA) type of closure.

Recently, scaled particle theory (SPT) was extended and applied to predict the properties of the hard-sphere fluid in porous media[182–185]. The media was represented by a matrix of hard-sphere obstacle particles randomly placed in a configuration of HS fluid quenched at equilibrium. Unlike ROZ theory, this proposed version of SPT provides a closed form analytical expressions for the thermodynamics of the system. This feature of SPT is very useful, since it enables one to use an analytical description of the reference system in various thermodynamic perturbation theories. Furthermore, predictions from the present version of SPT are perhaps the most accurate in comparison with predictions of the currently available theoretical methods for hard-sphere systems, i.e., ROZ theory.

Additionally, the phase behavior of several model liquids adsorbed in porous media has been studied using the SPT description of the corresponding reference systems. These studies include applications of the Barker-Henderson (BH) perturbation theory to the Lennard-Jones (LJ) fluid [186], the high temperature approximation to the polydisperse hard-sphere Yukawa fluid[187], Wertheim's thermodynamic perturbation theory (TPT) to hard-sphere network forming[188] and polydisperse square-well (SW) chain[189] fluids, the associative mean spherical approximation (AMSA)[190], and the collective variable method[191] to a charged hard-sphere fluid.

Confined fluid properties have also been actively studied using simulation methods, with an emphasis on Monte Carlo (MC) methods. The majority of these simulations focus on describing the LJ fluid under confinement conditions through various MC methods, such as standard MC[192], grand-canonical MC[193–196], and Gibbs ensemble MC[147,197]. Confined SW fluids have also been studied using grand-canonical transition-matrix MC[198]. However, while LJ and SW fluids are well represented, both simulation and theoretical approaches that utilize other potentials for the model

fluid have been widely neglected. We note that computer simulations of the phase behavior of fluids adsorbed in porous media are challenging. During each simulation, the fluid properties must be averaged with respect to the different realizations of the matrix (i.e., porous media), which is time consuming, since each realization requires a separate simulation. Also, it is generally not clear how many realizations are needed and what size of the matrix sample should be used in order to obtain sufficiently accurate predictions.

In this chapter, we propose a simple analytical theory for predicting the thermodynamic properties and phase behavior of liquid mixtures with any number of components confined in random porous media. The theory is based on the combination of SPT and second-order BH (BH2) perturbation theory. The liquid is represented by an n- component mixture of the hard-sphere Morse (HSM) model and the porous media is modeled by the HS fluid quenched at equilibrium. The choice of the HSM model and SPT description of the reference system enables us to formulate a completely analytical version of the second-order BH perturbation theory for systems with an arbitrary number of components. Note that previous studies of the phase behavior are based on the numerical solutions of the ROZ equation, which is rather cumbersome to use even in the one-component case and quickly becomes impractical as the number of components increases. The accuracy of the theory, as well as its applicability, is demonstrated by comparison of the theoretical predictions against corresponding MC simulations.

3.2 Model & Theory

We consider a simple liquid mixture confined in a random porous medium. The liquid is modeled by a multicomponent mixture of hard spheres of different size with an additional attractive Morse potential. For the porous medium the model suggested by Madden and Glandt[148,149] is used, in

which a matrix of hard-sphere obstacles formed by a fluid of hard particles quenched at equilibrium is used. In addition to the hard-sphere interaction, the particles of the liquid interact with the matrix obstacles via the attractive Morse potential. The pair potential acting between the particles of the system is

$$U_{ij}^{(M)}(r) = U_{ij}^{(hs)}(r) + U_{ij}^{(M)}(12) \tag{3.1}$$

where i,j denotes the particle species and takes the values 0, …, n, $U_{ij}^{(hs)}(r)$is the hard sphere potential

$$U_{ij}^{(hs)}(r) = \begin{cases} \infty, & for\ r < \sigma_{ij} \\ 0, & for\ r > \sigma_{ij} = (\sigma_i + \sigma_i)/2 \end{cases} \tag{3.2}$$

σ_i is the hard-sphere diameter of the particle of species i, and $U_{ij}^{(M)}(r)$ is the Morse potential

$$U_{ij}^{(M)}(r) = \begin{cases} 0, & for\ r < \sigma_{ij} \\ -\varepsilon_{ij}^{(M)} \exp\left[-z_{ij}\left(r - \sigma_{ij}\right)\right], & for\ r > \sigma_{ij} \end{cases} \tag{3.3}$$

Here, as usual i = 0 denotes hard-sphere obstacles of the matrix $\varepsilon_{00}^{(M)} = 0$ and the screening parameter $z_{ij} = 1.8/\sigma_1$.

The theoretical description of the model at hand is carried out using BH2 perturbation theory[187,189,199] in combination with scaled particle theory. We assume that the Helmholtz free energy of our liquid mixture can be written as follows

$$A = A_{ref} + \Delta A_1^{(M)} + \Delta A_2^{(M)} \tag{3.4}$$

where A_{ref} is Helmholtz free energy for the reference system, and A_1 and A_2 the first and second perturbation terms respectively.

$$\frac{\beta \Delta A_1^{(M)}}{V} = 2\pi\beta \sum_{ij} \rho_i \rho_j \int_0^\infty dr\, r^2 U_{ij}^{(M)}(r) g_{ij}^{(ref)}(r) \tag{3.5}$$

$$= 2\pi\beta \sum_{ij} \varepsilon_{ij}^{(M)} \rho_i \rho_j \, e^{2 z_{ij} \sigma_{ij}} \left. \frac{\partial G_{ij}^{(ref)}(s)}{\partial s} \right|_{s=z_{ij}}$$

and

$$\frac{\beta \Delta A_2^{(M)}}{V} = -\pi\beta^2 K^{(ref)} \sum_{ij} \rho_i \rho_j \int_0^\infty dr\, r^2 \left[U_{ij}^{(M)}(r) \right]^2 g_{ij}^{(ref)}(r) \tag{3.6}$$

$$= \pi\beta^2 K^{(ref)} \sum_{ij} \left(\varepsilon_{ij}^{(M)} \right)^2 \rho_i \rho_j \, e^{2 z_{ij} \sigma_{ij}} \left. \frac{\partial G_{ij}^{(ref)}(s)}{\partial s} \right|_{s=2z_{ij}}$$

Here $g_{ij}^{(ref)}(r)$ is the radial distribution function (RDF) of the reference system $G_{ij}^{(ref)}(s)$ is the Laplace transform of $g_{ij}^{(ref)}(r)$,

$$G_{ij}^{(ref)}(s) = \int_0^\infty dr\, r e^{-sr} g_{ij}^{(ref)}(r) \tag{3.7}$$

$K^{(ref)}$ is isothermal compressibility of the reference system, i.e.

$$K^{(ref)} = \left(\frac{\partial \rho}{\partial \left(\beta P_{ref} \right)} \right) \tag{3.8}$$

P_{ref} is the pressure of the reference system, $\beta = 1/k_B T$, T is the temperature, ρ_i is the number density of the component *i* and $\rho = \sum_{i=1}^{n} \rho_i$.

The reference system is represented by the multicomponent hard-sphere fluid confined in the random porous medium. The thermodynamic properties of the system are calculated using a recently proposed version of scaled particle theory (SPT)[184]. In the framework of SPT, explicit analytical expressions for the Helmholtz free energy and chemical potential of the n-component hard-sphere fluid confined in the hard-sphere random matrix have been derived[182–185]. To avoid repetition, we do not present them here and refer the reader to the original publications[182–185]. However, for the sake of completeness, the SPT expressions for the Helmholtz free energy, chemical potential, and compressibility of the one-component hard- sphere fluid in the matrix, which will be used in our numerical calculations are provided below. We have

$$\frac{\beta A_{hs}}{N} = \beta\mu_{hs} - \frac{\beta P_{hs}}{\rho} \tag{3.9}$$

where

$$\frac{\beta P_{hs}}{\rho} = \frac{1}{1-\eta/\phi_0}\frac{\phi_0}{\phi} + \left(\frac{\phi_0}{\phi} - 1\right)\frac{\phi_0}{\eta} ln\left(1 - \frac{\eta}{\phi_0}\right) + \frac{a}{2}\frac{\eta/\phi_0}{(1-\eta/\phi_0)^2} + \frac{2b}{3}\frac{(\eta/\phi_0)^2}{(1-\eta/\phi_0)^3} \tag{3.10}$$

$$\beta\mu_{hs} = \ln(\Lambda_1^3\rho) + \beta\mu_1^{(ex)} - ln\left(1 - \frac{\eta}{\phi_0}\right) + \frac{\eta(\phi_0 - \phi)}{\phi_0\phi(1-\eta/\phi_0)} + (1+a)\frac{\eta/\phi_0}{(1-\eta/\phi_0)} + \frac{(a+2b)}{2}\frac{(\eta/\phi_0)^2}{(1-\eta/\phi_0)^2} + \frac{2b}{3}\frac{(\eta/\phi_0)^3}{(1-\eta/\phi_0)^3} \tag{3.11}$$

$$K_{hs} = \left[\frac{1}{1-\eta/\phi_0} + \frac{\eta/\phi_0}{(1-\eta/\phi_0)^2} + a\frac{\eta/\phi_0}{(1-\eta/\phi_0)^3} + 2b\frac{(\eta/\phi_0)^2}{(1-\eta/\phi_0)^4}\right]^{-1} \tag{3.12}$$

and $\eta_0 = \pi\rho_0\sigma_0^3/6$, $\phi_0 = 1-\eta_0$, $\eta = \pi\rho_1\sigma_1^3/6$ and $\phi = exp\left(-\beta\mu_1^{(ex)}\right)$. Here

$$a = 6 + \frac{3\eta_0\tau(\tau+4)}{1-\eta_0} + \frac{9\eta_0^2\tau^2}{(1-\eta_0)^2}$$

$$b = \frac{9}{2}\left(1 + \frac{\tau\eta_0}{1-\eta_0}\right)^2 \tag{3.13}$$

$$\beta\mu_1^{(ex)} = -ln(1-\eta_0) + \frac{9\eta_0^2}{2(1-\eta_0)^2} - \eta_0 Z_0 + \left[3\eta_0 Z_0 - \frac{3\eta_0(2+\eta_0)}{(1-\eta_0)^2}\right](1+\tau)$$

$$- \left[3\eta_0 Z_0 - \frac{3\eta_0(2+\eta_0)}{2(1-\eta_0)^2}\right](1+\tau)^2 + \eta_0 Z_0(1+\tau)^3 \tag{3.14}$$

$Z_0 = (1+\eta_0+\eta_0^2)/(1-\eta_0)^3$ and $\tau = \sigma_1/\sigma_0$.

The structural properties of the reference system are calculated assuming that the RDFs $g_{ij}^{(ref)}(r)$ can be approximated by the RDFs of the n + 1-component hard-sphere mixture $g_{ij}^{(ref)}(r)$ with n components representing the reference system and one component representing the matrix of the hard-sphere obstacles. To validate this assumption computer simulation have been performed and the results obtained compared against the corresponding theoretical results. Theoretical pair distribution functions have been calculated using the Percus-Yevick approximation. One substantial advantage of the PY approximation is that the closed form analytical expression for the Laplace transforms of the hard-sphere RDFs $G_{ij}^{(ref)}(s)$, which enter into the expressions for the Helmholtz free energy equations 3.5 and 3.6, are available[200].

The chemical potential, μ_i, and pressure, P, of the system are calculated using standard thermodynamical relations, i.e.

$$\mu_i = \mu_i^{(ref)} + \Delta\mu_i \qquad\qquad P = P_{ref} + \Delta P \tag{3.15}$$

where

$$\Delta\mu_i = \frac{\partial}{\partial\rho_{i|_{\{\rho_j \neq i\}}}}\left(\frac{\Delta A_1}{V} + \frac{\Delta A_2}{V}\right) \tag{3.16}$$

$$\Delta P = \sum_{i=1}^{n} \rho_i \Delta\mu_i - \frac{\Delta A_1}{V} - \frac{\Delta A_2}{V} \tag{3.17}$$

3.3 Monte Carlo Simulation Details

To assess the accuracy of the theoretical approach proposed, Monte-Carlo (MC) computer simulations[201] have been performed of the same model as that studied theoretically, thus providing exact model properties and the ability to directly test the theory. The simulated system consists of fluid particles immersed in the environment of a matrix formed by a frozen configuration of randomly dispersed impenetrable hard spheres (HS matrix). We consider the system in a simulation box of a cubic shape with periodic boundary conditions applied along three dimensions. The number of the matrix particles N_0 is varied depending on the packing fraction η_0 of the system and the HS particle diameter $\sigma_0 = \sigma_1/\tau$, where: $\eta_0 = \pi\sigma_0^3 N_0/L^3/6$.

Canonical (NVT) MC simulations[201] were performed to determine the RDFs of the reference system. The fluid-fluid $g_{11}^{(ref)}(r)$ and fluid-matrix $g_{01}^{(ref)}(r)$ RDFs were obtained from NVT simulations of a hard-sphere fluid confined in a disordered hard-sphere matrix at various packing fractions of fluid, η_1, and matrix, η_0, particles. Several different values for the size ratio

of fluid and matrix particles τ have been considered. The number of the matrix particles in the system N_0 are chosen depending on their size, i.e., $N_0 = 10{,}000,\ 6000, 4000\ and\ 2000$, for $\tau = 1, 1/2, 1/3\ and\ 1/5$, respectively. For each set of system parameters, eight random matrix configurations are studied, and the RDFs are averaged over these matrix realizations. Each simulation run consists of $5 \cdot 10^5$ simulation steps for system equilibration and additional 10^5 steps for production. At each step, N_1 trial moves of particles are performed, where N_1 is the number of fluid particles. The maximum displacement for trial moves of fluid particles was adjusted to reach the acceptance rate around 75%. The RDFs were calculated by sampling the configuration every 5 steps. To speed up simulations the linked-cell algorithm with a cell size equal to $2\sigma_1$ was applied[201].

Grand-canonical MC (GCMC) simulations were performed to obtain the average density of a HSM fluid confined in a disordered hard-sphere matrix at a fixed chemical potential and constant temperature[201]. The system was simulated in a box of the size $L = 20\sigma_{11}$and a cut-off distance of $r_c = 10\sigma_1$ used for both the fluid-fluid and fluid-matrix interactions. The number of matrix particles N_0 was adjusted according to the chosen combination of η_0 and τ. Two values of the matrix packing fraction, $\eta_0 = 0.1\ and\ 0.15$, have been studied and are typical values for a wide range of mesoporous materials[141–143]. The screening parameter z_{ij} of the HSM potential (equation 3.3) is $z_{ij} = 1.8/\sigma_1$, indicating that the value of the cut-off distance used is sufficiently large.

All GCMC simulations are performed at the temperature $k_B T/\varepsilon_{11}^{(M)} = 2$, which is very close to the critical temperature of each bulk fluid, but still belongs to the supercritical region. For each set of parameters, the system is fully equilibrated starting from a random initial configuration

with fluid particles of density $\rho *= 0.1$. Each simulation step consists of translational trial moves with the maximum displacement $0.2\sigma_{11}$ and insertion/removal attempts. The ratios of translation and insertion/removal trials are set to 80% and 20% respectively. The total number of fluid particles N_1. The number of steps needed to equilibrate the systems at the considered chemical potentials is typically found to be less than 10^5. Afterwards, the fluid density is averaged during at least 10^5 simulation steps. To improve statistics at substantially low fluid densities ($\rho_1\sigma_{11}^3 < 0.01$), the number of simulation steps is increased to 10^6. In general, the relative error of the densities obtained at the different values of the chemical potential was around 1% of better. For the sake of comparison, a HSM fluid in the bulk is also simulated. Finally, we note that while computer simulations of fluids adsorbed in porous media are challenging as discussed above, the simulations performed herein are carried out at temperatures above the critical temperature therefore they are expected to be sufficiently accurate.

3.4 Results & Discussion

3.4.1 Structure of the Reference System

We present the theoretical predictions for the RDFs of the reference system $g_{11}^{(ref)}(r)$ and $g_{01}^{(ref)}(r)$ in Figures 3.1-3.4 compared against the corresponding computer simulation predictions. Four versions of the model matrix with different porosity ($\phi_0 = 1 - \eta_0$) and different ratios of the sizes of the obstacle and fluid particles τ ($\eta_0 = 0.1058$ and $\tau = 1$ in Fig. 3.1, $\eta_0 = 0.2206$ and $\tau = 1/2$ in Fig. 3.2, $\eta_0 = 0.2972$ and $\tau = 1/3$ in Fig. 3.3, and $\eta_0 = 0.3901$ and $\tau = 1/5$ in Fig. 3.4) are considered. For each set of η_0 and τ wer present the results for the RDFs at high and low values of the fluid packing fraction η. In all cases studied, very good quantitative agreement between the theoretical and computer simulation results can be observed for almost all values of

the distance between the particles r. Slightly less accurate predictions from the theory can be seen only in close vicinity to the contact distance for the RDF $g_{11}^{(ref)}(r)$ at higher densities and for the RDF $g_{01}^{(ref)}(r)$ at both, high and low densities.

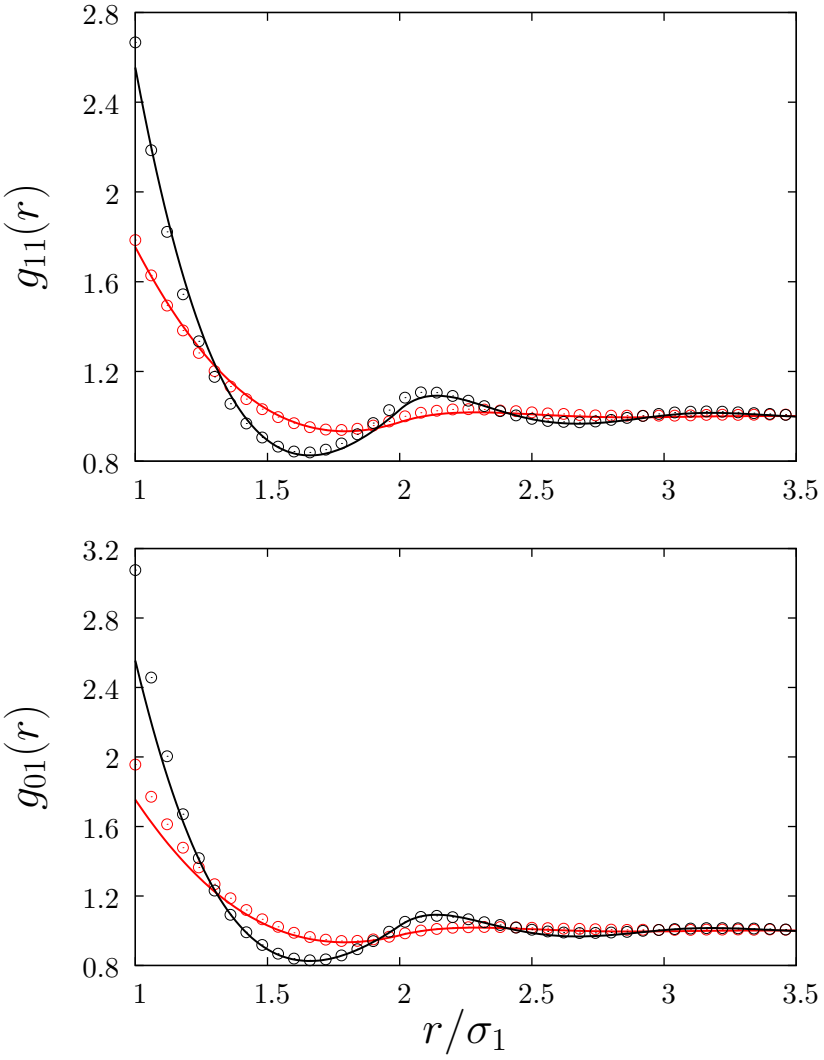

Figure 3.1 Radial distribution function between fluid hard-sphere particles $g_{11}(r)$ (upper panel) and fluid and matrix hard-sphere particles $g_{01}(r)$ (lower panel) for the hard-sphere fluid confined in a random hard-sphere matrix. Lines represent predictions of the theory and symbols stand for computer simulation results. Here $\tau = 1, \eta_0 = 0.1058$, red symbols and lines denote the system with $\eta = 0.1011$ and black symbols and lines denote the system with $\eta = 0.2197$. Here and in Figures 3.2 – 3.4 the error in MC simulation predictions does not exceed the size of the symbols in the figure.

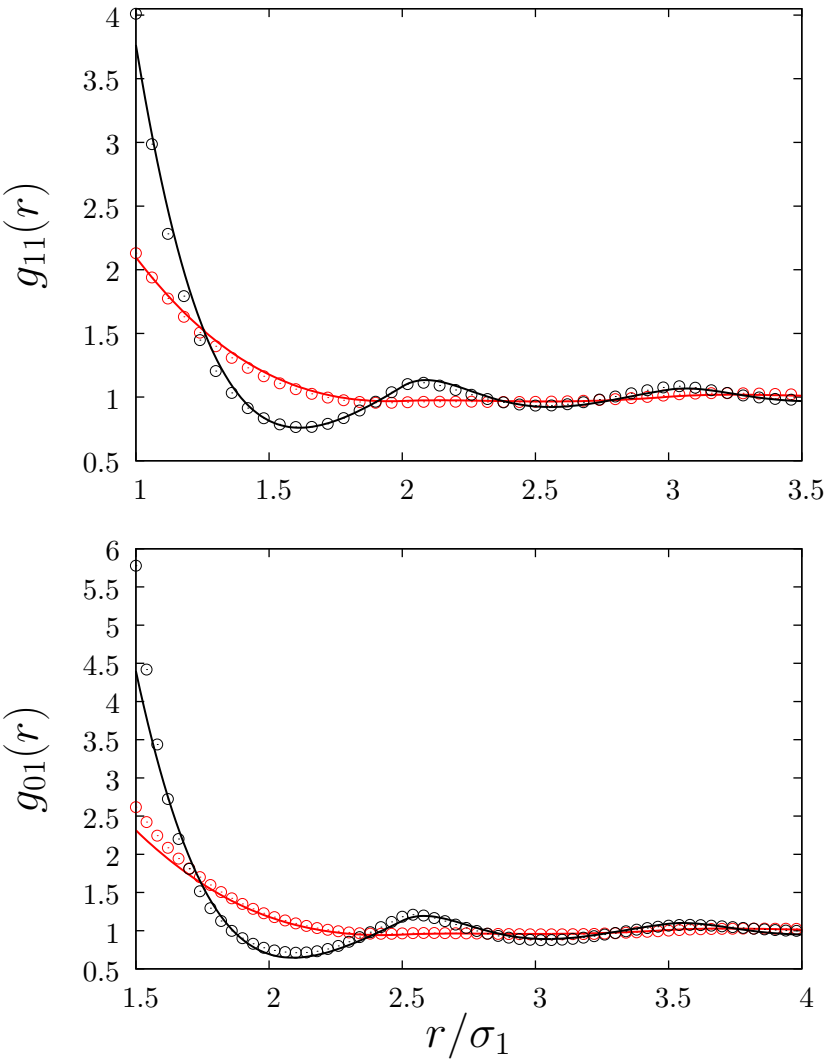

Figure 3.2 Notation is the same as that in Figure 3.1 except that here $\tau = 1/2\,, \eta_0 = 0.2206$, red symbols and lines denote the system with $\eta = 0.0921$ and black symbols and lines denote the system with $\eta = 0.2469$.

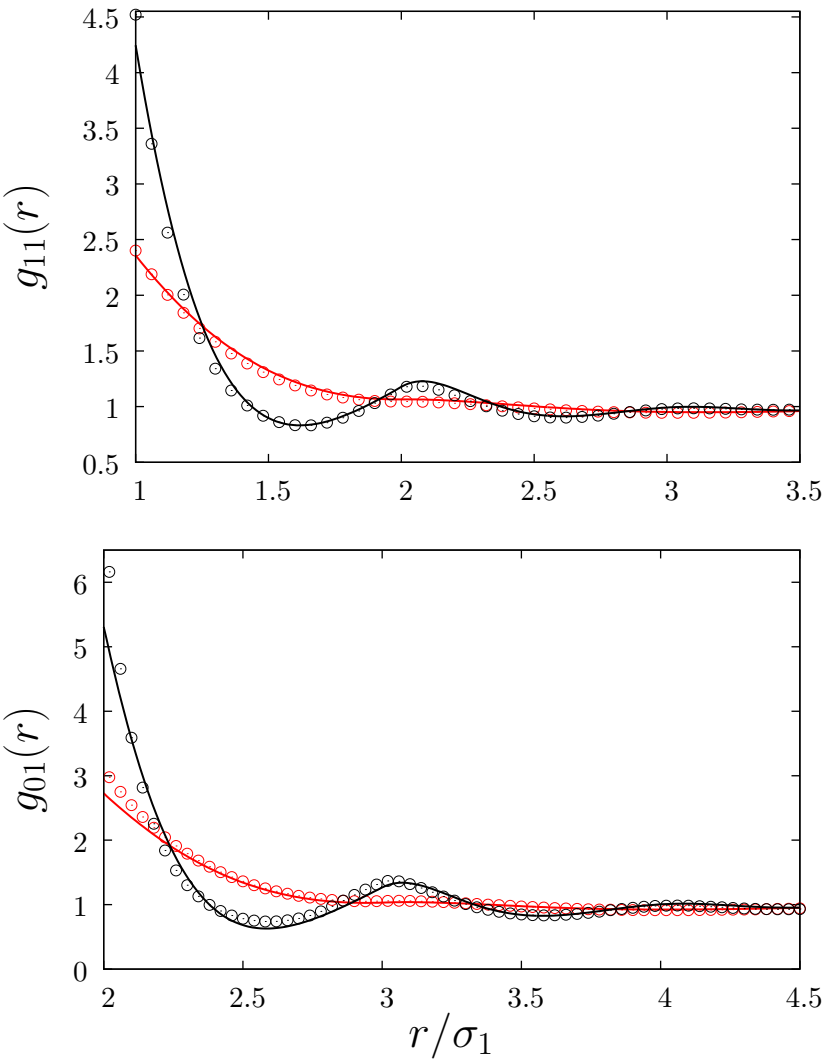

Figure 3.3 Notation is the same as that in Figure 3.1 except that here $\tau = 1/3\,, \eta_0 = 0.2972$, red symbols and lines denote the system with $\eta = 0.0869$ and black symbols and lines denote the system with $\eta = 0.2263$.

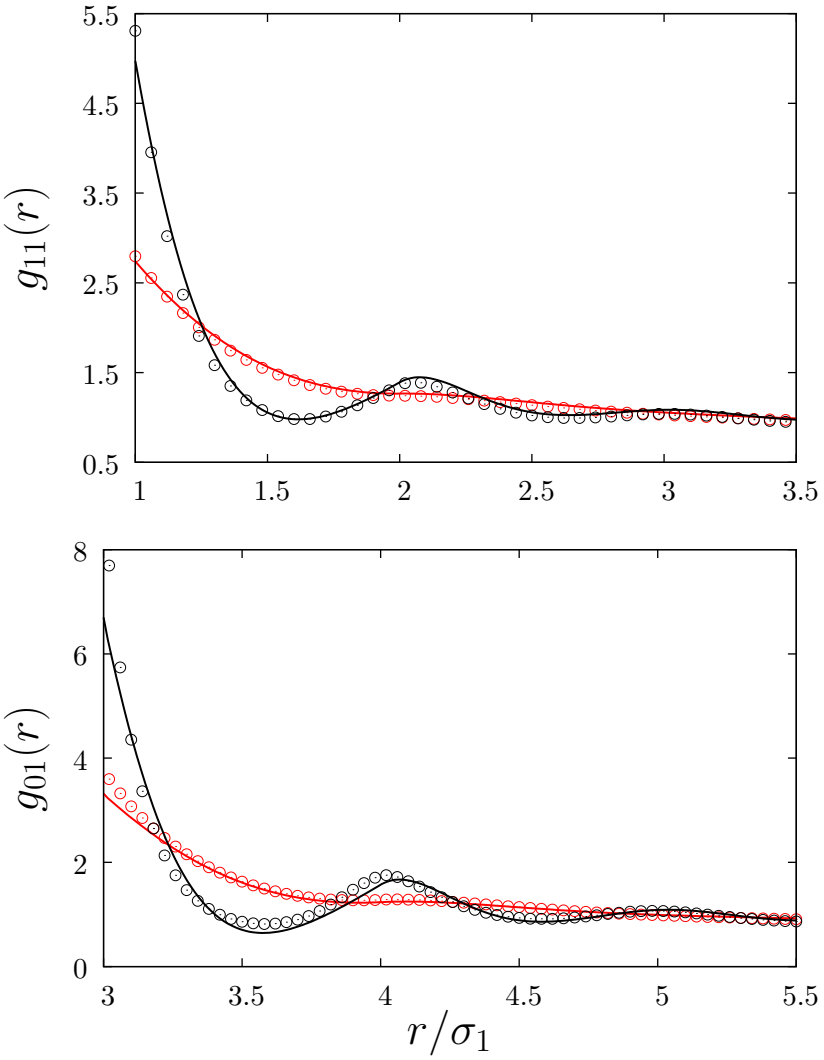

Figure 3.4 Notation is the same as that in Figure 3.1 except that here $\tau = 1/5\,, \eta_0 = 0.3901$, red symbols and lines denote the system with $\eta = 0.0806$ and black symbols and lines denote the system with $\eta = 0.2020$.

3.4.2 Thermodynamics of the Hard-Sphere Morse Liquid Confined in the Matrix

In Figures 3.5 – 3.7 theoretical and computer simulation results for the excess chemical potential as a function of the density of the HSM liquid confined in the matrix are presented. We have studied three different sets of the model parameters for the matrix, i.e., $\eta_0 = 0.1$ and $\tau = 1$ in Fig. 3.5, $\eta_0 = 0.15$ and $\tau = 1$ in Fig. 3.6, $\eta_0 = 0.1$ and $\tau = 3/2$ in Fig. 3.7. For each version of the matrix model parameters three values of the interaction energy $\varepsilon_{01}^{(M)}\left(\varepsilon_{01}^{(M)}/\varepsilon_{11}^{(M)} = 0, 1, 1.5\right)$ are considered. The temperature of the system is $T^* = k_B T/\varepsilon_{11}^{(M)} = 2$.

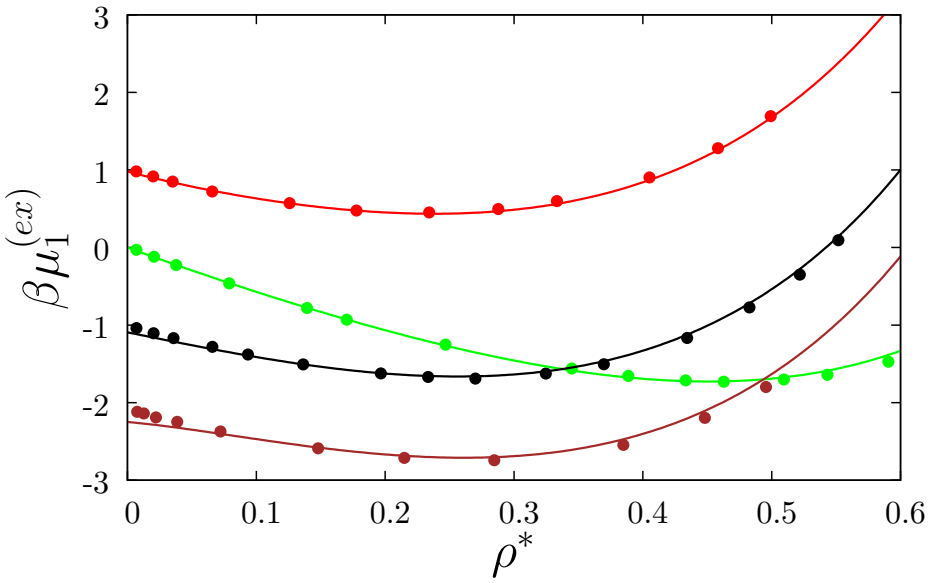

Figure 3.5 Excess chemical potential $\beta\mu_1^{(ex)}$ of the hard-sphere Morse liquid confined in the matrix at $T^* = 2$ as a function of the liquid density ρ^*. Lines show predictions of the theory and symbols stand for computer simulation results. Here $\tau = 1, \eta_0 = 0.1$ and $\varepsilon_{01}^{(M)} = 0$ (red lines and symbols), $\varepsilon_{01}^{(M)}/\varepsilon_{11}^{(M)} = 1$ (black lines and symbols) and), $\varepsilon_{01}^{(M)}/\varepsilon_{11}^{(M)} = 1.5$ (brown lines and symbols). Green line and symbols represent $\beta\mu_1^{(ex)}$ for the hard-sphere Morse liquid in the absence of the matrix and $\rho^* = \rho_1\sigma_1^3$. Here in Figs. 3.6 and 3.7 the error in the MC simulation predictions does not exceed the size of the symbols in the figure.

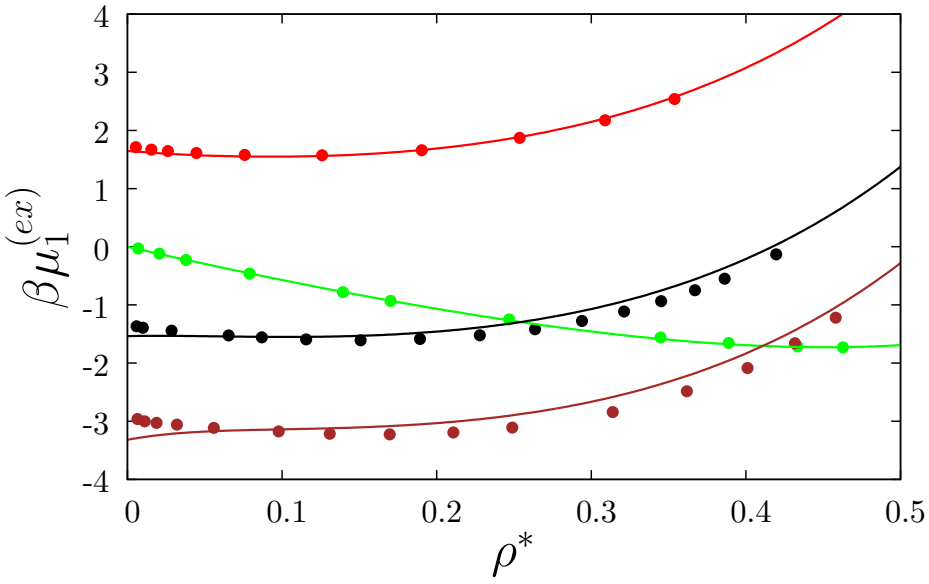

Figure 3.6 Notation is the same as that in Figures 3.5 except that here $\eta_0 = 0.15$.

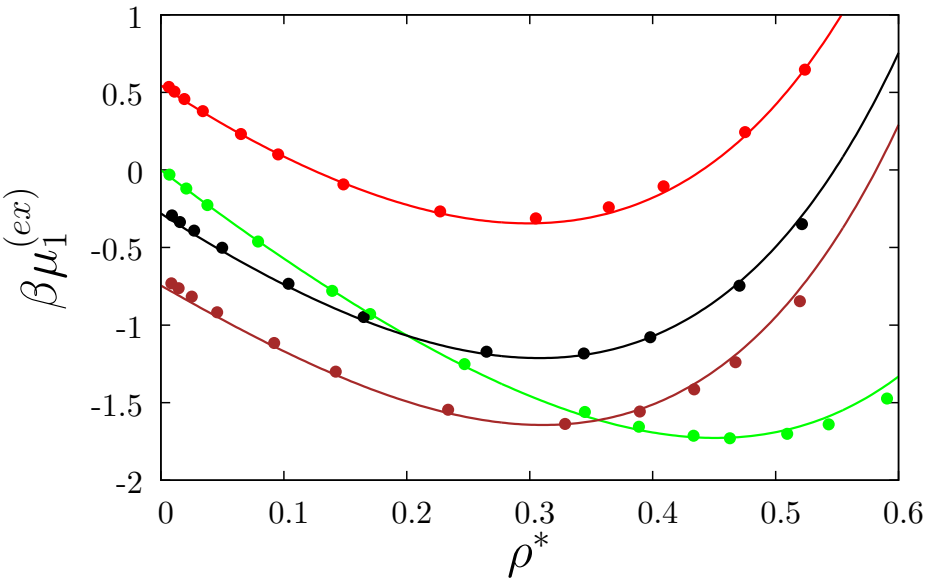

Figure 3.7 Notation is the same as that in Figures 3.5 except that here $\tau = 2/3$.

In general, the agreement between the theoretical predictions and simulations is good. For the model with $\varepsilon_{01} = 0$, the theoretical predictions are very accurate. As the strength of matrix-fluid attraction ε_{01} is increased, the theory provides slightly less accurate results for small values of ρ^* and larger values η_0. This decrease in the accuracy of theoretical results is due to relatively less accurate predictions of the theory $g_{01}(r)$, since at these values of ρ^* and η_0 the contribution to the Helmholtz free energy (equations 3.5 and 3.6) due to the matrix-fluids correlations become larger.

3.4.3 Liquid-Vapor Phase Behavior

Results for the phase behavior of the model are given in Figures 3.8 and 3.9. In Figure 3.8 the liquid-vapor phase diagram of the HSM fluid confined in the hard-sphere matrix at three different values of the matrix packing fraction $\eta_0 = 0, 0.1, 0.2$ and two different values of the matrix-fluid size ratio $\tau = 1, 1/2$ are presented. As one would expect with the increase of the matrix packing fraction the phase envelope and critical point shift in the direction of the lower temperature and

lower densities. This effect is more pronounced for the models with larger values of τ. The effects of the attraction between fluid particles and obstacles of the matrix are shown in Figure 3.9. Here we consider the model with $\eta_0 = 0.1$, $\tau = 1$, and $\varepsilon_{01}^{(M)} = 0$, $\varepsilon_{01}^{(M)}/\varepsilon_{11}^{(M)} = 1$, $\varepsilon_{01}^{(M)}/\varepsilon_{11}^{(M)} = 3$, and $\varepsilon_{01}^{(M)}/\varepsilon_{11}^{(M)} = 6$. With the increase of the strength of fluid-matrix interaction, $\varepsilon_{01}^{(M)}/\varepsilon_{11}^{(M)}$, from 0 to 1 the critical temperature and density increase. With further increase of the strength of the attraction up to $\varepsilon_{01}^{(M)}/\varepsilon_{11}^{(M)} = 6$ the critical temperature noticeably decreases, and the critical density becomes almost twice as large. This behavior can be attributed to the competition between fluid-fluid and fluid-matrix interactions. With the increase of the fluid-matrix attraction, the formation of the liquid phase requires lower temperatures and higher densities.

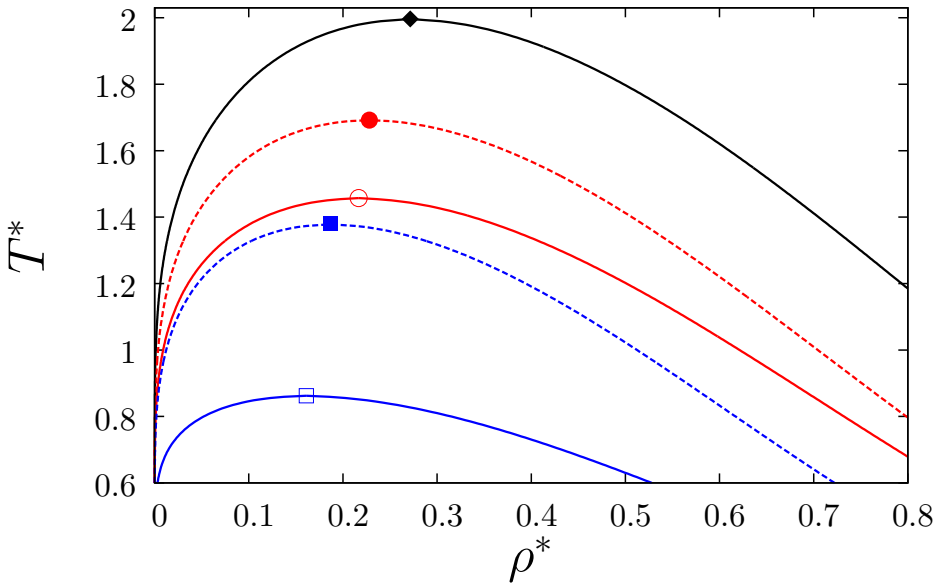

Figure 3.8 Liquid-gas phase diagram of the hard-sphere Morse liquid confined in disordered hard-sphere matrix $\varepsilon_{01}^{(M)} = 0$ with $\eta_0 = 0$ (solid black like and filled diamond), $\eta_0 = 0.1$ and $\tau = 1$ (solid red line and empty circle), $\eta_0 = 0.1$ and $\tau = 1/2$ (dashed red line and filled circle), $\eta_0 = 0.2$ and $\tau = 1$ (solid blue line and empty square), $\eta_0 = 0.2$ and $\tau = 1/2$ (dashed blue line and filled square). Symbols denote position of the critical point. Here $T^* = k_B T/\varepsilon_{11}^{(M)}$ and $\rho^* = \rho_1 \sigma_1^3$.

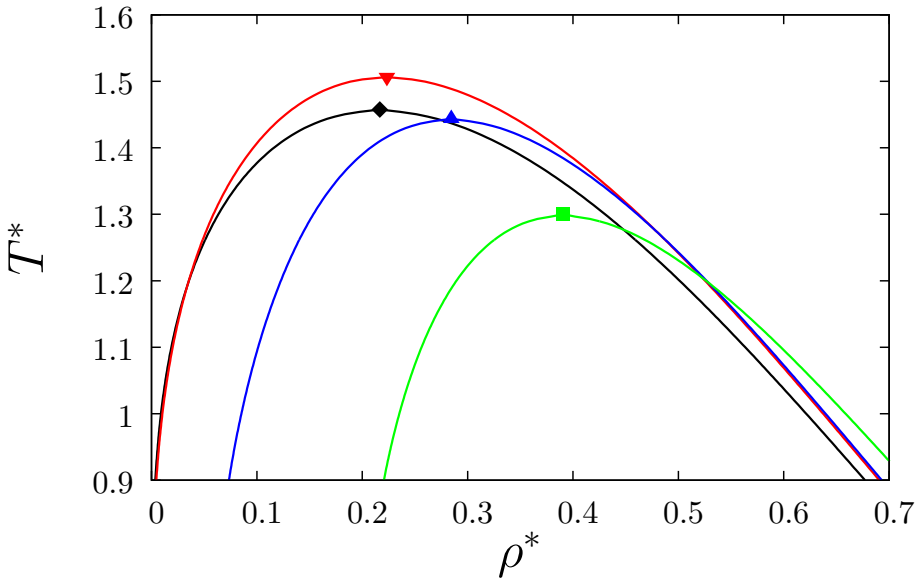

Figure 3.9 Liquid-gas phase diagram of the hard-sphere Morse liquid confined in disordered hard-sphere Morse matrix with), $\eta_0 = 0.1$, $\tau = 1$ and $\varepsilon_{01}^{(M)} = 0$ (black line and diamond), $\varepsilon_{01}^{(M)}/\varepsilon_{11}^{(M)} = 1$ (red line and downward triangle), $\varepsilon_{01}^{(M)}/\varepsilon_{11}^{(M)} = 3$ (blue line and upward triangle), $\varepsilon_{01}^{(M)}/\varepsilon_{11}^{(M)} = 6$ (green line and square). Here $T^* = k_B T/\varepsilon_{11}^{(M)}$ and $\rho^* = \rho_1 \sigma_1^3$.

Finally in Figures 3.10 – 3.14 we compare our theoretical predictions for the liquid-gas phase diagram for the LJ and hard-sphere SW fluids confined in the LJ and hard-sphere matrices against the corresponding computer simulation predictions from the literature[147,200], as computer simulation results for the phase behavior of the HSM model are not available. We note that these computer simulations were carried out taking into account only one matrix realization. In[147], the authors use a truncated LJ potential,

$$U_{11}^{(LJ)}(r) = \begin{cases} 4\varepsilon_{11}^{(LJ)}\left[\left(\frac{\sigma_{11}^{(LJ)}}{r}\right)^{12} - \left(\frac{\sigma_{11}^{(LJ)}}{r}\right)^{6}\right], & for\ r < r_c \\ 0, & for\ r > r_c \end{cases} \tag{3.18}$$

for the interaction between the liquid particles and either the hard-sphere potential or LJ potential analogous to Eq. 18 for the interaction between fluid and matrix particles. Description of the LJ

model is carried out using the BH prescription[126] for the effective hard-sphere sizes σ_{11} and σ_{01}. For the HSM potential energy parameter $\varepsilon_{11}^{(M)}$ we have use the value obtained as a result of fitting of the corresponding computer simulation bulk phase diagrams and for $\varepsilon_{01}^{(M)}$ we have: $\varepsilon_{01}^{(M)} = \varepsilon_{11}^{(M)}\left(\varepsilon_{01}^{(LJ)}/\varepsilon_{11}^{(LJ)}\right)$. Description of the model with hard-sphere SW interaction potential, i.e.

$$U_{11}^{(LJ)}(r) = \begin{cases} \infty, & for\ r < \sigma_{11} \\ -\varepsilon_{11}^{(SW)}, & for\ \sigma_{11} \le r < \lambda\sigma_{11} \\ 0, & for\ \lambda\sigma_{11} \le r \end{cases} \tag{3.19}$$

is carried out following the scheme similar to that used above. Explicit expressions for the temperature dependence of $\varepsilon_{11}^{(M)}$ in the case of LJ fluid and SW fluid are presented in equations 3.20 and 3.21, respectively. In both cases the value of the HSM potential decay parameter was chosen to be $z = 1.8/\sigma_{11}^{(LJ)}$.

The expression for the SW potential fit of $\varepsilon_{11}^{(M)}$ is

$$\varepsilon_{11}^{(M)}(T) = -1.4143(T^*)^3 + 3.6596(T^*)^2 - 2.8747(T^*) + 1.277 \tag{3.20}$$

Where $T^* = k_B T/\varepsilon_{11}^{(SW)}$ and the expression for the LJ potential fit of $\varepsilon_{11}^{(M)}$ is

$$\varepsilon_{11}^{(M)}(T) = -0.6767(T^*)^3 + 1.5671(T^*)^2 - 0.9694(T^*) + 0.6733 \tag{3.21}$$

where $T^* = k_B T/\varepsilon_{11}^{(LJ)}$.

In general, the agreement between the theoretical predictions and simulation data is good. The theory correctly reproduces the effects of the confinement due to changes in both the size ratio of the fluid and matrix particles, shown in Figure 3.10 and in the packing fraction of the matrix η_0,

in Figures 3.11 and 3.14. With the increase of the matrix particles size at constant η_0 the average size of the pores increases, which makes the effects of confinement weaker. As a result, the critical temperature and density of the fluid adsorbed in the matrix with larger obstacles is larger than those of the fluid in the matrix with smaller obstacles, shown in Figure 3.10. On the other hand, increasing the matrix packing fraction η_0 decreases the porosity and increases the effects of confinement. This effect can be seen in Figures 3.11 and 3.14, where due to the increase of η_0 the phase envelope shifts in the direction of lower temperatures and densities. Here theoretical predictions are in relatively good agreement with computer simulation predictions for lower and intermediate values of η_0, i.e., $\eta_0 = 0.5$ and $\eta_0 = 0.1$. In particular, for the SW fluid, the accuracy of our theory is similar to that of Hvozd et al.[189] (Fig. 3.14). In the latter study, the authors apply the BH2 approach directly to the SW model in question.

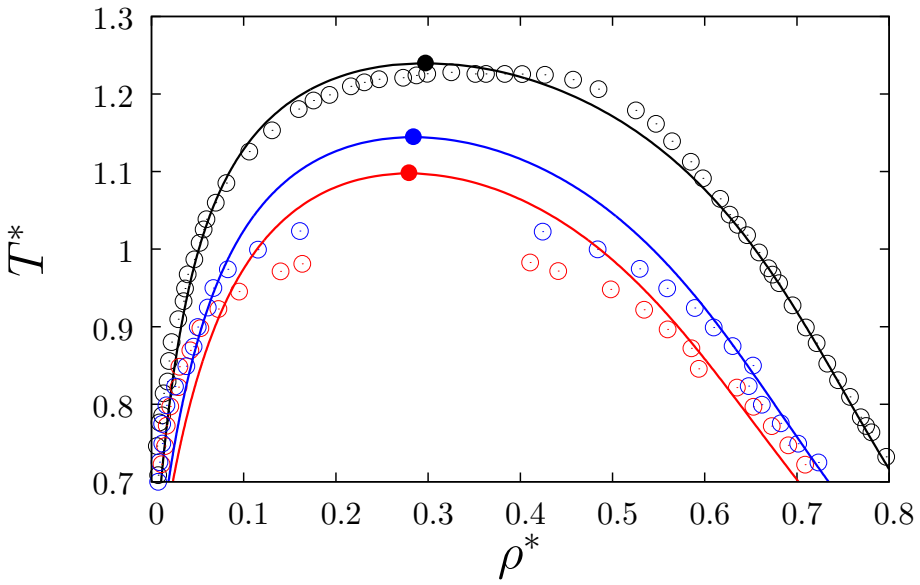

Figure 3.10 Liquid-gas phase diagram of the LJ fluid as shown in Equation 18 in the bulk (black line and empty circles), confined in disordered hard-sphere matrix with $\eta_0 = 0.05$ and $\sigma_1^{(LJ)}/\sigma_0 = 1$ (red line and empty circles) and $\sigma_1^{(LJ)}/\sigma_0 = 2/3$ (blue line and empty circles). Lines represent results of the theory, empty symbols denote computer simulation results[147] and filled symbols denote positions of the critical point. Here $T^* = k_B T/\varepsilon_{11}^{(LJ)}$ and $\rho^* = \rho_1\left(\sigma_1^{(LJ)}\right)^3/(1-\eta_0)$.

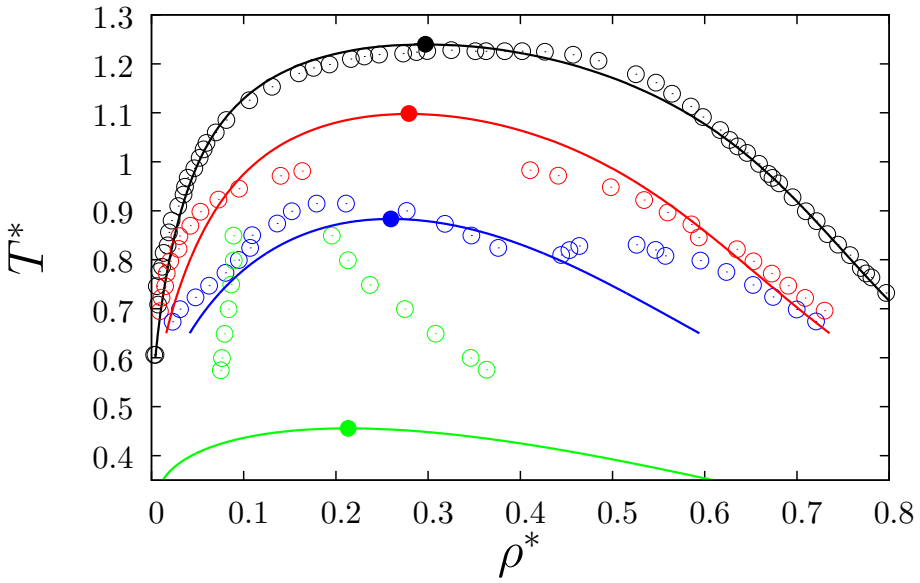

Figure 3.11 Liquid-gas phase diagram of the LJ fluid as shown in Equation 18 in the bulk (black line and empty circles), confined in disordered hard-sphere with $\eta_0 = 0.05$ and $\sigma_1^{(LJ)}/\sigma_0 = 1$ (red line and empty circles), $\eta_0 = 0.1$ (blue line and empty circles) and $\eta_0 = 0.2$ (green line and empty circles). Lines represent results of the theory, empty symbols denote computer simulation results[147] and filled symbols denote positions of the critical point. Here $T^* = k_B T/\varepsilon_{11}^{(LJ)}$ and $\rho^* = \rho_1\left(\sigma_1^{(LJ)}\right)^3/(1-\eta_0)$.

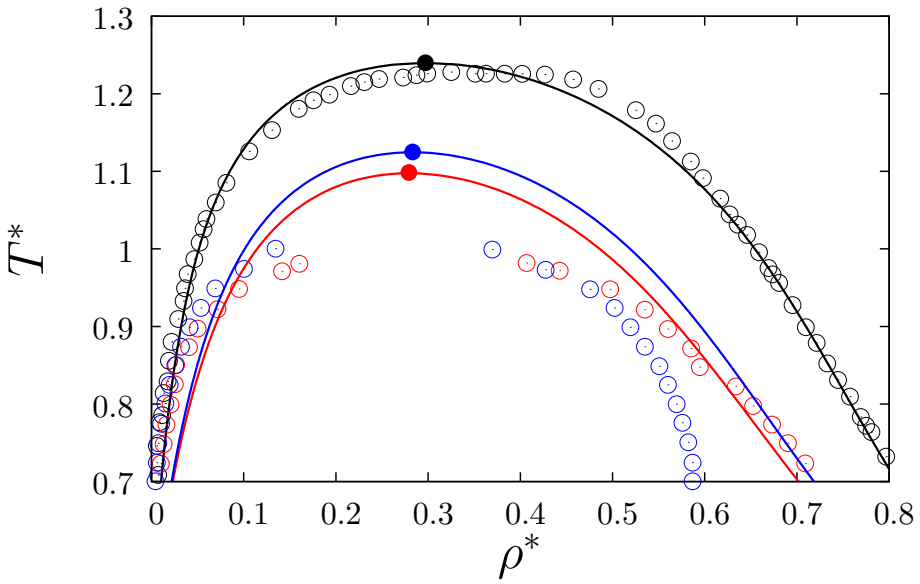

Figure 3.12 Liquid-gas phase diagram of the LJ fluid as shown in Equation 18 in the bulk (black line and empty circles), confined in disordered hard-sphere with $\eta_0 = 0.05$ and $\sigma_1^{(LJ)}/\sigma_0 = 1$ (blue line and empty circles), and confined in disordered LJ matrix with $\eta_0 = 0.05$, $\sigma_1^{(LJ)}/\sigma_0 = 1$ and $\varepsilon_{01}^{(LJ)}/\varepsilon_{11}^{(LJ)} = 1$ (red line and empty circles). Lines represent results of the theory, empty symbols denote computer simulation results[147] and filled symbols denote positions of the critical point. Here $T^* = k_B T/\varepsilon_{11}^{(LJ)}$ and $\rho^* = \rho_1\left(\sigma_1^{(LJ)}\right)^3/(1-\eta_0)$.

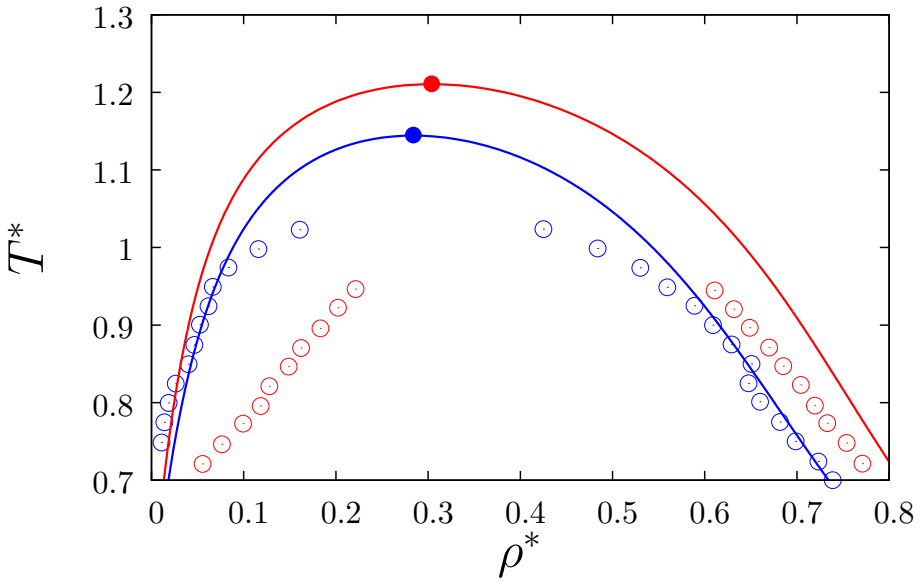

Figure 3.13 Liquid-gas phase diagram of the LJ fluid as shown in Equation 18 confined in disordered hard-sphere with $\eta_0 = 0.05$ and $\sigma_1^{(LJ)}/\sigma_0 = 3/2$ (blue line and empty circles), and confined in disordered LJ matrix with $\eta_0 = 0.05$, $\sigma_1^{(LJ)}/\sigma_0 = 3/2$ and $\varepsilon_{01}^{(LJ)}/\varepsilon_{11}^{(LJ)} = 1.25$ (red line and empty circles). Here $T^* = k_B T/\varepsilon_{11}^{(LJ)}$ and $\rho^* = \rho_1\left(\sigma_1^{(LJ)}\right)^3/(1-\eta_0)$.

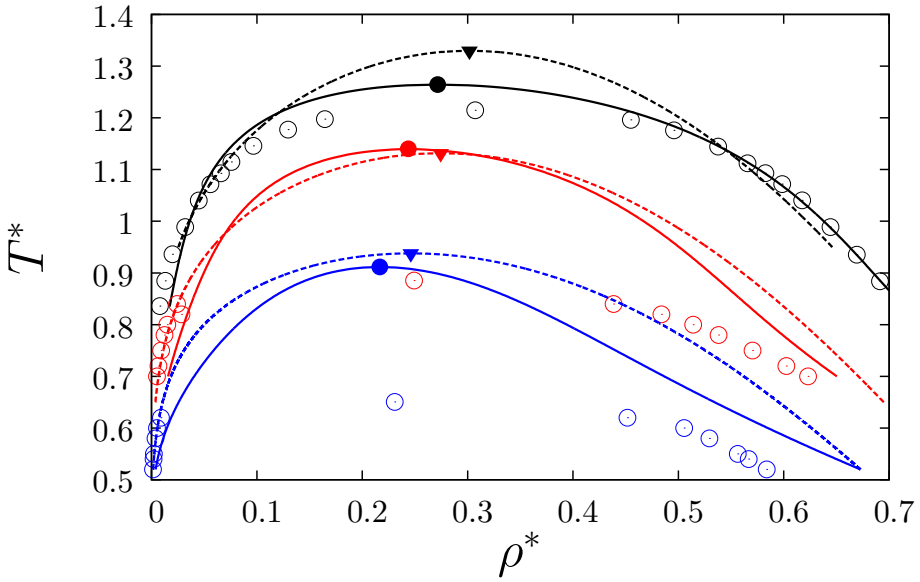

Figure 3.14 Liquid-gas phase diagram of hard-sphere SW liquid as shown in Equation 19 in the bulk (black lines and empty circles), confined in disordered hard-sphere matrix with $\tau = 1$ and $\eta_0 = 0.05$ (red lines and empty circles), $\eta_0 = 0.1$ (blue lines and empty circles), Solid and dashed lines represent results of the present BH2 theory and the version of the BH2 theory[189], empty circles stand for computer simulation results[198] and filled symbols denote the position of the critical points. Here $T^* = k_B T/\varepsilon_{11}^{(LJ)}$ and $\rho^* = \rho_1\left(\sigma_1^{(LJ)}\right)^3/(1-\eta_0)$.

For $\eta_0 = 0.1$ computer simulation for the LJ fluid in the matrix[147] shows the existence of the two phase transitions with two critical points: one located at lower density and higher temperature and the other at higher density and lower temperature. At the same time, MC computer simulations carried out for the SW fluid in the matrix[198] with the same value of η_0, shows the appearance of a single phase transition. In both cases, the theory predicts the existence of only one phase transition. However, we note that the phase behavior of the fluid adsorbed in the porous media is very sensitive to even subtle differences in the matrix structure and for two different realizations of the matrix with the same porosity, size of the obstacles and distribution of the pore sizes, computer simulations can produce the phase diagram with and without phase transitions[147]. Therefore, the existence of the two phase transitions for the LJ model at hand is still questionable[195,202]. With further decrease of the matrix porosity up to $\eta_0 = 0.2$, the theoretical phase envelope shifts towards the lower temperatures and densities as shown in Figure 3.11. In contrast, the computer simulation phase diagram shifts in the direction of slightly higher temperatures and lower densities and becomes substantially narrower. We believe that this disagreement can be explained by the sensitivity of the phase behavior to the matrix structure, generated in the computer simulations. Next in Figures 3.12 and 3.13, we compare predictions of the theoretical predictions and simulation results for the effects of attraction between LJ fluid and matrix particles. We consider the case of equal and different sizes of the fluid and matrix particles in Figures 3.12 and 3.13, respectively. In both cases, an increase in the fluid-matrix attraction leads to a shift of the phase diagram to higher temperatures. At the same time, while the theoretical phase diagram shifts to higher densities, the computer simulation phase diagram for $\varepsilon_{01}^{(LJ)}/\varepsilon_{11}^{(LJ)} = 1$ is shifted in the opposite direction to lower densities, shown in Figure 3.12 and for $\varepsilon_{01}^{(LJ)}/\varepsilon_{11}^{(LJ)} = 1.25$ it is moved towards the higher densities, shown in Figure 3.13. In our opinion this

nonmonotonic behavior can be also attributed to the difficulties in performing computer simulations of the systems in question, in particular due to insufficient number of matrix realizations accounted.

3.5 Conclusions

In this chapter we propose a simple analytical theory for thermodynamics of the multicomponent simple liquid mixtures confined in the porous media. The media is represented by the matrix of hard-sphere obstacles randomly placed in a configuration of a HS fluid quenched at equilibrium. A simple fluid mixture is modeled by the n-component hard-sphere mixture with additional attractive Morse potential between liquid particles and between the particles of the matrix and liquid particles. For the theoretical description, we combine SPT and second-order BH perturbation theory, appropriately modified to account for the absence of the interaction between the matrix particles. SPT is used to describe the thermodynamics of the reference system. We have shown that the structure of the reference system can be accurately predicted using PY RDFs of the n + 1-component hard-sphere mixture with the n component representing the fluid and one component representing the matrix obstacles. Agreement between theoretical and computer simulation predictions is very good for fluid-fluid RDFs and slightly less accurate for fluid-matrix RDFs at all densities and size ratios studied. It is also demonstrated that BH2 perturbation theory for the n + 1- component HSM liquid can be used to give sufficiently accurate predictions for the thermodynamics of the n-component fluid con- fined in the matrix with HSM obstacles. Theoretical predictions for the chemical potential are in a very good agreement for the model with weak fluid-matrix attraction and becomes less accurate with the increase of the fluid-matrix attraction and matrix density. Our SPT-BH2 approach is able to correctly predict the effects due to the changes in the matrix density, fluid-matrix particles size ratio and strength of the fluid-

matrix interaction of the liquid-gas phase behavior. With a minimal adjustment of our HSM potential we were able to reproduce, with a reasonable accuracy, computer simulation results for the phase behavior of the LJ and hard-sphere SW fluids confined in the porous media. Due to its simplicity, the theory can be used to study the properties of a simple fluid mixture with any number of components adsorbed in the hard-sphere matrix. Taking into account the isomorphism of the fluid adsorbed in disordered hard- sphere matrix[184] we expect that our theory can be applied also to describe the properties of the fluids confined in the matrices with the other hard-core morphologies.

Chapter 4

Predicting the Properties of Fatty Acid Methyl Esters and Sulfur Molecules for Greener Petroleum

4.1 Introduction

With increasing demand to lower greenhouse gas emissions and minimize environmental impacts, finding alternatives to petroleum is a priority. The main compounds used to create greener alternative fuels, or biodiesels, are fatty acid methyl ester (FAME) molecules.[27,203] Biodiesel has the possibility of lowering greenhouse gas emissions by approximately half compared to equivalent petroleum fuels.[11] Knowing the phase behavior of multiple FAME molecules and their mixtures would allow the composition of the biodiesel to be tailored based to the implementation needs. Experimental studies of such an extensive selection of FAME molecules would be far too time intensive in order to have a full picture of the possible FAME combinations.

Despite the positives of switching to biodiesel, the cost of biodiesel is almost double the cost of traditional fuels, meaning that until the cost can be lowered, ways to reduce the environmental impact of petroleum is also a priority. One of the main impurities in petroleum are sulfur molecules, which impair the effectiveness of emission control systems and generate sulfur dioxide. Additionally, cyclic sulfur molecules, like thiophene, are not easily removed through typical desulfurization processes, such as hydrodesulphurization.[204] With increasing environmental regulations, sulfur impurities make it difficult for industries to achieve the required lower pollutant levels. Therefore, knowing the solubility of cyclic sulfur molecules, especially thiophene, in various other compounds including carbon dioxide is vital in lowering the environmental impact of traditional petroleum without significantly increasing its production costs.

To move toward greener fuels, data on the phase behavior of FAME molecules and the solubility of sulfur molecules allows increased environmental efficiency from both sides of the petroleum spectrum. As little is known about these molecule classes, it would be extremely time and labor intensive to gain a full picture of these systems through experimental studies. Furthermore, both FAME and sulfur-based molecules have limited experimental data available, making simple equation of state models ineffective at furthering the information available on these systems.

A molecular-based equation of state, such as the statistical associating fluid theory (SAFT) is considered here to develop a predictive model for both FAME and sulfur molecules. FAME molecules have been represented using SAFT for potentials of variable range, or SAFT-VR, by multiple groups[29,30] with reasonable agreement, though larger deviations were often seen at lower temperatures. Additionally, FAME molecules have been considered using the SAFT-γ group contribution approach[28]. While the deviations in vapor pressure reported are reasonable, based on the figures in the SAFT-γ work, it seems that the saturated liquid density deviations are larger than those for the vapor pressure. soft-SAFT has also been used to study FAME systems by multiple groups[27,31,32] with success. However, in the FAME mixtures considered (specifically those with alcohols and carbon dioxide) binary interaction parameters were fitted to each individual mixture and unable to be used transferably. Therefore, the soft-SAFT models cannot be expanded without further fitting of binary interaction parameters.

Perturbed chain SAFT (PC-SAFT) has considered FAME molecules[35], but its parameters had average absolute deviations greater than 10%, which are higher than typically considered reasonable. The PC-SAFT model was expanded to consider additional FAME molecules[33], but the deviations remained higher than 10%. PC-SAFT is also the main version of SAFT that has studied

sulfur molecules. In one study[20], the vapor pressure and saturated liquid density of pure sulfur molecules were reasonably represented, but even with binary interaction parameters fit to the mixture systems studied, VLE was predicted in cases where the experimental data showed LLE. Another study considered sulfur molecules and ionic liquids with PC-SAFT[205], but despite using binary interaction parameters had similar issues with predicting VLE for the phase behavior when the experimental data showed LLE.

Therefore, to broadly predict the thermodynamic properties and phase behavior of FAME and sulfur molecules and their respective mixtures, here we explore the use of the group contribution SAFT-VR (GC-SAFT-VR)[22,121] approach. The GC-SAFT-VR model allows functional groups to be parameterized and then used transferably to construct other molecules that can be represented as a heteronuclear chain. The FAME molecules are built from functional groups that were parameterized in previous works.[11,22,120] However, for the sulfur molecules, additional functional groups[10] must be introduced to represent these molecules. GC-SAFT-VR fits all interactions to the pure components meaning that all mixtures are purely predictive. The only exception is for mixtures with carbon dioxide, as carbon dioxide is not included in other molecules, any interactions with carbon dioxide must be fit to mixture data. However, in order to retain some predictive power, the interactions with carbon dioxide are only fit to one set of experimental data, thus allowing all other combinations to be fully predicted.

4.2 Models & Theory

The GC-SAFT-VR approach[22] represents each functional group in a molecule by tangentially bonded segments with individual size and energy parameters. All of the expressions for GC-SAFT-VR were provided in Chapter 2 and thus not repeated here.

All of the parameters used to describe the FAME molecules were originally developed for other molecule types such as alkanes, alkenes, and esters[22,120]. We utilized a cross interaction with carbon dioxide from previous work[11] as well, which made the work for the FAME molecules purely predictive. Specifically we consider methyl oleate and its mixtures which was incorrectly represented by Haley et al. in the initial work.[11]

Cyclic sulfur molecules are also considered in this chapter. While sulfur molecules were previously parameterized in another work[10], the parameters for thiophene were not being used in a transferable fashion as is the point of GC-SAFT-VR. They have been refit in this work. Now that the parameters for thiophene have been corrected, the approach can accurately predict the pure fluid properties and phase behavior of thiophene mixtures.

4.3 Results & Discussion

One of the innate benefits of GC-SAFT-VR is the ability to use parameters for functional groups transferably between multiple molecule classes, i.e., any parameterized functional groups should be able to accurately predict the properties of other molecules containing these functional groups. Here we test the transferable nature of the parameters by using them to predict the properties of FAME molecules and their mixtures. While FAME molecules were previously considered by Haley et al.[11], here we expand upon this work to consider FAME molecules that contain a double bonded carbon in the middle of the molecule. Specifically, we consider methyl oleate and its mixtures with carbon dioxide, which is one of the main FAME molecules included in biodiesels.

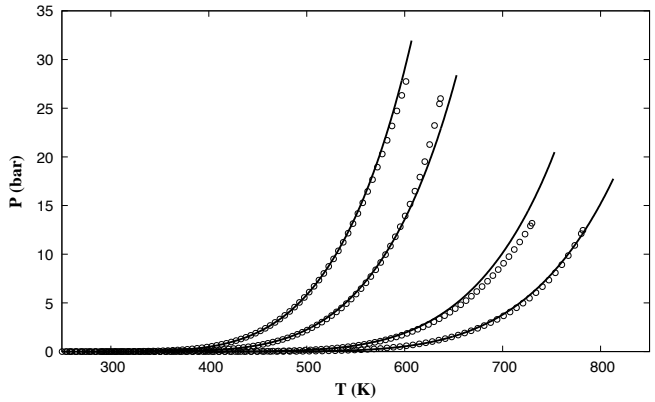

Figure 4.1. Comparison between theoretical predictions from the GC-SAFT-VR equation and the ThermoData Engine (TDE) data for the vapor pressure of methyl caproate, methyl caprylate, methyl myristate, and methyl oleate (left to right). Symbols correspond to the TDE data[206] and the solid lines to the theoretical results.

The parameters needed to describe the FAME molecules and their mixtures with carbon dioxide are given Tables 4.1 - 4.3 from the work of Peng et al.[22,120] Figure 4.1 shows the predicted vapor pressure for four pure FAME molecules, methyl caproate, methyl caprylate, methyl myristate, and methyl oleate. As can be seen form the figure, reasonable agreement between the predictions and the experimental data is observed, with the exact deviations reported in Table 4.4. In Table 4.4, the average absolute deviation (AAD) values obtained show an improvement over the initial work [11]. This improvement is likely due to utilizing different experimental datasets and using consistent functional group parameters across all molecules in this work.

Table 4.1. GC-SAFT-VR parameters for the segment size and segment number of carbon dioxide and the functional groups used to describe the FAME molecules studied.

Groups	**σ_{ij} (Å)**	**m_j**
CO_2	2.7739	2.000
CH_3	3.737	0.667
CH_2	4.041	0.333
cis-CH=CH	3.349	0.856
C=O	3.496	0.580
OCH_3 (ester)	3.078	1.330
OH (terminal)	5.299	0.176

Table 4.2. GC-SAFT-VR segment-segment dispersion energy well depth parameters $\varepsilon_{ki,jl} / k_B$ (K) for carbon dioxide and the functional groups used to describe the FAME molecules studied.

Type	**CO_2**	**CH_3**	**CH_2**	***cis*-CH=CH**	**C=O**	**OCH_3 (ester)**	**OH (terminal)**
CO_2	179.317	204.951	206.251	155.496	268.797	137.977	309.677
CH_3	204.951	234.250	235.735	177.725	307.223	157.702	353.946
CH_2	206.251	235.735	237.230	178.825	309.171	158.702	356.191
cis-CH=CH	155.496	177.725	178.825	134.840	233.090	119.648	268.539
C=O	268.797	307.223	309.171	233.090	402.929	206.829	464.207
OCH_3 (ester)	167.237	191.144	192.356	145.021	250.689	128.682	288.814
OH (terminal)	309.677	353.946	356.191	268.539	464.207	238.284	534.805

Table 4.3. GC-SAFT-VR segment-segment dispersion energy range parameters $\lambda_{ki,lj}$ for carbon dioxide and the functional groups used to describe the FAME molecules studied.

Type	**CO_2**	**CH_3**	**CH_2**	***cis*-CH=CH**	**C=O**	**OCH_3 (ester)**	**OH (terminal)**
CO_2	1.527	1.506	1.505	1.729	1.729	1.594	1.506
CH_3	1.506	1.492	1.583	1.683	1.685	1.566	1.494
CH_2	1.505	1.583	1.667	1.771	1.586	1.662	1.569
cis-CH=CH	1.729	1.683	1.771	1.896	1.894	1.781	1.650
C=O	1.729	1.685	1.586	1.894	1.891	1.558	1.652
OCH_3 (ester)	1.594	1.566	1.662	1.781	1.558	1.655	1.554
OH (terminal)	1.506	1.494	1.569	1.650	1.652	1.554	1.495

Table 4.4. Average absolute deviations in vapor pressure and saturated liquid density for the FAME molecules studied.[30,207–209]

Molecule	Formula	% AADP	% AADρ_l
Methyl Caproate	$C_7H_{14}O_2$	1.68	0.37
Methyl Caprylate	$C_9H_{18}O_2$	1.23	0.25
Methyl Caprate	$C_{11}H_{22}O_2$	1.66	0.33
Methyl Laurate	$C_{13}H_{26}O_2$	1.79	0.27
Methyl Myristate	$C_{15}H_{30}O_2$	3.22	0.26
Methyl Palmitate	$C_{17}H_{34}O_2$	6.27	0.34
Methyl Oleate	$C_{19}H_{36}O_2$	3.99	2.96
Methyl Stearate	$C_{19}H_{38}O_2$	7.25	0.75
Average		3.39	0.69

In the work of Haley et al.[11], the functional groups used to describe the double bond in methyl oleate was incorrectly represented by utilizing a $CH{=}CH_2$ functional group for the double bond, whereas it should be a CH=CH functional group. Here we correct this error and also consider binary mixtures of molecules with methyl oleate. First, in Figure 4.2 we the binary mixture of methyl oleate and methyl stearate at 472.15 K is shown. In contrast to the original work, no azeotropic behavior occurs, suggesting separation is more reasonable than was previously predicted.

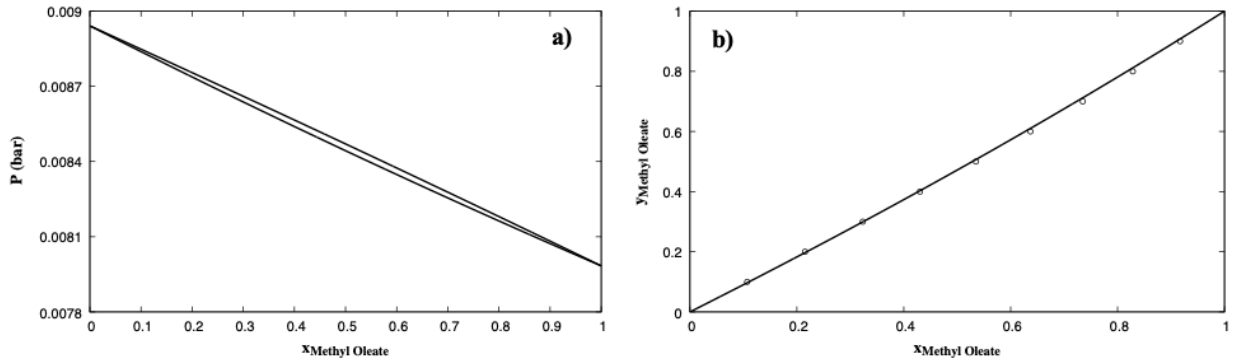

Figure 4.2. *Pxy* (a) and *xy* (b) diagram for the methyl oleate + methyl stearate binary mixture at 472.15 K. Solid lines represent the theoretical predictions and the symbols represent the experimental data[207].

Figure 4.3 considers the mixture of carbon dioxide with four different FAME molecules. Specifically, the *Pxy* diagram of carbon dioxide with methyl myristate, methyl oleate, methyl

stearate, and methyl palmitate were determined at constant temperature slices of 313.15 K, 323.15 K, 333.15 K, and 343.15 K. While the results show an overprediction of the critical point, this is typical of analytical equations of state. Better agreement could likely be obtained for these systems by fitting binary interaction parameters between different groups,[32] this was not done in order to retain a predictive model.

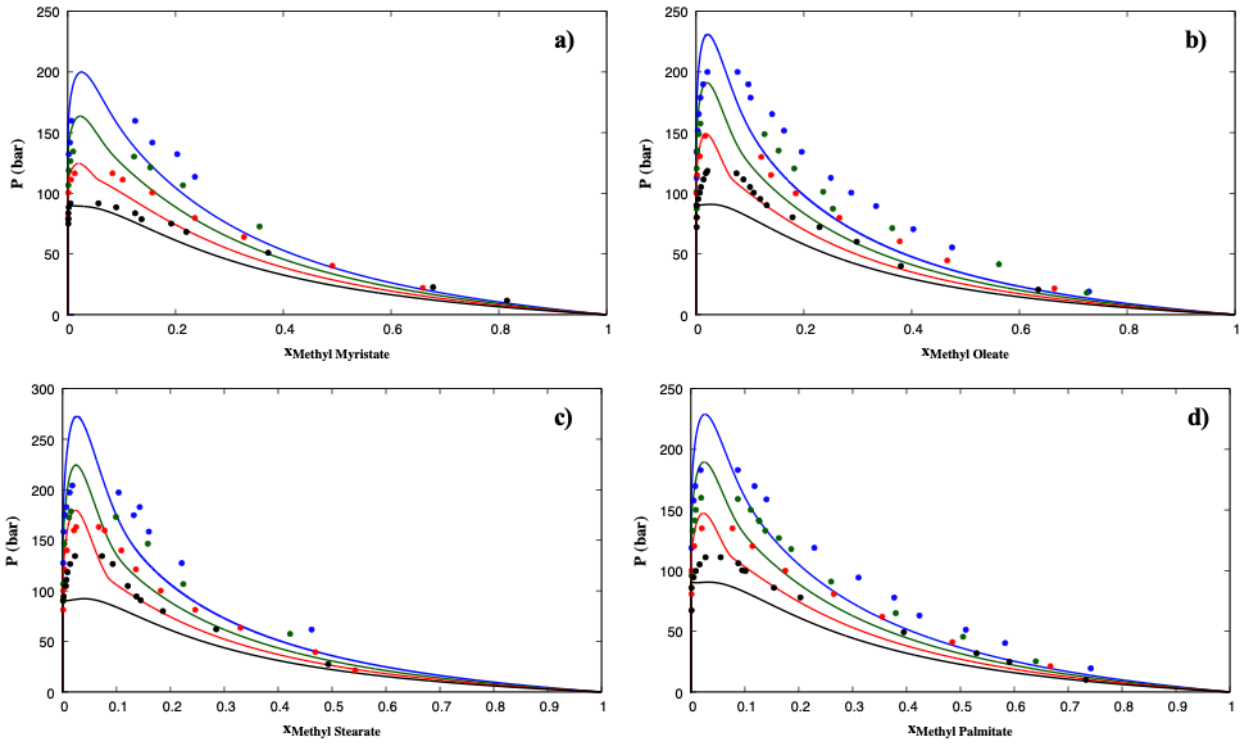

Figure 4.3. Constant temperature *Pxy* slices of the a) methyl myristate, b) methyl oleate, c) methyl stearate, and d) methyl palmitate + CO_2 phase diagrams at 313.15 K, 323.15 K, 333.15 K, 343.15 K (bottom to top). Solid lines represent the predictions from the GC-SAFT-VR equation, and the symbols show the experimental data[210].

We next consider both sulfur containing molecules and their mixtures. As for the FAME molecules, the sulfur molecules have been considered previously,[10] but the parameters used were not represented in a transferable fashion. Since utilizing transferable parameters for functional groups across molecule types is necessary to create predictive models using GC-SAFT-VR, these

parameters are refitted in this work. All parameters used for the sulfur molecules are shown in Tables 4.5-4.7. The main component considered here is thiophene as the functional groups used for thiophene previously were incorrect as a consistent set of functional group parameters were not used across multiple molecules, meaning the parameters were not used transferably. In Figure 4.4 we show the vapor pressure and saturated liquid density of thiophene in good agreement with the experimental data.

Table 4.5. GC-SAFT-VR parameters for the segment size σ and segment number *m* of each functional group studied.

	Σ (Å)	m_i
-S-	3.919	0.850
CH= (Thiophene)	3.511	0.350
CH= (Benzene)	3.028	0.619
CH= (Alkylbenzene)	3.928	0.350
C=	2.112	0.382

Table 4.6. GC-SAFT-VR segment-segment dispersion energy range parameters $\lambda_{ki,lj}$. Values denoted with a * do not utilize Lorentz-Bethelot combining rules.

	-S-	CH= (Thiophene)	CH= (Benzene)	CH= (Alkylbenzene)	C=
CH_3	1.51701	1.37586	1.60988	1.49148	1.38398
CH_2	1.57280*	1.47417	1.70485	1.58024	1.50425
CH	1.74358	1.61843	1.86298	1.71841	1.68251
CH_2=CH	1.55381	1.41152	1.65393	1.52768	1.42865
OH terminal	1.51450	1.39825	1.58968	1.49329	1.40889
CO_2	1.50401*	1.37307	1.64570	1.50548	1.38199
-S-	1.54086	1.40447	1.63435	1.51590	1.41899
CH= (Thiophene)	1.40447	1.25224	1.48522	1.37831	1.22993
CH= (Benzene)	1.63435	1.48522	1.75536	1.60607	1.52422
CH= (Alkylbenzene)	1.51590	1.37831	1.60607	1.49099	1.38674
C=	1.41899	1.22993	1.52422	1.38674	1.19284

Table 4.7. GC-SAFT-VR segment-segment dispersion energy well depth parameters $\varepsilon_{ki,lj}/k_B$ (K). Values denoted with a * do not utilize Lorentz-Bethelot combining rules.

	-S-	CH= (Thiophene)	CH= (Benzene)	CH= (Alkylbenzene)	C=
CH_3	404.974	209.610	185.238	293.442	153.861
CH_2	407.542	210.939	186.412	295.302	154.837
CH	264.619	136.963	121.038	191.741	100.536
CH_2=CH	391.878	202.831	179.247	283.952	148.886
OH terminal	611.907	316.716	279.890	443.384	232.481
CO_2	354.322	183.393	162.069	256.739	134.617
-S-	700.125	362.376	320.241	507.306	265.997
CH= (Thiophene)	362.376	187.562	165.753	262.575	137.677
CH= (Benzene)	320.241	165.753	146.480	232.044	121.669
CH= (Alkylbenzene)	507.306	262.575	232.044	367.590	192.740
C=	265.997	137.677	121.669	192.740	101.060

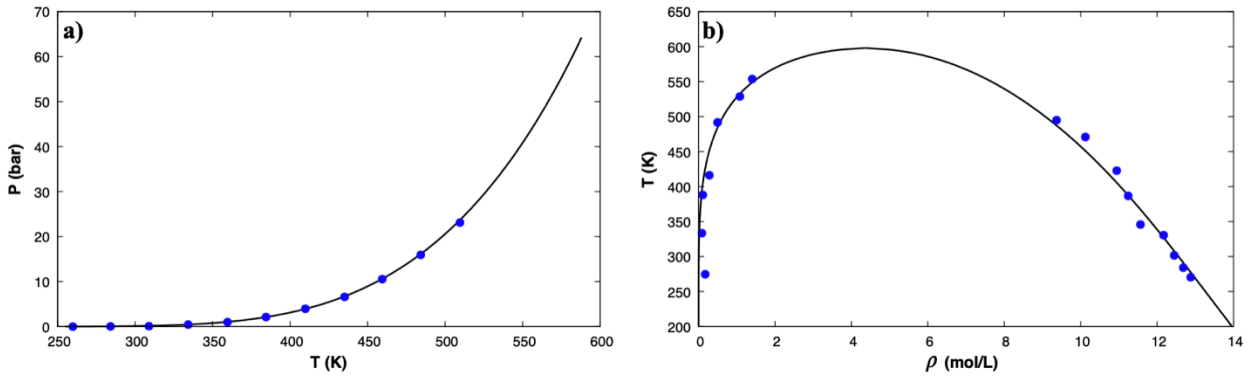

Figure 4.4. GC-SAFT-VR correlation for a) the vapor pressure curve and b) the saturated liquid density for thiophene (C_4H_4S) using the parameters determined in this work as compared to experimental data (symbols).[206]

Figure 4.5 shows binary mixtures with thiophene and alkanes and alkenes, including hexane, hexene, heptane, and methylbutane. Each of the systems studied show good agreement with the experimental data. Namely, GC-SAFT-VR is able to correctly predict the presence and lack of an azeotrope in each of the mixtures, demonstrating that this could be expanded to other types of branched and linear alkanes and alkenes with thiophene. With the accurate predictions of thiophene with alkanes, we next consider thiophene mixed with other cyclic molecules.

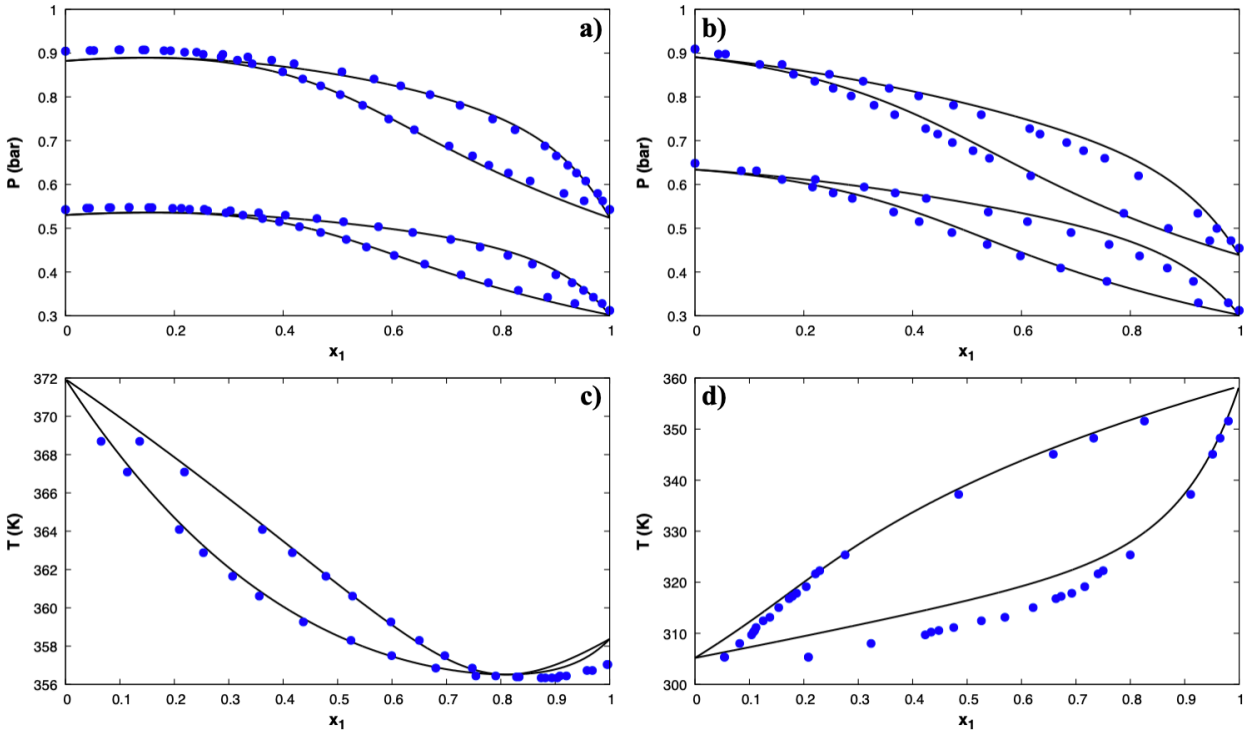

Figure 4.5. Phase behavior of thiophene (1) + (a) hexane (2) at 338.15 K and 323.15 K (top to bottom), (b) hexene (2) at 333.15 K and 323.15 K (top to bottom), (c) heptane (2) at 1.0133 bar, and (d) 2-methylbutane (2) at 1.0133 bar. The solid lines represent the GC-SAFT-VR predictions and the symbols the experimental data[211,212].

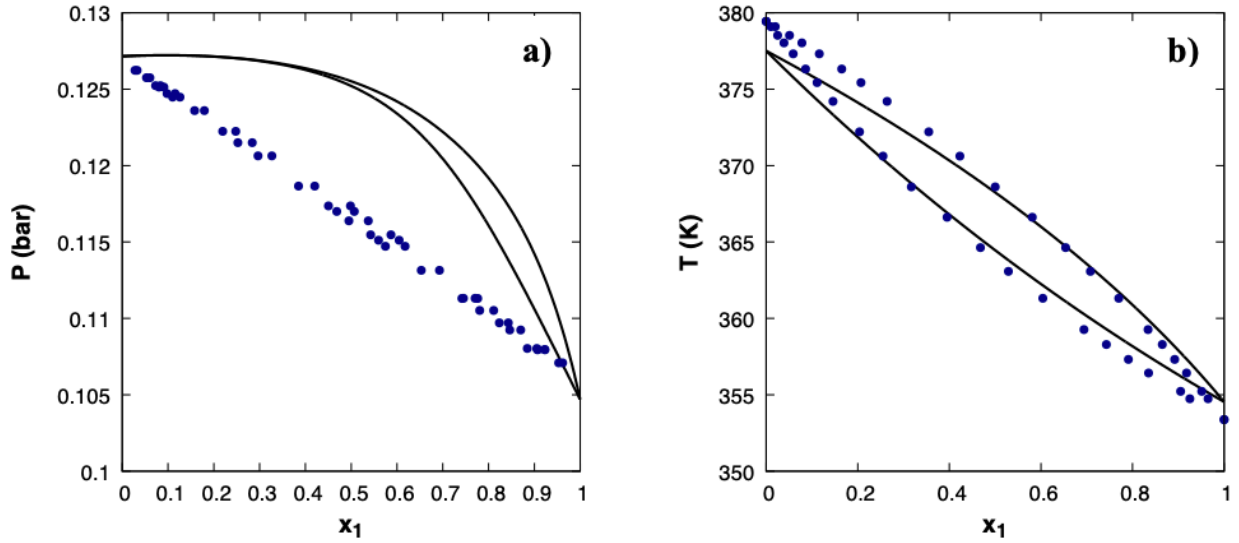

Figure 4.6. Isothermal vapor-liquid equilibria for thiophene (1) (a) + benzene at 298.15 K and (b) toluene (2) at 0.9003 bar. The solid lines represent the GC-SAFT-VR predictions and the symbols the experimental data[211,213].

In Figure 4.6, we consider thiophene with benzene and toluene at a constant temperature and pressure slice, respectively. The mixture of thiophene and toluene in Figure 4.6b shows a reasonable agreement with the experimental data, but the mixtures of thiophene and benzene do not show a good agreement. Both of the pure components on either side of the mole fractions are accurate, but likely a cross interactions for this mixture needs to be introduced due to the polarity of the ring molecule mixed when with a small polar molecule like carbon dioxide. The original plots for these systems had a better agreement but the parameters used were incorrect and the prediction is not valid for comparison here.

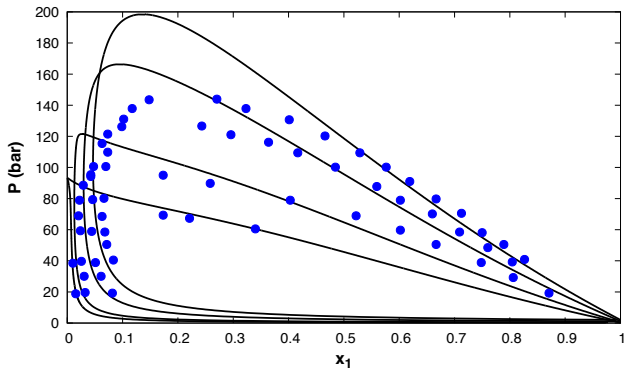

Figure 4.7. Isothermal vapor-liquid equilibria for thiophene (1) + CO_2 at 383 K, 363 K, 334 K, and 314 K (top to bottom). The solid lines represent the GC-SAFT-VR predictions and the symbols represent the experimental data[10,21].

We also consider the mixture of thiophene and carbon dioxide. For this system, we use a cross interaction between carbon dioxide and the -S- functional group. This interaction was fit to the VLE data at 363.15 K. All of the other constant temperature slices considered were then predicted and are shown in Figure 4.7. Similar agreement between the theoretical results and experimental data is obtained as in previous work,[10] including the overprediction of the critical point. Finally, Figure 4.8 shows thiophene mixed with associating alcohol molecules.

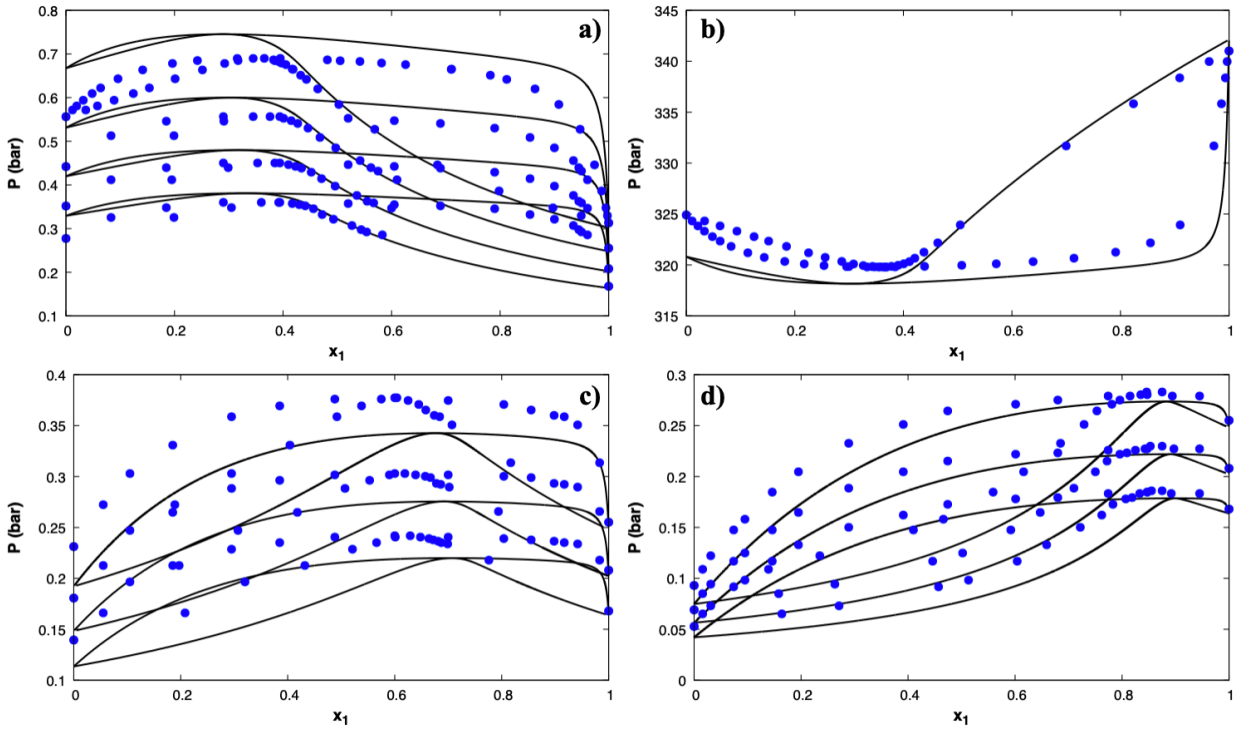

Figure 4.8. Binary mixtures of thiophene (1) + a) methanol (2) at 323.15 K, 318.15 K, 313.15 K, and 308.15 K (top to bottom), b) methanol (2) at 0.6003 bar, c) ethanol (2) at 318.15 K, 313.15 K, 308.15 K (top to bottom), and d) propanol (2) at 318.15 K, 313.15 K, 308.15 K (top to bottom). The solid lines represent the GC-SAFT-VR predictions and the symbols the experimental data[214,215].

The thiophene molecule is non-associating, so no cross-association interactions are considered, only the association within the alcohols. The parameters for the alcohols were taken from previous work[121] but the cross interactions with the sulfur molecules were determined in this work by fitting a binary interaction parameter between carbon dioxide and the -S- functional group. We are able to obtain a good agreement between the experimental data and theoretical predictions, though we do see some deviation on the pure methanol side of Figure 4.8a, likely due to methanol being a small molecule making it difficult to represent with a group contribution approach like GC-SAFT-VR. Again, the theory is able to accurately predict the azeotrope where applicable.

4.4 Conclusions

In this chapter, we have shown that the GC-SAFT-VR functional group parameters can be accurately applied to describe molecules outside the originally intended molecule classes. Functional group parameters are often parameterized to the simplest molecule class that contains that functional group, i.e., CH_3 and CH_2 are fit to alkanes, and then applied to more complex molecules. In this work we were able to apply functional group parameters to FAME molecules without having to change any of their interaction parameters. The ability to freely transfer parameters across molecule types allows for GC-SAFT-VR to accurately predict the parameters of a much broader range of molecules than those that are currently published. The accuracy of the FAME molecule predictions shows one potential instance of this transferability, but this could be broadly expanded upon with further molecules.

Additionally, this chapter expands the available GC-SAFT-VR parameters for accurately representing sulfur molecules, specifically, for the cyclic sulfur molecule thiophene and its mixtures. The ability to accurately predict the properties of sulfur molecules, specifically whether or not an azeotrope is present, is especially important in the separation of sulfur molecules from petroleum to create greener fuel. The parameters for the sulfur molecules considered were able to accurately predict the thermodynamic properties and the presence or absence of an azeotrope for multiple sulfur molecule mixtures with a good agreement. Outside of the cross interaction fit between the sulfur molecules with carbon dioxide, all other mixture information is purely predictive. The advantage of the GC-SAFT-VR approach is the ability to use these parameters transferably for other cyclic or sulfur molecules. Therefore, the mixtures that could be considered can be expanded to sulfur molecules and their mixtures as further systems of interest become desirable in industrial and environmental applications.

Chapter 5

Predicting the Phase Behavior of Fluorinated Organic Molecules and their Mixtures using GC-SAFT-VR

5.1 Introduction

Fluorinated molecules have multiple useful applications, especially in environmental applications due to their unique properties.[36,216,217] Fluorinated molecules are well known for having vastly different properties than their hydrocarbon counterparts, especially in terms of carbon dioxide solubility.[37,38] Specifically, fluorinated molecules can exhibit low surface tensions, high fluidity, low dielectric constants, high vapor pressures, high compressibility, and increased gas solubilities. As their properties differ so widely from other similar molecules, a reliable method to predict their thermodynamic properties and phase behavior is especially important. Moreover, as increasing environmental guidelines are imposed, some fluorinated compounds have the potential to be promising alternatives to current refrigerants with high global warming potential. However, due to the number of possible alternatives, potential toxic effects, and the difficulty in obtaining some of the fluorinated molecules, it is not possible for experimental methods to determine the properties of the all of the possible molecules available to assess their suitability.

Without the wide range of experimental data that many cubic equation of state models require for parameter determination, current theoretical approaches for predicting the properties of fluorinated molecules are limited.[218–221] As such, more molecular based equations of state, that typically have more predictive ability once reliable parameters have been determined, are attractive with which to study these systems.

The statistical associating fluid theory (SAFT) provides has been utilized successfully to predict the properties of fluorinated molecules. Multiple studies have used the SAFT for potentials

of variable range (SAFT-VR) to predict the properties of perfluoroalkanes and their mixtures with alkanes[99,103,222]. In these studies, reasonable agreement between the theoretical and experimental data was achieved, though it was noted that as the alkane chain length increased, the deviations from the experimental data increased. However, the use of a different binary interaction parameter for shorter and longer chain lengths did decrease deviations with experimental data for the longer chains but reduced the predictive power of the model.

Soft-SAFT has also been used to study perfluoroalkane and alkane mixtures[41]. A binary interaction parameter was again required and adjusted for each mixture studied. A modified soft-SAFT method that included quadrupolar interactions[223] provided good agreement with experimental data for mixtures of fluorinated aromatic molecules without the use of a binary interaction parameter; however, saturated fluorinated molecules still required binary interaction parameters.

SAFT studies have also been used to represent hydrofluoroethers (HFEs). However only a small number of HFE molecules have been considered at once, primarily focusing on pure HFEs with small chain alcohols, alkanes, and ketones at atmospheric conditions.[49,98,224] Utilizing perturbed chain SAFT (PC-SAFT)[19,225] good agreement with experimental data was obtained but the work is not easily transferable and required additional binary interaction parameters, limiting their predictive ability.

In this work, multiple classes of fluorinated molecules and their mixtures, including perfluoroalkanes, perfluoroalkylalkanes branched fluorinated alkanes, 1,1-difluoroalkanes, 1-fluoroalkanes, and hydrofluoroethers, are considered. In order to develop a predictive model, group contribution SAFT-VR (or GC-SAFT-VR) is used as it allows molecules to be represented by functional groups that can typically be parameterized based on pure component data alone. GC-

SAFT-VR has been used successfully to study the phase behavior of a wide range of molecules including alkanes, alkenes, ketones, acetates, esters, alcohols, aldehydes, amines, carboxylic acids, aromatics, and polymers.[10,11,22,47,120,121] Therefore, parameters from previous work[10,11,22,47,120,121] have been used herein with new cross interaction parameters for some groups and CO_2 proposed. The parameters for each functional group are fit to experimental vapor pressure and saturated liquid density data for a small set of molecules from a molecule class that contains the functional groups of interest.

5.2 Models & Theory

The GC-SAFT-VR approach[22] represents each functional group in a molecule by tangentially bonded segments that have individual size and energy parameters. The entirety of the GC-SAF-VR model is outlined in Chapter 2, so the expressions are not repeated here.

Parameters for all of the functional groups used in this work were originally introduced by Haley et al.[47], but due to multiple parameters being used incorrectly and inconsistently in the original work, some parameters had to be refit and clarified in this work in order to utilize transferable parameters. GC-SAFT-VR allows the transferable use of parameters that are fit for functional groups to build up other molecules. In the previous work, incorrect and inconsistent parameters were used for multiple molecules. This included utilizing multiple independent parameter sets all for the same functional groups for groups including OCH_2, CF_2, CHF_2, and others. Therefore, for some fluorinated molecules, hydrofluoroethers (HFEs) specifically, the parameters were refit in order to ensure that the parameter set were transferable. Outside of HFEs, the other functional group parameters from the previous work were kept the same. Additionally,

the cross interaction between fluorinated molecules and carbon dioxide is refit because the original one was not specified and therefore could not be replicated.

The pure component properties of various perfluoroalkanes, perfluoroalkylalkanes, branched fluorinated alkanes, 1,1-difluoroalkanes, 1-fluoroalkanes, and hydrofluoroethers have been re-determined. Table 5.1 shows the vapor pressure and saturated liquid density average absolute deviations (AAD) for the molecules considered. A limited set of mixtures including mixtures of perfluoroalkanes with alkanes as well as of perfluoroalkanes and HFEs with carbon dioxide have also been studied.

Table 5.1. Average absolute deviation in vapor pressures and saturated liquid densities obtained between theoretical and experimental data[223,226–230] results for pure fluorinated fluids.

Compounds	T (K)	N_{pt}	%AAD*P*	%AADρ_{liq}
Perfluoroalkanes				
Perfluoropropane	241 – 283	13	6.50	1.48
Perfluorobutane*	155 – 345	20	6.02	3.23
Perfluoropentane*	170 – 370	21	9.61	2.44
Perfluorohexane	185 – 395	43	4.03	2.44
Perfluoroheptane*	225 – 425	41	3.60	1.96
Perfluorooctane*	360 – 445	18	6.95	1.79
Perfluorononane	375 – 445	15	8.36	1.79
Perfluorodecane*	425 – 500	16	5.49	1.61
Average			6.32	2.09
Perfluoroalkyalkanes				
Perfluorobutylpentane*	P: 278 – 328	P: 21	3.80	
	ρ_{liq}: 278 – 353	ρ_{liq}: 16		0.59
Perfluorobutylhexane	P: 278 - 328	P: 21	3.06	
	ρ_{liq}: 278 – 353	ρ_{liq}: 16		0.66
Perfluorobutyloctane	P: 298 – 328	P: 13	2.13	
	ρ_{liq}: 278 - 353	ρ_{liq}: 16		0.68
Perfluorohexylhexane*	P: 288 - 328	P: 17	17.34	
	ρ_{liq}: 278 - 353	ρ_{liq}: 16		0.23
Perfluorohexyloctane	ρ_{liq}: 278 - 353	ρ_{liq}: 16		0.34
Average			6.58	0.50
Branched Fluorinated Alkanes				
2-Fluoro-2-methylbutane*	250 - 340	25	0.80	3.28
2-Fluoropropane	173 – 325	35	4.96	2.48
2-Fluorobutane	253 – 385	32	5.09	1.14
3-Fluorohexane*	280 – 395	24	4.81	0.97
Average			3.91	1.97
1-1,-Difluoroalkanes				
1,1-Difluoropentane*	270 – 375	22	8.34	0.13
1,1-Difluorohexane*	290 – 405	24	4.92	0.07
1,1-Difluoroheptane	293 – 425	27	9.50	0.13
1,1-Difluorooctane	300 – 429	44	10.01	
Average			8.19	0.11
1-Fluoroalkanes				
1-Fluoropentane	250 – 370	32	9.65	0.44
1-Fluorohexane	290 – 425	32	4.57	0.65
1-Fluoroheptane*	290 – 425	32	0.91	0.38
1-Fluorooctane*	290 – 445	38	4.02	0.41
1-Fluorononane	293 – 470	37	6.90	0.51
Average			5.21	0.48

Hydrofluoroethers (HFEs)			
HFE-347pc-f*	297 – 464	19	15.75
HFE-347mcf	298 – 455	16	21.51
HFE-356pc-f*	300 – 501	21	24.69
HFE-374pcf	343 – 505	20	6.12
HFE-449mec-f*	303 – 476	19	16.66
HFE-449mcf-c*	300 – 473	21	25.25
HFE-458pcf-c	323 – 510	19	22.27
HFE-467mccf*	292 – 482	23	24.84
HFE-569mccc	309 – 473	13	29.42
Average			21.29

*Molecule used to determine the model parameters

5.3 Results & Discussion

To describe the molecules of interest, parameters developed by Haley and McCabe [47] to describe the primary functional groups in fluorinated molecules are used. First, properties for the pure molecules were compared to experimental data. The pure fluorinated molecule classes considered are perfluoroalkanes, perfluoroalkylalkanes, branched fluorinated alkanes, 1,1-difluoroalkanes, 1-fluoroalkanes, and hydrofluoroethers. Since the initial publication of the fluorinated molecules, additional experimental data has become available. Therefore, the average absolute deviations (AADs) to experimental vapor pressures and saturated liquid densities are recomputed to include the new data. In order to represent these molecules, molecular parameters were fit to a small subset from each molecule class. These molecular parameters can be found in Tables 5.2 – 5.4. These tables include parameters for both CF_2 and $CF_2\alpha$. Haley et al.[47] found that due to high electronegativity differences, a different set of binary interaction parameters were required when describing a CF_2 functional group directly next to a CH_2 functional group. These interactions are represented by the $CF_2\alpha$ functional group.

Table 5.2. GC-SAFT-VR parameters for the segment size, σ, and segment number, m, of each functional group studied.

Functional Group	σ (Å)	m_i
CF_3	4.618	0.685
$CF_2\alpha$	4.345	0.370
CF_2	4.345	0.370
CF	3.251	0.269
CHF_2	3.076	1.577
CH_2F	3.338	1.046
CHF	3.962	0.548

Table 5.3. GC-SAFT-VR segment-segment dispersion energy range parameters $\lambda_{ki,lj}$.

	CF_3	$CF_2\alpha$	CF_2	CF	CHF_2	CH_2F	CHF
CH_3	1.397	1.572	1.572	1.644	1.422	1.463	1.421
CH_2	1.482	1.819	1.660	1.734	1.524	1.560	1.512
CH	1.608	1.786	1.786	1.888	1.678	1.709	1.649
CH_2=CH	1.429	1.303	1.303	1.687	1.461	1.501	1.455
OCH_3 (ether)	1.423	1.611	1.611	1.695	1.455	1.498	1.450
OCH_2 (ether)	1.550	1.679	1.679	1.755	1.677	1.556	1.502
OCH (ether)	1.628	1.847	1.847	1.990	1.723	1.760	1.680
CO_2	1.398	1.596	1.596	1.684	1.426	1.474	1.425
CF_3	1.321	1.476	1.476	1.526	1.327	1.367	1.336
$CF_2\alpha$	1.476	1.641	1.641	1.717	1.515	1.549	1.504
CF_2	1.476	1.641	1.641	1.717	1.515	1.549	1.504
CF	1.526	1.717	1.717	1.818	1.584	1.621	1.563
CHF_2	1.327	1.515	1.515	1.584	1.336	1.385	1.346
CH_2F	1.367	1.549	1.549	1.621	1.385	1.430	1.389
CHF	1.336	1.504	1.504	1.563	1.346	1.389	1.354

Table 5.4. GC-SAFT-VR segment-segment dispersion energy well depth parameters $\varepsilon_{ki,lj}/k_B$ (K).

	CF_3	$CF_2\alpha$	CF_2	CF	CHF_2	CH_2F	CHF
CH_3	271.88	226.43	226.43	260.40	258.13	253.13	328.97
CH_2	273.61	227.87	172.48	262.05	259.77	255.43	331.05
CH	177.65	147.95	147.95	170.15	168.67	165.85	214.95
CH_2=CH	263.09	166.52	166.52	251.97	249.78	245.61	318.33
OCH_3 (ether)	269.63	224.55	224.55	258.24	255.99	251.72	326.24
OCH_2 (ether)	238.51	198.63	198.63	228.43	181.15	222.66	288.58
OCH (ether)	146.80	122.26	122.26	140.60	139.38	137.05	177.63
CO_2	237.88	198.11	162.45	227.83	225.85	222.08	287.82
CF_3	315.56	262.81	262.81	302.23	299.60	194.60	381.81
$CF_2\alpha$	262.81	218.87	218.87	251.70	249.51	245.35	317.98
CF_2	262.81	218.87	218.87	251.70	249.51	245.35	317.98
CF	302.23	251.70	251.70	289.46	286.94	282.15	365.68
CHF_2	299.60	249.51	249.51	286.94	284.45	279.70	362.51
CH_2F	294.60	245.35	245.35	282.15	279.70	275.03	356.45
CHF	381.81	317.98	317.98	365.68	362.51	356.45	461.98

A summary of the AAD calculations is included in Table 5.1. Within each molecule class the individual molecules that were used to model the parameters in the original work are denoted with an *. Between 2 - 4 molecules from each molecule class were used to fit the parameters for the necessary functional groups. Comparing the AAD values from the original publication[47] to the work here, the values are comparable for each of the molecule classes, with minimal deviations from the initially published AAD values, outside of the HFEs. Slight deviations are expected when comparing to new sets of experimental data as each set of experimental data also deviates slightly from others at the same conditions.

In contrast, to the other molecule classes, the HFEs showed considerable deviations from the initial work. After recalculating the AAD values for the HFEs, the deviations from the initial publication were significant, despite using the same experimental dataset. Therefore, the HFE groups required a refit in order to accurately represent the HFE molecules utilizing transferable parameters. The HFE molecules that were used to fit the transferable parameters were reconsidered as the AAD values were much higher than initially published when fitting to the same molecules. Therefore, rather than fit to only 4 HFEs, the parameters were fit to 5 HFEs to assist in the accuracy of the model. Unfortunately, even with the refit, the AAD values for the HFE molecules remained considerably above reasonable values. Therefore, the HFE molecules are expanded upon in future chapters in order to more accurately represent them using GC-SAFT-VR. The fits obtained in this chapter were used in both this work and in Chapter 6 before they were redone in Chapter 7. The updated parameters that were used for HFEs are included in Tables 5.2 - 5.4.

After adjusting the parameters for the fluorinated molecules, some of the mixtures from the original work were reconsidered with the updated parameters to assure that only transferable parameters are considered. The first mixtures considered, shown in Figure 5.1, were

perfluoroalkanes with alkanes at constant temperature slices, specifically mixtures of perfluorohexane with pentane, heptane, and octane at temperatures of 293.65 K, 317.65 K, and 313.15 K, respectively. The agreement in Figure 5.1a between the predicted and experimental compositions is reasonable and comparable to the original published work. The predicted and experimental composition curves in Figure 5.1b of hexane with perfluoropentane, perfluorohexane, perfluoroheptane, and perfluorooctane at 293.15 K, 298.15 K, 303.15 K, and 313.15 K, respectively show good agreement and are comparable to the initial work.

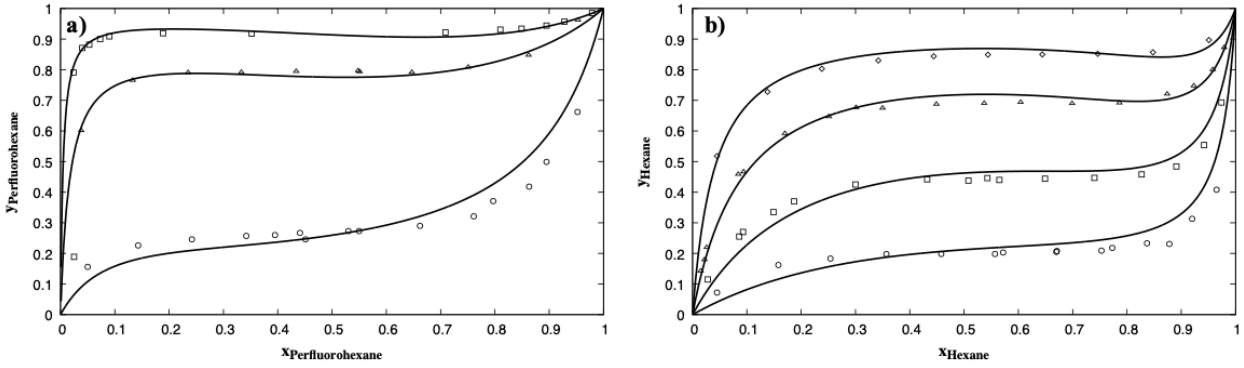

Figure 5.1. Predicted composition curves for a.) perfluorohexane + pentane at 293.65 K (circles), + heptane at 317.65 K (triangles) and + octane at 313.15 K (squares), and b.) hexane + perfluoropentane at 293.15 K (circles), + perfluorohexane at 298.15 K (squares), + perfluoroheptane at 303.15 K (triangles) and + perfluorooctane at 313.15 K (diamonds). Solid lines represent GC-SAFT-VR predictions and the data points represent experimental data[231].

Data for a binary mixture of perfluorobutane and butane are shown in both Figure 5.2 and Figure 5.3a. As seen in both of these cases, the agreement with experimental data is poor. While the trends are similar, the actual values are slightly higher for the *pT* projection as shown in Figure 5.2.

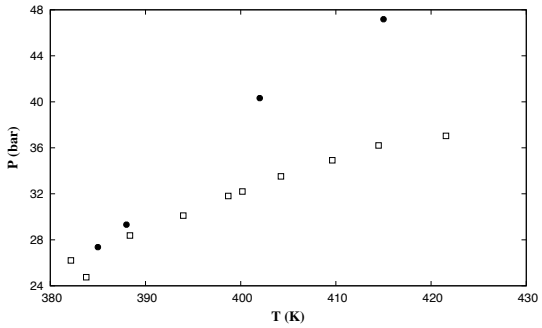

Figure 5.2 Predicted *pT* projection of the critical line for the butane (1) + perfluorobutane (2) binary mixture. Black circles represent predictions from the GC-SAFT-VR approach and open squares show results from the SAFT-VR[222] equation.

At low temperatures, the agreement is reasonable, but at higher temperatures, the pressure values that GC-SAFT-VR predicts are much higher. Additionally, in Figure 5.3a at lower temperatures, the theory predicts lower pressures than the experimental data shows. Though at the lower temperatures, the difference is less significant as the order of magnitude is smaller. There are a few reasons as to why the agreement between the theory and experimental data for the mixture of perfluorobutane and butane is not as reasonable as it is with other mixtures. One reason may be that both perfluorobutane and butane are smaller molecules in their molecule classes. Typically, SAFT parameters aren't fit to the smallest or largest molecules in a molecule class as they will dominate the parameters and not allow for accurate representation for the bulk of the molecules in each molecule class. Consequently, this can cause the smallest and largest molecules in each class to not be as well-represented, causing perfluorobutane and butane to have higher deviations than other molecules in the class. Conversely, the mixture of perfluorobutane and butene in Figure 5.3b shows a much better agreement with the experimental data, especially at the lower two temperatures. It is worth noting that at the temperature range considered in Figure 5.3b for perfluorobutane and butene, is within a range where the perfluorobutane and butane mixture matches the experimental data quite well in Figure 5.2. This shows that perfluorobutane mixtures

are able to be accurately represented between about 300 K to 395 K, but outside this range, we see some deviation from the experimental data.

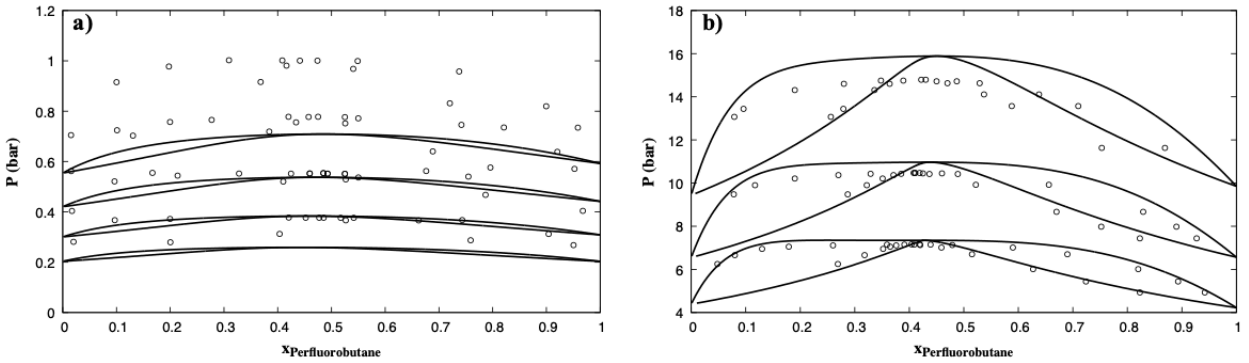

Figure 5.3. a.) *P-x-y* diagram) of perfluorobutane + butane binary mixtures at 259.95 K, 253.62 K, 246.35 K, and 238.45 K (top to bottom. b.) P-x-y diagram of perfluorobutane + butene binary mixtures at 342.93 K, 327.93 K, and 312.92 K (top to bottom). Solid lines represent results from the GC-SAFT-VR approach while the experimental data points[232,233] are represented by open circles.

Next, another perfluoroalkane and alkane binary mixture is considered. Namely in Figure 5.4, a mixture of perfluorohexane and pentane is considered at a constant temperature slice of 293.65 K. This comparison to experimental data is quite reasonable, despite the slight overprediction of the pressure near the azeotrope. The agreement between theory and experimental data was improved over the work of Dias et al.[234].

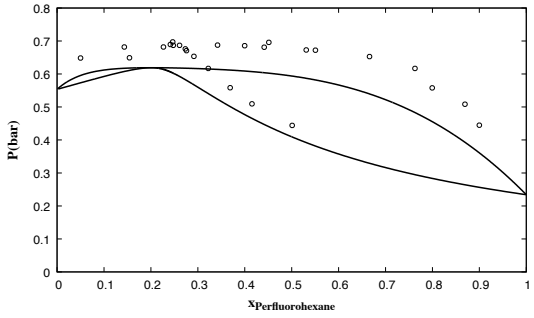

Figure 5.4. *Pxy* prediction of perfluorohexane + pentane mixture at 293.65 K. The lines correspond to the GC-SAFT-VR predictions and the symbols the experimental data[231].

Liquid-liquid equilibrium is then predicted for binary mixtures of perfluorooctane with hexane, heptane, octane, and nonane in Figure 5.5a and perfluorohexane with hexane in Figure 5.5b at atmospheric pressure. These results do overpredict the upper critical solution temperature, but this overprediction is consistent with the previous work of Dias et al.[234]. Colina et al.[48] was able to correct this overprediction by rescaling the model to the critical point, but in order to maintain a fully predictive model, we don't consider that here.

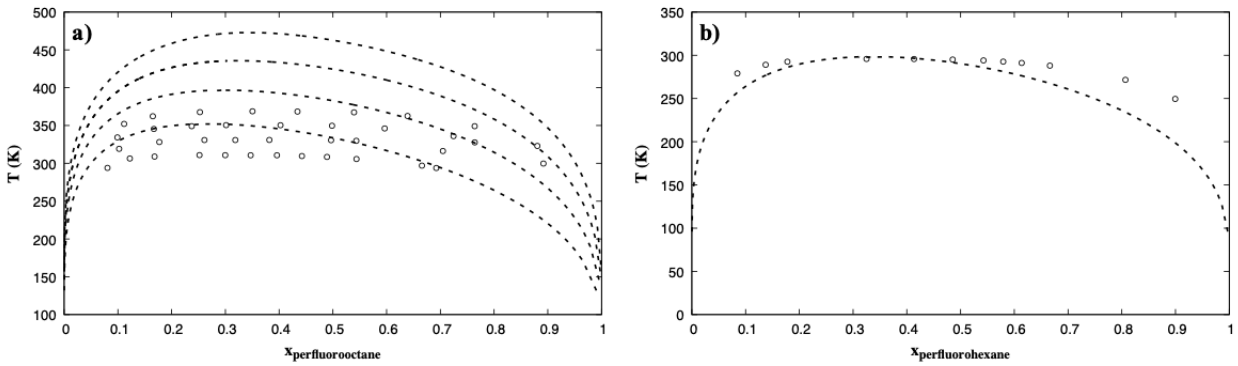

Figure 5.5. a.) LLE diagram at a constant pressure of 1.013 bar for binary mixtures of perfluorooctane + alkanes, hexane, heptane, octane, and nonane (from bottom to top). Solid lines represent predictions from the GC-SAFT-VR approach and open circles represent the experimental data points[235], b.) LLE diagram at a constant pressure of 1.013 bar for the binary mixture of perfluorohexane + hexane. The solid line represents the theoretical prediction and the open circles represent the experimental data[236].

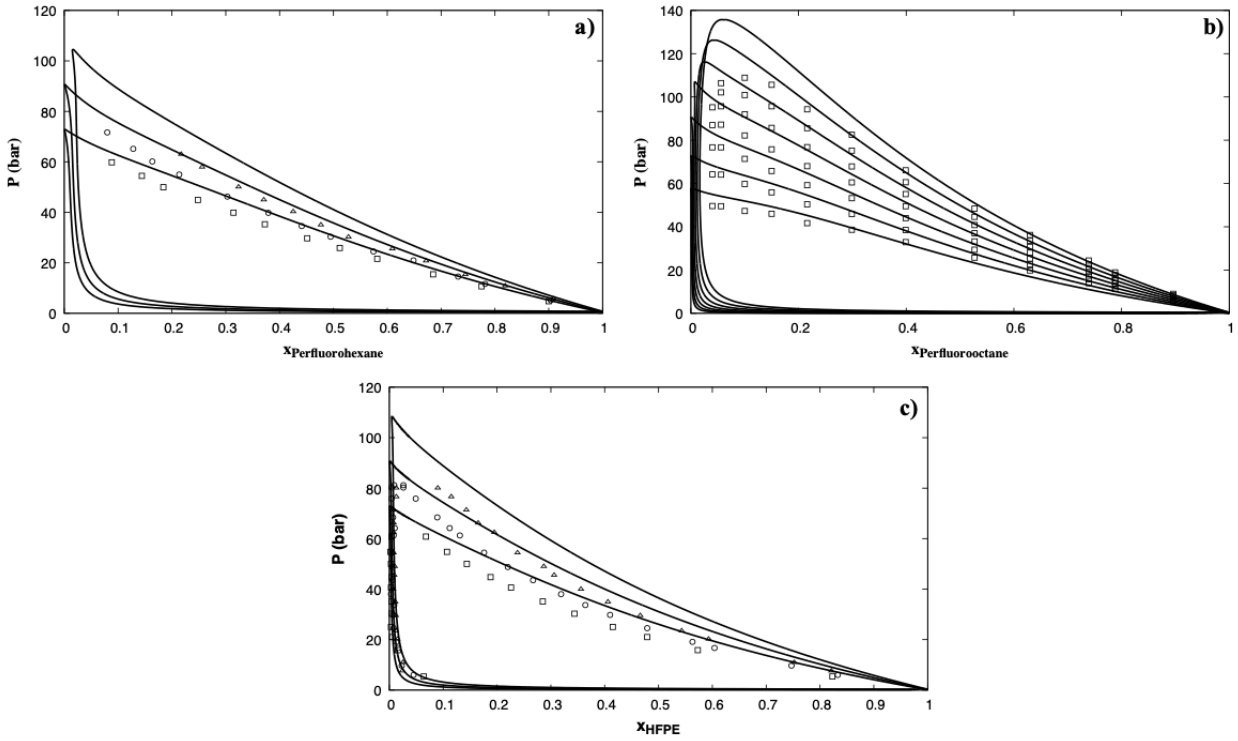

Figure 5.6. Constant temperature slices of CO_2 + a) perfluorohexane binary mixture at 303.15 K (squares), 313.15 K (circles), and 323.15 K (triangles), b) perfluorooctane at 293.15 K, 303.15 K, 313.15 K, 323.15 K, 333.15 K, 343.15 K, and 353.15 K (bottom to top), and c) $C_5H_3F_9O$ at 303.15 K (squares), 313.15 K (circles), and 323.15 K (triangles). Solid lines represent the GC-SAFT-VR predictions and the symbols represent the experimental data.[41,42,45]

Finally, we consider mixtures of fluorinated molecules with carbon dioxide in Figure 5.6. The SAFT-VR CO_2 parameters were taken from the literature[237] and are provided in Tables 5.1-5.3. Using the CO_2, CF_3, and CF_2 parameters, the GC-SAFT-VR approach was then used to determine the phase behavior of the CO_2 + perfluorohexane and CO_2 + perfluorooctane mixtures. Fig. 6a and b show *Pxy* slices of the CO_2 + perfluorohexane and CO_2 + perfluorooctane phase diagrams, respectively. In addition, *Pxy* slices of the CO_2 + 1,1,2,3,3,3-hexafluoropropyl (2,2,2-trifluoroethyl) ether binary mixture was predicted as shown in Fig. 5.6c. In all cases excellent predictions are obtained with the use of a single fitted cross interaction between the CO_2 molecule and CF_2 groups. The CO_2 + 1-ethoxy-1,1,2,2,3,3,4,4,4-nonafluorobutane binary mixture at 303.15K was used to determine the cross interaction, with all systems in Figure 5.6 then predicted:

note the use of a binary mixture to fit the cross interaction is unavoidable since the CO_2 molecule cannot be treated within the group contribution approach. Each of these figures show a reasonable agreement with the experimental data. The shape of the constant temperature slices for Figures 5.6a and c could be closer to the experimental data, which is why they are considered more extensively in future chapters. The trends in the prediction for perfluorooctane and carbon dioxide in Figure 5.6b are closer to the experimental data, but there is still an overprediction of the critical regions, which is typical with SAFT methods.

5.4 Conclusions

After clarifying and adjusting the GC-SAFT-VR parameters for fluorinated molecules, we ensured that only transferable parameters were used to represent these molecules. Utilizing corrected transferable parameters, we were able to obtain similar AAD values to those that were originally published for each group of fluorinated molecules except hydrofluoroethers (HFEs). Despite the increased AAD values for HFEs, the mixture of HFE and carbon dioxide still gives reasonable results. In order to get more reasonable AAD results for HFEs, they are reconsidered in future chapters as well.

All of the other binary mixtures considered show similar or improved agreement with the experimental data compared to the original work, except for the mixture of perfluorobutane and butane. However, the mixture of perfluorobutane and butane is reasonable within a set temperature range. Due to the complex nature of fluorinated molecules, the GC-SAFT-VR parameter set is expanded upon in future chapters in order to best represent these complex molecules, but in this work the parameters used are able to reasonably represent both pure fluorinated fluids as well as binary mixtures of fluorinated molecules with alkanes and carbon dioxide.

Chapter 6

Vapor-Liquid Equilibria for Binary Systems Carbon Dioxide + 1,1,1,2,3,3-hexafluoro-3-(2,2,2-trifluoroethoxy)propane or 1-ethoxy-1,1,2,2,3,3,4,4,4-nonafluorobutane at 303.15 – 323.15 K

This chapter was taken from the published work of H. Matsuda et al.[45]

6.1 Introduction

Chlorofluorocarbons (CFCs) have been utilized extensively as refrigerants, blowing agents, and cleaning solvents due to their chemical stability and physical properties. However, the Montreal Protocol (1989) requested that the use of CFCs be phased-out prior to 1996 because of ozone layer depletion and global warming. Thus, CFC alternatives have been investigated heavily in subsequent years. Hydrochlorofluorocarbons (HCFCs) have been used as interim replacements for CFCs because of similar physicochemical properties and lower ozone depletion potential (ODP) values; however, it should be noted that they have higher global warming potential (GWP) values. Thus, they were to be phased-out by 2020 according to the updated Montreal Protocol. Hydrofluorocarbons (HFCs) and perfluorocarbons (PFCs) have been used as alternatives to CFCs and HCFCs, because they have zero ODP and high thermal stabilities; however, they still have high GWP values. Therefore, HFCs and PFCs were included in the set of six major greenhouse gases whose use should be reduced in the Kyoto Protocol (2005). As a result, hydrofluoroethers (HFEs) have been utilized as third generation alternatives to replace CFCs, HCFCs, HFCs, and PFCs due to their zero ODP, low GWP, and short atmospheric lifetimes[39,40,47,230,238]. Industrially HFEs are also used as cleaning solvents in electronic and magnetic devices, as a protective gas in the melting of alloys, for decontamination of fluids, and as heat transfer fluids in heat exchangers[239,240]. However, pure HFE's are flammable and toxic. Thus, a mixture of HFE's with

another refrigerant could retain desirable properties, whilst negating some of the more undesirable ones, and has been a successful strategy in the past (e.g., hydrofluoroolefins[241,242]).

Carbon dioxide (CO_2) is a well-known natural refrigerant that can be used as an alternative to the above-mentioned CFCs, HCFCs, HFCs, and PFCs, making it a possible refrigerant to use in mixtures with HFEs. CO_2 is a natural, nontoxic, readily available and inflammable gas with zero ODP. Because of these favorable physical properties, CO_2 has already been used as a working fluid for heat pumps[243]. However, one of the main disadvantages is that CO_2 run heat pumps need to be operated in a trans-critical cycle, i.e., at a very high pressure (typically within 15 MPa of the maximum operating pressure), due to its relatively low critical constants (T_c = 304.12 K, P_c = 7.374 MPa[244])[245,246]. Mixtures of CO_2 and HFEs may thus also provide a promising alternative by reducing the need for a high operating pressure whilst retaining the more favorable properties of CO_2.

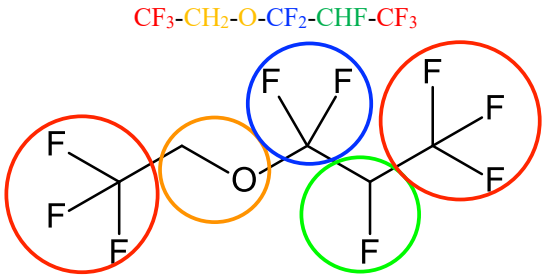

HFE-449mec-f

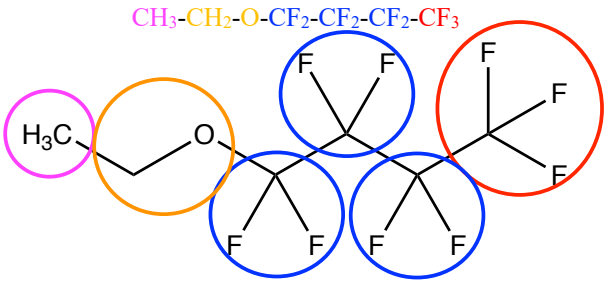

HFE-7200

Figure 6.1. Structures of HFE-449mec-f and HFE-7200.

In order to evaluate the performance of mixtures of CO_2 and HFEs and determine optimal operating conditions for refrigeration processes using mixtures of CO_2 and HFEs, an understanding of the mixture vapor-liquid equilibrium (VLE) data is crucial. Several studies report experimental VLE data for binary mixtures of CO_2 + CFCs[41,42,246–253]. However, limited VLE data is available in the literature regarding binary systems CO_2 + HFEs. The object of this work is thus to measure the VLE data for binary systems CO_2 + HFEs, i.e., 1,1,1,2,3,3-hexafluoro-3-(2,2,2-trifluoroethoxy)propane (HFE-449mec-f) and 1-ethoxy-1,1,2,2,3,3,4,4,4-nonafluorobutane (HFE-7200). The structures of the two HFEs studied are shown in Figure 5.1. These two HFEs were chosen because HFE-449mec-f can also be used as an alternative cleaning solvent[40,253,254] and HFE-7200 has lower values of GWP and atmospheric lifetime compared to other HFEs (60 and 0.77 years, respectively[39]). It can be used not only as a working fluid for refrigerants and heat transfer, but also as a cleaning solvent and lubricant carrier, etc.[240,255]. We determined the isothermal VLE for CO_2 + HFE-449mec-f or HFE-7200 at temperatures 303.15, 313.15, and 323.15 K using a static-circulation apparatus. The experimental VLE data were correlated by the Peng-Robinson (PR) equation of state (EOS)[256] coupled with the van der Waals one fluid (vdW1) mixing rule and Wong-Sandler (WS)[257] mixing rules combined with the non-random two-liquid (NRTL) model[258]. The systematic series of experimental data are also described with the group contribution (GC) based SAFT-VR[22] equation of state (GC-SAFT-VR) that combines the SAFT-VR[99] equation with a group contribution[22] approach. The GC-SAFT-VR equation describes chains composed of neutral non-polar square-well spheres of different sizes and/or interaction energies (including dispersion and association), with monomer properties computed from perturbation theory using a reference system of hard spheres of arbitrary composition and size. Using this hetero-segmented approach, GC-SAFT-VR parameters have been determined in prior work for a

wide range of functional groups (i.e., CH_3, CH_2, C=O, CH_2O, OH, etc.) and used to study the thermodynamics and phase behavior of alkanes, alkenes, ketones, aromatics, acetates, esters, polymers, and other associating and non-associating fluids (see for example[22,47,120,121,259]). We note that the cross interactions between simple groups such as CH_3-CH_2 are given by the simple Lorentz-Berthelot combining rules; however, for cross interactions with polar groups, such as the carbonyl group, where deviations from "ideal behavior" are expected, the cross interactions are fitted to pure component experimental data for molecules that contain the functional groups under consideration. In this way, in contrast to the traditional equation of state and SAFT-based approaches, when deviations from the Lorentz-Berthelot combining rule are seen, parameters do not need to be fit to experimental mixture data. Additionally, by not averaging the group parameters on chain formation, as in other group-contribution based SAFT approaches[115,117,260], the connectivity of functional groups and location of association sites can be specified in the GC-SAFT-VR approach.

Multiple SAFT approaches have been proven effective in the study of a wide variety of refrigerants, including fluorinated systems, such as the SAFT-VR study by Galindo et al.[104] and the work of Avendaño et al.[261] who studied pure refrigerants with the SAFT-gamma group-contribution approach. Additionally, fluorinated refrigerant mixtures have also been studied using GC-SAFT-VR and PC-SAFT in work by Haley et al.[47] and Fouad and Vega[242], respectively. In this work, we expand upon previous work with the GC-SAFT-VR approach in order to predict the phase behavior of the CO_2 + HFE binary mixtures studied and provide a wider examination of their phase behavior than is possible with correlative approaches.

6.2 Experimental Methods

6.2.1 Materials

The chemicals used in this work are summarized in Table 5.1. The CO_2 was passed through a $0.5\mu m$ inline filter (Nepro Company, Japan) before use to avoid undesirable particles. The purity of the HFE-449mec-f and HFE-7200 was verified by gas chromatography (GC) (GC-14A, Shimadzu Co. Ltd., Kyoto, Japan) with a thermal conductivity detector. Existence of two isomers has been reported in the literature[240,262–265]. Thus, the composition of binary isomers of HFE-7200 was determined by ^{1}H NMR analysis (JNM-ECX400, JEOL Ltd., Tokyo, Japan). The obtained mole fraction of the isomer with CAS number 163702-06-5 was 0.614, whereas that of the isomer with CAS 163702-05-4 was 0.386. The densities (ρ) of the esters at 298.15 K was measured using a precision digital oscillating U-tube densimeter (DMA 4500, Anton Paar GmbH, Graz, Austria) with a reproducibility of 10^{-2} kg m^{-3}. The experimental ρ at 298.15 K for the chemicals used in this work are reported in Table 5.1 together with the literature values[240,266].

Table 6.1. Chemicals used in this work.

Component	Source	CAS Registry Number	Purification method	Purity	ρ (298.15 K) (kg m^{-3})	
					Experimental [f]	Literature
CO_2	Showa Denko Gas Products Co. Ltd.	124-38-9	No	0.9999 [d]	-	-
HFE-449mec-f [a]	DAIKIN Fine Chemical Co. Ltd.	993-95-3	Molecular sieves 13X	0.995 [e]	1527.97	1531.2 [g]
HFE-7200 [b]	3M Co. Ltd.	163702-06-5 [c] 163702-05-4 [c]	Molecular sieves 5A	0.999 [e]	1422.56	1422.65 [h]

[a] IUPAC name: 1,1,1,2,3,3-hexafluoro-3-(2,2,2-trifluoroethoxy)propane.
[b] IUPAC name: 1-ethoxy-1,1,2,2,3,3,4,4,4-nonafluorobutane.
[c] Binary mixture of two isomers with mole fraction of 0.614 for CAS number 163702-06-5 and 0.386 for CAS 163702-05-4, determined by ^{1}H NMR, with a standard uncertainty $u(x) = 0.01$.
[d] volume fraction.
[e] mass fraction.
[f] At $P = 101$ kPa. Standard uncertainties are $u(\rho) = 0.01$ kg·m^{-3}, $u(T) = 0.01$ K, and $u(P) = 1$ kPa.
[g] Tochigi et al.[266]. At $T = 293.15$ K.
[h] Rausch et al.[240].

6.2.2 Apparatus and Procedure

We used a static-circulation apparatus to measure the VLE. A schematic diagram of the apparatus is shown in Figure 5.2. It is composed of three parts, i.e., a variable volume equilibrium cell, sampling unit for vapor and liquid phases, and GC. The equilibrium cell 1 was immersed in a thermostated water bath with three windows (THOMAS KAGAKU Co. Ltd., Japan). There are six visual sapphire windows (23 mm in diameter and 11.5 mm thick) in the equilibrium cell for the visual observation of the phase behavior.

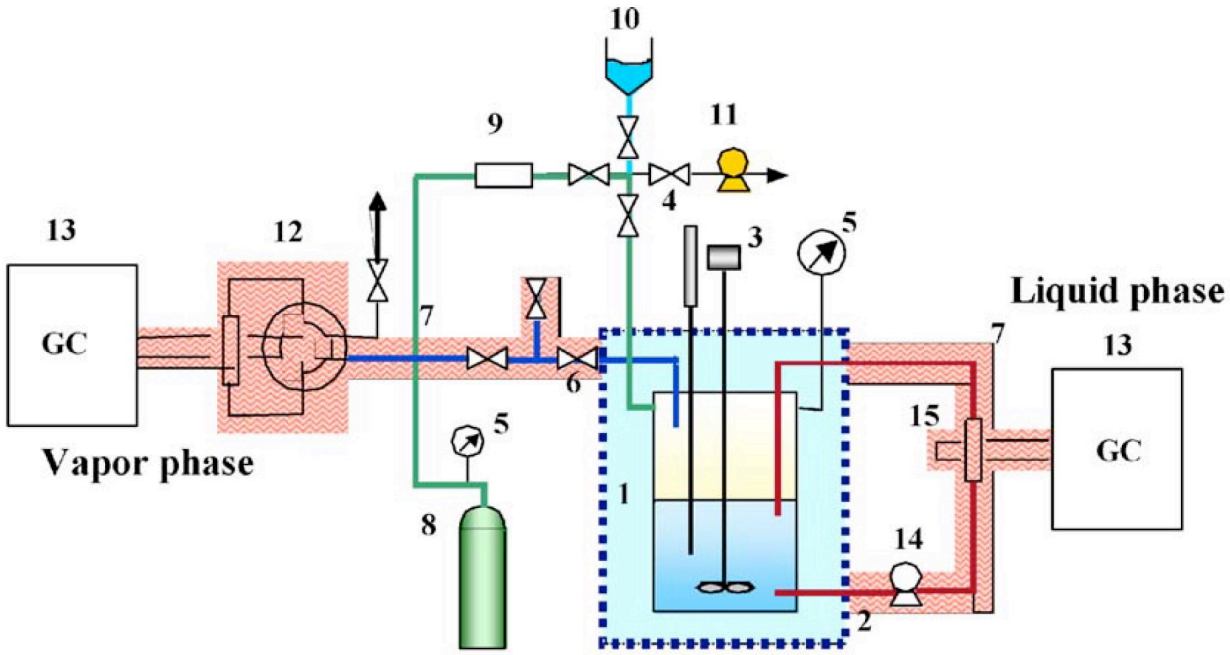

Figure 6.2. Schematic diagram of the experimental apparatus for measuring isothermal VLE. 1, equilibrium cell; 2, water bath; 3, stirrer; 4, thermometer; 5, pressure indicator; 6, sampling valve; 7, ribbon heater; 8, CO_2 cylinder; 9, in-line filter; 10, sample installation; 11, vacuum pump; 12, six-way valve; 13, gas chromatograph; 14, circulation pump; and 15, sample injector.

The temperature of the apparatus was controlled within ± 0.1 K. The equilibrium cell was made from stainless steel (SUS 316) and measurements can be made at temperatures up to 473 K and pressures up to 20 MPa. The inner volume was 500 cm^3. A calibrated Pt 100 Ω platinum resistance thermometer 4 with an accuracy of ± 0.01 K was used for measurements of the sample temperature. The pressure was determined by a pressure indicator (DPI 145, Druck Co.,

Kirchentellinsfurt, Germany) with an accuracy of ± 0.04 % F.S. Two GCs were used for the analysis of the vapor and liquid phase samples, respectively. Further details regarding the experimental apparatus and procedure have been described in previous work[42].

During measurement, first, the equilibrium cell (labelled 1 in Figure 5.2) was evacuated by the vacuum pump, and HFE-449mec-f or HFE-7200 was charged into the equilibrium cell. Next, CO_2 was added until the desired pressure is achieved. Then, the liquid phase was continuously recirculated (through circulation 14 in Figure 5.2). The interface of the vapor and liquid phases were observed during the measurements by the visual glass windows equipped in the cell. The system was regarded as reaching equilibrium when temperature and pressure fluctuations of no more than ±0.01 K and ±0.001 MPa, respectively, were observed for 30 min. The equilibrium measurement of temperature and pressure before sampling was up to about 6 hours.

Once equilibrium was reached, the vapor and liquid samples were taken (Sample injector 15 in Figure 5.2). Finally, the compositions of the vapor and liquid phases were determined by GC.

6.2.3 Analysis

The vapor and liquid phase samples were analyzed by a GC (GC-14A, Shimadzu Co., Ltd., Kyoto, Japan) with a thermal conductivity detector (TCD). Porapak Q (2.0 m × 3.0 mm inside diameter, Shinwa Chemical Industries Ltd., Kyoto, Japan) was used as the column packing. Helium was used as the carrier gas at a flow rate of 50.0 mL min^{-1}. The temperature in the TCD was maintained at 623 K. Compositions were determined using the absolute area method with a calibration curve. The accuracy for the mole fraction was ± 0.002.

6.3 Models & Theory

6.3.1 Peng-Robinson Equation of State

The correlations of the experimental VLE data were performed with the PR EOS combined with the vdW1 or WS-NRTL models as the mixing rule. The PR EOS is given by,

$$P = \frac{RT}{v-b} - \frac{a(T)}{v(v+b)+b(v-b)} \tag{5.1}$$

where P is the pressure, R is the ideal gas constant, T is the temperature, v is the molar volume, a is the energy parameter and b is the size parameter. These parameters for pure components i, were calculated using

$$a_{ii}(T) = \frac{0.45724R^2T_{c,i}^2}{P_{c,i}}\left[1 + m_i\left(1 - \sqrt{\frac{T}{T_{c,i}}}\right)\right] \tag{5.2}$$

$$m_i = 0.37464 + 1.5422\omega_i - 0.26992\omega_i^2 \tag{5.3}$$

and

$$b_i = \frac{0.07780RT_{c,i}}{P_{c,i}} \tag{5.4}$$

where $T_{c,i}$ and $P_{c,i}$ are the critical temperature and critical pressure for pure component, respectively, and ω_i is the acentric factor. The pure component parameters $T_{c,i}$, $P_{c,i}$ and ω_i[244,266,267] used to calculate the a and b values for the pure components CO_2, HFE-449mec-f, or HFE-7200 are provided in Table 5.2. The acentric factor, ω_i, for HFE-449mec-f and HFE-7200 was estimated from pressure-temperature data.

Table 6.2. Critical temperature, T_c, critical pressure, P_c, acentric factor, ω, and Antoine constants, A, B, C values for the pure components.

Component	T_c (K)	P_c (MPa)	ω	Antoine A [a]	Antoine B [a]	Antoine C [a]
CO_2	304.12 [b]	7.374 [b]	0.225 [b]			
HFE-449mec-f	475.74 [c]	2.233 [c]	0.529 [d]	6.08992 [e]	1126.735 [e]	-69.161 [e]
HFE-7200	483.00 [f]	2.007 [f]	0.464 [d]	6.19053 [f]	1243.910 [f]	-52.285 [f]

[a] $\log\left(P_i^s/\mathrm{kPa}\right) = A - B/[(T/\mathrm{K}) + C]$.
[b] Poling et al.[244].
[c] Yasumoto et al.[230].
[d] Estimated by the definition of acentric factor: $\omega = -\log(P_r^s)_{T_r=0.7} - 1$, which P_r^s is P_i^s/P_c.
[e] Tochigi et al.[266].
[f] Dortmund Data Bank 2019[267].

The vdW1 and WS mixing rules were used to calculate the mixture energy parameter, a, and the size parameter, b. The vdW1 mixing rule is given by,

$$a = \sum_{i=1}^{\mathrm{NC}} \sum_{j=1}^{\mathrm{NC}} x_i x_j \left(a_{ii} a_{jj}\right)^{0.5} \left(1 - k_{ij}\right) \quad \left(k_{ij} = k_{ji},\ k_{ii} = k_{jj} = 0\right) \tag{5.5}$$

and

$$b = \sum_{i=1}^{\mathrm{NC}} x_i x_j \left(\frac{b_i + b_j}{2}\right)\left(1 - l_{ij}\right) \quad \left(l_{ij} = l_{ji},\ l_{ii} = l_{jj} = 0\right) \tag{5.6}$$

where k_{ij} and l_{ij} are binary interaction parameters. The WS mixing rule for the PR EOS is given by,

$$\frac{a}{b} = \sum_{i=1}^{\mathrm{NC}} x_i \frac{a_{ii}}{b_i} + \frac{A_{\infty}^{\mathrm{E}}}{C} \tag{5.7}$$

$$b = \frac{\sum_{i=1}^{\mathrm{NC}} \sum_{j=1}^{\mathrm{NC}} x_i x_j \left(b - \frac{a}{RT}\right)_{ij}}{1 - \sum_{i=1}^{\mathrm{NC}} x_i \frac{a_{ii}}{bRT} - \frac{A_{\infty}^{\mathrm{E}}}{CRT}} \tag{5.8}$$

$$\left(b - \frac{a}{RT}\right)_{ij} = \frac{1}{2}\left[\left(b_i - \frac{a_{ii}}{RT}\right) + \left(b_j - \frac{a_{jj}}{RT}\right)\right]\left(1 - k_{ij}\right) \ \left(k_{ij} = k_{ji},\ k_{ii} = k_{jj} = 0\right) \tag{5.9}$$

with the constant C in Eq. (5.8) as

$$C = \frac{\ln\left(\sqrt{2} - 1\right)}{\sqrt{2}} \tag{5.10}$$

where A_{∞}^{E} is the excess Helmholtz free energy at infinite pressure, and k_{ij} is the second virial coefficient binary interaction parameter. The NRTL model[258] was applied to calculate A_{∞}^{E} given by,

$$A_{\infty}^{E} = \sum_{i=1}^{NC} x_i \frac{\sum_{j=1}^{NC} x_j \tau_{ji} G_{ji}}{\sum_{k=1}^{NC} x_k G_{ki}} \tag{5.11}$$

$$G_{ij} = \exp(-\alpha_{ij}\tau_{ij}) \quad (\alpha_{ij} = \alpha_{ji},\ \alpha_{ii} = \alpha_{jj} = 0) \tag{5.12}$$

$$\tau_{ij} = \frac{g_{ij} - g_{jj}}{RT} \quad (\tau_{ii} = \tau_{jj} = 0) \tag{5.13}$$

where $g_{ij} - g_{jj}$ is the binary interaction parameter of the NRTL model. The value of 0.3 was used for α_{12} according to recommendation by Renon and Prausnitz[258]. k_{12} and l_{12} in the vdW1 mixing rule, and k_{12}, $g_{12} - g_{22}$ and $g_{21} - g_{11}$ in the WS-NRTL mixing rule were treated as fitted parameters, and were regressed by minimizing the following objective function (F_{obj}):

$$F_{obj} = \sum_{k=1}^{NDP} \left(\frac{P_{exptl.} - P_{calcd.}}{P_{exptl.}} \right)_k^2 \tag{5.14}$$

where NDP is the number of experimental data points, and "exptl." and "calcd." are the experimental and calculated values, respectively.

6.3.2 GC-SAFT-VR

In the GC-SAFT-VR approach[22], the functional groups in molecules are represented by tangentially bonded segments that each have individual size and energy parameters. The functional group *i* in molecule *k* interacts with functional group *j* in molecule *l* through dispersive interactions via the square-well potential as described by,

$$u_{ki,lj}(r) = \begin{cases} +\infty & \text{if} \quad r < \sigma_{ki,lj} \\ -\varepsilon_{ki,lj} & \text{if} \quad \sigma_{ki,lj} \le r \le \lambda_{ki,lj}\sigma_{ki,lj} \\ 0 & \text{if} \quad r > \lambda_{ki,lj}\sigma_{ki,lj} \end{cases} \tag{5.15}$$

where r is the distance between the two groups, $\sigma_{ki,lj}$ is the segment diameter, and $\varepsilon_{ki,lj}$ and $\lambda_{ki,lj}$ are the dispersion energy well depth and range parameters, respectively. The cross interactions for size and energy between unlike segments can be expressed by Lorentz-Berthelot combining rules,

$$\sigma_{ki,lj} = \frac{\sigma_{ki,ki} + \sigma_{lj,lj}}{2} \tag{5.16}$$

$$\varepsilon_{ki,lj} = \xi_{ki,lj}\sqrt{\varepsilon_{ki,ki}\varepsilon_{lj,lj}} \tag{5.17}$$

$$\lambda_{ki,lj} = \gamma_{ki,lj}\left(\frac{\sigma_{ki,ki}\lambda_{ki,ki} + \sigma_{lj,lj}\lambda_{lj,lj}}{\sigma_{ki,ki} + \sigma_{lj,lj}}\right) \tag{5.18}$$

where $\xi_{ki,lj}$ and $\gamma_{ki,lj}$ are binary interaction parameters that enable adjustments to the cross interactions from the geometric and arithmetic mean values, respectively.

The definition if the Helmholtz free energy for a non-associating fluid in the GC-SAFT-VR approach is given by,

$$\frac{A}{Nk_BT} = \frac{A^{\text{ideal}}}{Nk_BT} + \frac{A^{\text{mono}}}{Nk_BT} + \frac{A^{\text{chain}}}{Nk_BT} \tag{5.19}$$

where N is the total number of molecules in the system, k_B is the Boltzmann constant, T is the absolute temperature, A^{ideal}, A^{mono}, and A^{chain} are the contributions to the Helmholtz free energy from the ideal, monomer, and hetero-segmented chain interactions, respectively. The reader is referred to the original publications[22,268] for details of the terms in equation 5.19, here we provide only the main expressions and a brief description of each term.

The ideal contribution to the Helmholtz free energy is given by,

$$\frac{A^{\text{ideal}}}{Nk_BT} = \sum_{k=1}^{n_{\text{components}}} x_k \ln\left(\rho_k {\Lambda_k}^3\right) - 1 \tag{5.20}$$

where $n_{\text{components}}$ represents the number of pure components in the system, x_k is the mole fraction of component k, ρ_k is the molecular number density, N_k/V, where N_k is the number of molecules of

component k and V is the volume of the system, and Λ_k is the de Broglie wavelength of component k.

The monomer contribution to the Helmholtz free energy is given by the temperature expansion of the second order Barker Henderson perturbation theory for mixtures[125],

$$\frac{A^{\text{mono}}}{Nk_BT} = \sum_{k=1}^{n}\sum_{i=1}^{n'_k} m_{ki}x_k\left(a^{\text{HS}} + \frac{a_1}{k_BT} + \frac{a_2}{(k_BT)^2}\right) \tag{5.21}$$

where n'_k is the number of types of functional groups i in a chain of component k and m_{ki} is the number of segments of type i in chains of component k. a^{HS}, a_1, and a_2 represent the hard-sphere reference term and the first and second order perturbation terms, respectively.

Finally, the contribution to the Helmholtz free energy from chain formation from the hetero-segmented monomer fluid is represented by,

$$\frac{A^{\text{chain}}}{Nk_BT} = -\sum_{k=1}^{n} x_k \sum_{ij} \ln y^{\text{SW}}_{ki,kj}\left(\sigma_{ki,kj}\right) \tag{5.22}$$

where the first sum is over all of the components, n, in the mixture, x_k is again the mole fraction of component k, the second sum considers the chain formation and the connectivity of the segments within a given component k. The background correlation function $y^{\text{SW}}_{ki,kj}$ is given by.

$$y^{\text{SW}}_{ki,kj}\left(\sigma_{ki,kj}\right) = \exp\left(\frac{-\varepsilon_{ki,kj}}{k_BT}\right) g^{\text{SW}}_{ki,kj}\left(\sigma_{ki,kj}\right) \tag{5.23}$$

where $\varepsilon_{ki,kj}$ is the segment-segment dispersion energy well depth and $g^{\text{SW}}_{ki,kj}(\sigma_{ki,kj})$ is the radial distribution function for the square-well monomers at the contact distance of $\sigma_{ki,kj}$ and is approximated by a first-order high temperature expansion[99].

Once the Helmholtz free energy is obtained, other thermodynamic properties, such as chemical potential and pressure can be calculated through standard thermodynamic relationships.

6.4 Results & Discussion

6.4.1 Experimental VLE Data for the Binary CO_2 + HFE-449mec-f or HFE-7200

VLE data for the binary systems CO_2 (1) + HFE-449mec-f or HFE-7200 (2) were measured at temperatures 303.15, 313.15, and 323.15 K. The experimental VLE data are listed in Tables 5.3 and 5.4, respectively.

Table 6.3. Experimental isothermal VLE data for the system CO_2 (1) + HFE-449mec-f (2) at temperatures (T) 303.15, 313.15, and 323.15 K. Pressure (P), liquid mole fraction (x_1), and vapor mole fraction (y_1).[a]

P (MPa)	x_1	y_1	P (MPa)	x_1	y_1
T = 303.15 K					
0.540	0.177	0.936	4.064	0.774	0.997
1.582	0.427	0.984	4.474	0.812	0.996
2.101	0.521	0.995	4.999	0.856	0.997
2.500	0.585	0.997	5.475	0.893	0.998
3.027	0.656	0.996	6.082	0.932	0.996
3.512	0.715	0.996			
T = 313.15 K					
0.602	0.167	0.955	4.874	0.780	0.995
0.970	0.253	0.977	5.447	0.824	0.995
1.669	0.396	0.984	6.126	0.869	0.992
1.911	0.437	0.987	6.417	0.888	0.990
2.454	0.521	0.992	6.841	0.911	0.993
2.979	0.590	0.993	7.584	0.951	0.996
3.370	0.636	0.991	8.022	0.974	0.996
3.802	0.681	0.997	8.118	0.974	0.991
4.352	0.733	0.994			
T = 323.15 K					
0.754	0.179	0.976	4.894	0.713	0.990
1.090	0.248	0.975	5.432	0.762	0.992
2.014	0.407	0.985	6.241	0.805	0.992
2.343	0.457	0.988	6.612	0.835	0.992
2.949	0.534	0.988	7.128	0.857	0.992
3.487	0.594	0.989	7.655	0.885	0.987
3.990	0.644	0.993	7.999	0.910	0.987
4.547	0.694	0.991			

[a] Standard uncertainties, u, are $u(T)$ = 0.1 K, $u(P)$ = 0.03 MPa, $u(x_1)$ = 0.007, and $u(y_1)$ = 0.007.

Table 6.4. Experimental isothermal VLE data for the system CO_2 (1) + HFE-7200 (2) at temperatures (T) 303.15, 313.15, and 323.15 K. Pressure (P), liquid mole fraction (x_1), and vapor mole fraction (y_1).[a]

P (MPa)	x_1	y_1	P (MPa)	x_1	y_1
T = 303.15 K					
0.550	0.133	0.965	4.020	0.699	0.993
1.057	0.244	0.982	4.460	0.751	0.994
1.493	0.325	0.988	5.056	0.817	0.995
2.074	0.426	0.990	5.565	0.871	0.995
2.549	0.501	0.992	5.722	0.887	0.995
3.065	0.577	0.992	6.110	0.923	0.996
3.499	0.634	0.993			
T = 313.15 K					
0.546	0.114	0.959	4.001	0.623	0.993
1.027	0.208	0.975	4.522	0.677	0.993
1.529	0.293	0.983	5.000	0.725	0.993
1.977	0.365	0.986	5.520	0.774	0.991
2.424	0.429	0.989	6.003	0.819	0.989
3.033	0.509	0.989	6.562	0.861	0.992
3.497	0.567	0.992			
T = 323.15 K					
1.032	0.195	0.973	5.019	0.681	0.994
1.507	0.272	0.988	5.489	0.722	0.996
1.922	0.340	0.991	5.941	0.763	0.992
2.500	0.424	0.983	6.577	0.801	0.998
3.020	0.478	0.992	7.063	0.841	0.999
3.522	0.539	0.990	7.505	0.875	0.994
3.996	0.583	0.994	8.063	0.901	0.997
4.471	0.634	0.995	8.603	0.933	0.992

[a] Standard uncertainties, u, are $u(T)$ = 0.1 K, $u(P)$ = 0.03 MPa, $u(x_1)$ = 0.007, and $u(y_1)$ = 0.007.

Plots of pressure (P) as functions of the liquid or vapor mole fraction of CO_2 (x_1 or y_1) for two systems are also presented in Figures 5.3 and 5.4, respectively. The pressure was measured up to about 8.6 MPa in this work. To our best knowledge, the experimental VLE data of these systems have not been previously reported in the literature. A comparison of Figures 5.3 and 5.4 shows that the P-x_1 diagram of the system CO_2 + HFE-7200, which has a higher carbon number, shifts to higher pressures, compared to the CO_2 + HFE-449mec-f system.

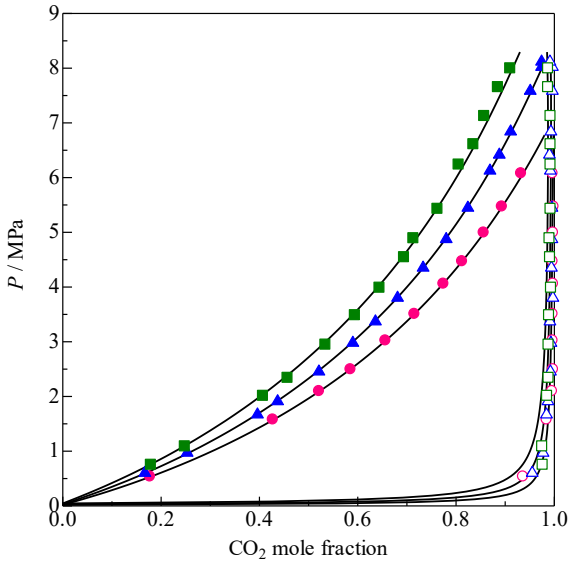

Figure 6.3. Experimental VLE data for the system CO_2 (1) + HFE-449mec-f (2) at 303.15, 313.15, and 323.15 K. Experimental data at liquid phase ; ● 303.15 K; ▲ 313.15 K; ■ 323.15 K, vapor phase ; ○ 303.15 K; Δ 313.15 K; □ 323.15 K. Results obtained from — PR EOS with vdW1 mixing rule.

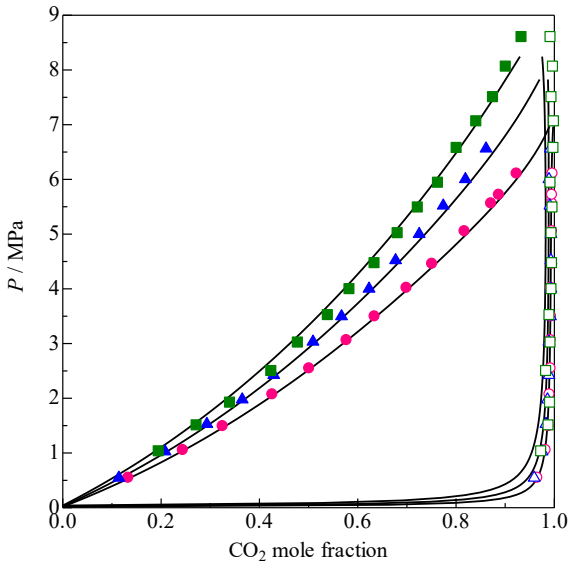

Figure 6.4. Experimental VLE data for the system CO_2 (1) + HFE-7200 (2) at 303.15, 313.15, and 323.15 K. Experimental data at liquid phase ; ● 303.15 K; ▲ 313.15 K; ■ 323.15 K, vapor phase ; ○ 303.15 K; Δ 313.15 K; □ 323.15 K. Results obtained from — PR EOS with vdW1 mixing rule.

6.4.2 Correlation

The determined parameters in both mixing rules along with the percentage average relative deviations of the experimental and calculated P, $|\Delta P/P|_{av.}$ and the average absolute deviations of the experimental and calculated y_1, $|\Delta y_1|_{av.}$, are provided in Table 5.5.

Table 6.5. Parameters and deviations between the calculated and experimental pressures ($|\Delta P/P|$)[a] and vapor phase mole fractions ($|\Delta y_1|$)[b], for the PR EOS combined with the vdW1 and WS-NRTL mixing rules and for the GC-SAFT-VR EOS both with and without the adjusted CO_2-CF_2 cross-interaction for the systems CO_2 (1) + HFE-449mec-f (2) and CO_2 (1) + HFE-7200 (2).

	CO_2 (1) + HFE-449mec-f (2)			CO_2 (1) + HFE-7200 (2)		
	303.15 K	313.15 K	323.15 K	303.15 K	313.15 K	323.15 K
Parameters of vdW1 mixing rule						
	k_{12} = –0.0516, l_{12} = 0.0436			k_{12} = 0.0322, l_{12} = 0.0430		
$\|\Delta P/P\|_{av.} \times 100$ (%)	0.6	0.6	1.5	1.6	2.2	2.9
$\|\Delta y_1\|_{av.}$	0.005	0.004	0.009	0.001	0.005	0.017
Parameters of WS-NRTL mixing rule						
	$g_{12} - g_{22}$ (J mol^{-1}) = 1604.893, $g_{21} - g_{11}$ (J mol^{-1}) = –2039.110 k_{12} = 0.4839, α_{12} = 0.3			$g_{12} - g_{22}$ (J mol^{-1}) = 5130.300, $g_{21} - g_{11}$ (J mol^{-1}) = –2325.171 k_{12} = 0.5940, α_{12} = 0.3		
$\|\Delta P/P\|_{av.} \times 100$ (%)	0.5	0.6	1.2	1.9	2.0	3.1
$\|\Delta y_1\|_{av.}$	0.005	0.004	0.009	0.001	0.004	0.012
GC-SAFT-VR						
$\|\Delta P/P\|_{av.} \times 100$ (%)	0.08	0.08	0.09	0.07	0.10	0.07
$\|\Delta y_1\|_{av.}$	0.007	0.014	0.017	0.094	0.100	0.065
GC-SAFT-VR with adjusted CO_2-CF_2 cross-interaction						
$\|\Delta P/P\|_{av.} \times 100$ (%)	0.09	0.07	0.09	0.08	0.09	0.08
$\|\Delta y_1\|_{av.}$	0.044	0.046	0.053	0.007	0.008	0.034

[a] $|\Delta P/P|_{av.} \times 100 = (100/\mathrm{NDP}) \sum_{k=1}^{\mathrm{NDP}} \left|(P_{\mathrm{exptl.}} - P_{\mathrm{calcd.}})/P_{\mathrm{exptl.}}\right|_k$.

[b] $|\Delta y_1|_{av.} = \sum_{k=1}^{\mathrm{NDP}} \left|y_{1,\mathrm{exptl.}} - y_{1,\mathrm{calcd.}}\right|_k / \mathrm{NDP}$, where NDP is the number of data points.

These parameters were determined per system and are temperature independent. The vdW1 mixing rule gave $|\Delta P/P|_{av.} \times 100$ and $|\Delta y_1|_{av.}$ of less than 2.9 % and 0.017, respectively for each dataset, whilst using the WS-NRTL mixing rule resulted in values of 3.1 % and 0.012. Thus, both models

show reasonable correlation of the results at all temperatures investigated. Figures 5.5 and 5.6 shows the relative deviations between the experimental and calculated P defined as $\left(P_{\text{exptl.}} - P_{\text{calcd.}}\right)/P_{\text{exptl.}} \times 100$ (%), and the absolute deviation between the experimental and calculated y_1 defined as $y_{1,\text{exptl.}} - y_{1,\text{calcd.}}$, as a function of liquid phase CO_2 mole fraction, x_1 in the systems CO_2 + HFE-449mec-f and CO_2 + HFE-7200, respectively. The values of $\left(P_{\text{exptl.}} - P_{\text{calcd.}}\right)/P_{\text{exptl.}} \times 100$ (%) and $y_{1,\text{exptl.}} - y_{1,\text{calcd.}}$ were generally within the uncertainties of the experimental pressure and vapor-phase mole fraction for both models; however, higher values were detected in some data of both systems, especially at temperature 323.15 K. The results of calculations using the vdW1 and WS-NRTL mixing rules are summarized graphically in Figures 5.5 and 5.6.

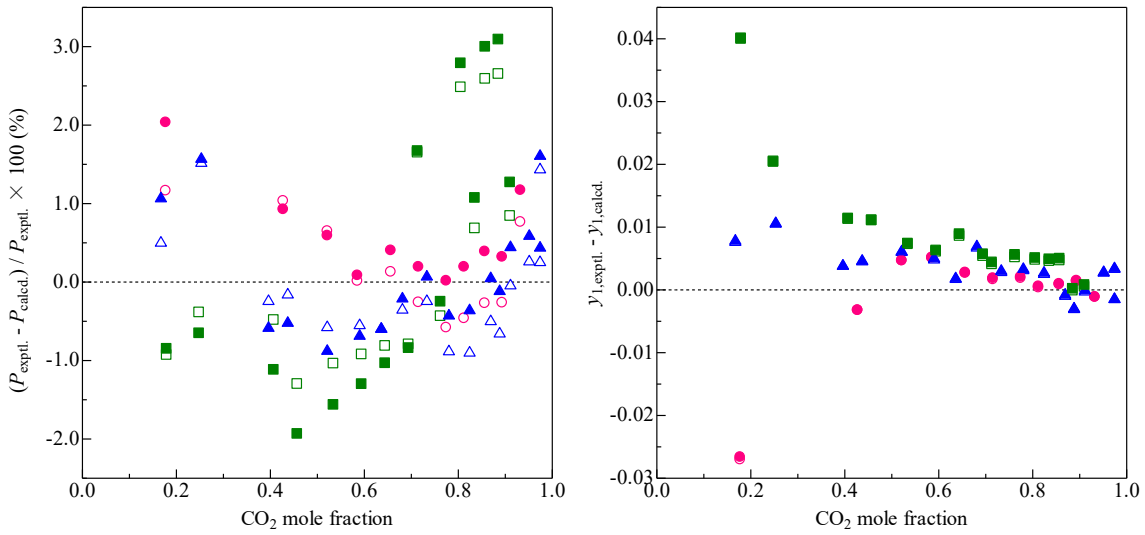

Figure 6.5. Relative deviations between the experimental and calculated results vs. CO_2 mole fraction for the system CO_2 (1) + HFE-449mec-f (2). PR EOS with vdW1 mixing rule at ● 303.15 K; ▲ 313.15 K; ■ 323.15 K. PR EOS with WS-NRTL mixing rule at ○ 303.15 K; Δ 313.15 K; □ 323.15 K. (a) $\left(P_{\text{exptl.}} - P_{\text{calcd.}}\right)/P_{\text{exptl.}} \times 100$ (%) and (b) $y_{1,\text{exptl.}} - y_{1,\text{calcd.}}$.

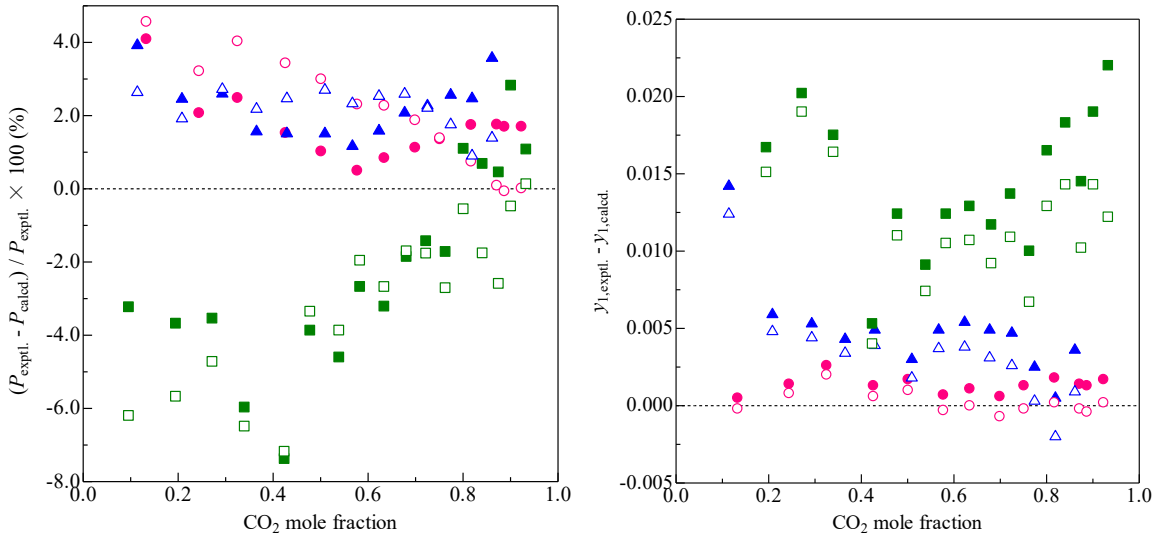

Figure 6.6. Relative deviations between the experimental and calculated results vs. CO_2 mole fraction for the system CO_2 (1) + HFE-7200 (2). PR EOS with vdW1 mixing rule at ● 303.15 K; ▲ 313.15 K; ■ 313.15 K. PR EOS with WS-NRTL mixing rule at ○ 303.15 K; Δ 313.15 K; □ 323.15 K. (a) $\left(P_{exptl.} - P_{calcd.}\right)/P_{exptl.} \times 100$ (%) and (b) $y_{1,exptl.} - y_{1,calcd.}$.

6.4.3 Prediction Using the GC-SAFT-VR

As shown in Figure 5.1, where each functional group is circled, HFE-449mec-f and HFE-7200 are both composed of CF_3, CF_2, CHF, CH_3, and ether CH_2O groups. The parameters for these functional groups were taken from previous work[22,47,120] and reported for completeness in Tables 5.6 – 5.8. Since CO_2 is a small molecule, it is not broken up into individual groups and represented by the SAFT-VR parameters proposed by dos Ramos et al.[237] as reported in Tables 5.6 – 5.8. Using these parameters, an average absolute deviation in the pressure ($|\Delta P/P|_{av.}$ %) for pure HFE-7200 of 2.02 % and 19.35 % for pure HFE-449mec-f compared to experimental data[230] are obtained. Likely, the high $|\Delta P/P|_{av.}$ % value for pure HFE-449mec-f is due to the additional CF_3 functional group present in the HFE-449mec-f molecule, instead of the smaller CH_3 functional group in HFE-7200. In Figs. 5.7 (a) and (b) respectively the constant temperature predictions of the CO_2 + HFE-449mec-f and CO_2 + HFE-7200 phase diagrams at 303.15, 313.15, and 323.15K are shown.

Table 6.6. GC-SAFT-VR parameters for the segment size, σ, and number, m, parameters for each of the groups studied.

Groups	σ_i (Å)	m_i
CO_2	2.774	2.000
CF_3	4.618	0.685
CF_2	4.345	0.370
OCH_2 (ether)	3.124	1.000
CHF	3.962	0.548
CH_3	3.737	0.667

Table 6.7. GC-SAFT-VR segment-segment dispersion energy range parameters $\lambda_{ki,lj}$.

	CO_2	CF_3	CF_2	OCH_2 (ether)	CHF	CH_3
CO_2	1.527	1.398	1.597	1.613	1.425	1.507
CF_3	1.398	1.321	1.476	1.470	1.336	1.398
CF_2	1.597	1.476	1.641	1.694	1.504	1.572
OCH_2 (ether)	1.613	1.470	1.694	1.690	1.502	1.582
CHF	1.425	1.336	1.504	1.502	1.354	-
CH_3	1.507	1.398	1.572	1.582	-	1.492

Note that these parameters differ from Haley et al.[47] due to a table misprint.

Table 6.8. GC-SAFT-VR segment-segment dispersion energy well depth parameters $\varepsilon_{ki,lj} / k_B$ (K).

	CO_2	CF_3	CF_2	OCH_2 (ether)	CHF	CH_3
CO_2	179.32	237.87	162.45	179.79	287.82	204.95
CF_3	237.87	315.56	262.81	238.50	381.81	271.88
CF_2	162.45	262.81	218.87	158.91	317.99	226.43
OCH_2 (ether)	179.79	238.50	158.91	180.27	288.58	205.49
CHF	287.82	381.81	317.99	288.58	461.98	-
CH_3	204.95	271.88	226.43	205.49	-	234.25

Note that these parameters differ from Haley et al.[47] due to a table misprint.

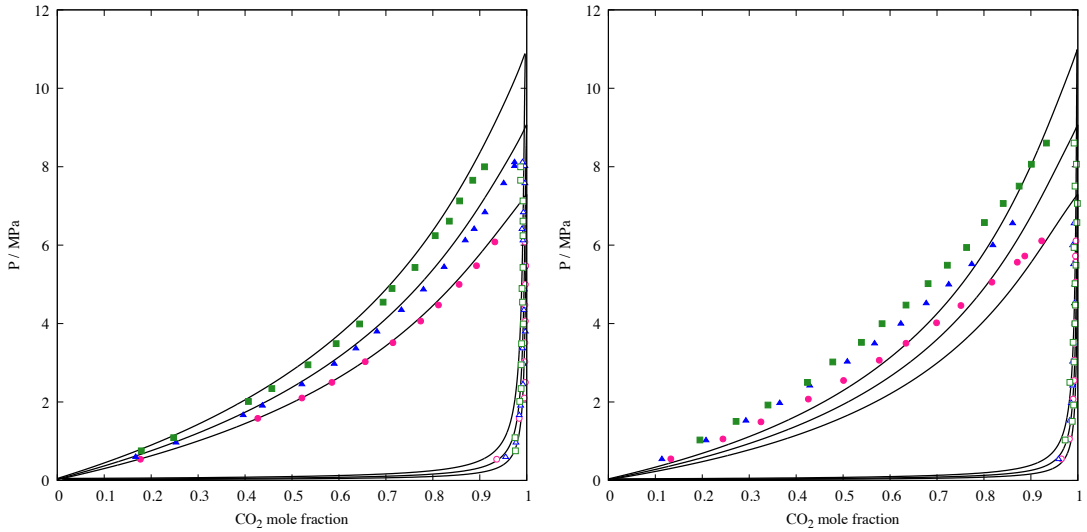

Figure 6.7. *Px* slices of (a) CO_2 (1) + HFE-449mec-f (2) and (b) CO_2 (1) + HFE-7200 (2) at constant temperatures of 303.15, 313.15, and 323.15 K. Solid lines correspond to predictions from the GC-SAFT-VR approach. Points correspond to experimental data presented here at liquid phase: ● 303.15 K, ▲ 313.15 K, ■ 323.15 K, and vapor phase: ○ 303.15 K, Δ 313.15 K, □ 323.15 K.

From the figures, it can be seen that the predictions are in good agreement with the experimental data, specifically for the CO_2 + HFE-449mec-f mixture (Fig. 5.7(a)). In order to quantitatively compare the experimental mixture data to the GC-SAFT-VR predictions, the average absolute deviation in the vapor phase mole fraction of CO_2 ($|\Delta y_1|_{av.}$) are reported in Table 5 along with the $|\Delta P/P|_{av}$ % values for the mixtures at 303.15, 313.15, 323.15 K. The $|\Delta y_1|_{av.}$ values are averaged across the 3 examined temperatures and deviations of 0.012 and 0.086 are obtained for the CO_2 + HFE-449mec-f and CO_2 + HFE-7200 systems, respectively. We note that this fit is purely predictive, since all parameters were obtained from a fit to pure component data, which is one of the advantages of using a group-contribution based SAFT approach. However, since the molecule set used to determine the interactions in fluorinated ether systems in the work of Haley et al.[47] was small, the use of an adjusted cross interaction between CO_2 and the CF_2 group was investigated to see if a better prediction of the CO_2 + HFE-7200 mixture could be obtained. The optimized cross interaction was fitted to the CO_2 + HFE-7200 system at 303.15 K and is reported

in reported in Tables 5.7 and 5.8. Although, the adjustment of this cross interaction away from the Lorentz-Berthelot value has a minimal effect on the CO_2 + HFE-449mec-f mixture ($|\Delta y_1|_{av.}$ of 0.012 to 0.047), as shown in Fig. 5.8 (a), it significantly improves the agreement with experimental data for the CO_2 + HFE-7200 system ($|\Delta y_1|_{av.}$ of 0.086 to 0.016) as can be seen in Fig. 5.8 (b) and reported in Table 5.5. Note that the cross interaction between CO_2 and CF_2 was fitted using the $|\Delta y_1|_{av.}$ values because of the small to nonexistent changes in the $|\Delta P/P|_{av}$ % values.

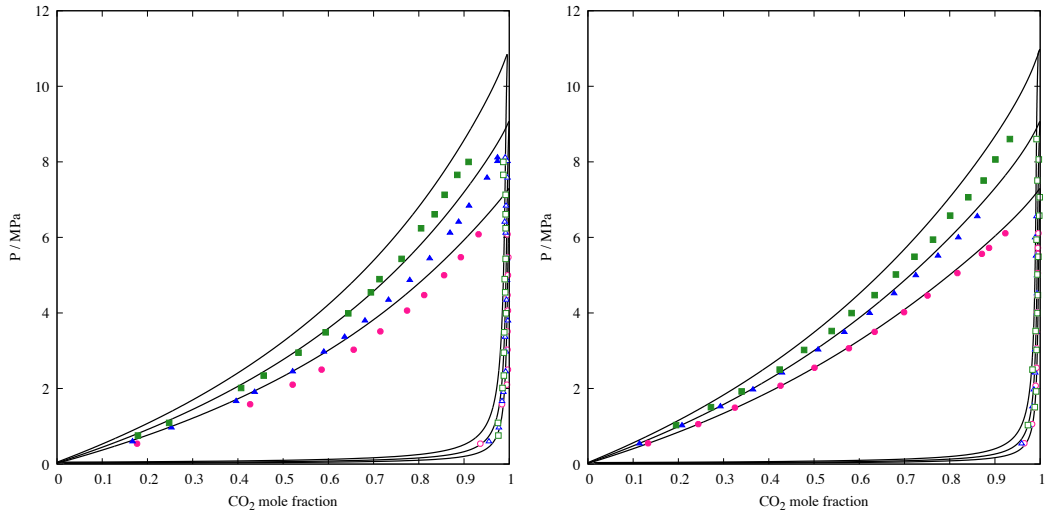

Figure 6.8. *Px* slices of (a) CO_2 (1) + HFE-449mec-f (2) and (b) CO_2 (1) + HFE-7200 (2) at constant temperatures of 303.15, 313.15, and 323.15 K with a binary interaction parameter between CO_2 and CF_2. Solid lines correspond to predictions from the GC-SAFT-VR approach. Points correspond to experimental data presented here at liquid phase: ● 303.15 K, ▲ 313.15 K, ■ 323.15 K, and vapor phase: ○ 303.15 K, Δ 313.15 K, □ 323.15 K.

Finally, the *p,T* projection of the fluid phase diagram was predicted for both mixtures with the parameter set that includes the optimized CO_2–CF_2 cross interaction and can be seen in Fig. 5.9. As can be seen from the figure type I phase behavior is found according to the scheme of Scott and van Konynenburg[269]. We note that both sets of parameters, i.e., with and without the adjusted CO_2–CF_2 cross interaction yield very similar phase diagrams. The GC-SAFT-VR approach, like all analytical equations of state, over predicts the critical point[110,270–272] and so the predicted critical

line is likely somewhat higher than the experimental values; however, we anticipate the type of phase diagram to be unaffected.

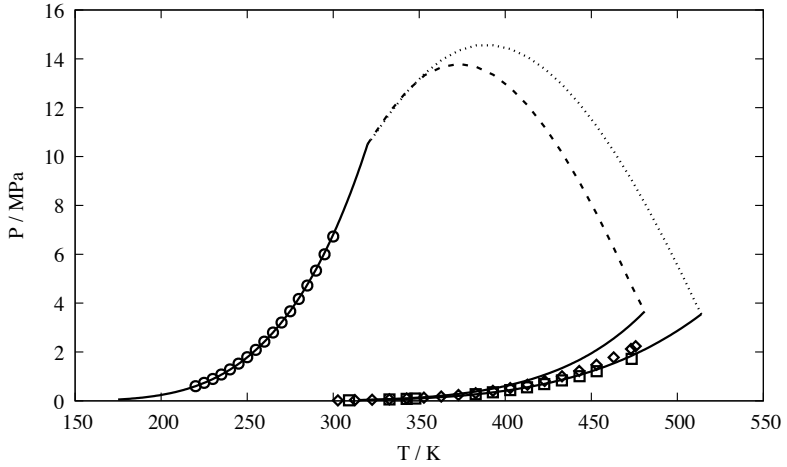

Figure 6.9. Projected pressure-temperature diagram of HFE-449mec-f + CO_2 (----) and HFE-7200 + CO_2 (·····) where the dotted lines represent the GC-SAFT-VR predicted critical line of both the mixtures utilizing the CO_2-CF_2 binary interaction parameter, the experimental data[206,230] for the pure components are shown as open symbols for CO_2 (○), HFE-449mec-f (◊), and HFE-7200 (□), and the solid lines are the GC-SAFT-VR predictions for the pure components presented here.

6.5 Conclusions

The experimental VLE data were obtained for two binary systems CO_2 + HFE-449mec-f or HFE-7200 at temperatures 303.15, 313.15, and 323.15 K and at pressure up to 9.0 MPa. This study furthers our understanding of these refrigerant mixtures as no experimental data were previously available for these two binary systems. The experimental VLE data were well correlated by the PR EOS with the vdW1and WS-NRTL mixing rules. These models provide reasonable agreements with the experimental data. The GC-SAFT-VR approach was also found to be able to correctly predict the phase behavior of the CO_2 + HFE binary mixtures. Due to the molecular polarity of the HFEs studied, optimization of the cross interaction between CO_2 and CF_2 was found to allow for better representation of the phase behavior than using Lorentz-Berthelot combining rules alone. Utilizing the fitted cross interaction the full phase diagram of

the CO_2 + HFE-449mec-f and CO_2 + HFE-7200 systems was also predicted, and type 1 phase behavior observed.

Chapter 7

Predicting the Thermodynamic Properties of Hydrofluoroethers and Fluorinated Mixtures with Carbon Dioxide Utilizing GC-SAFT-VR

7.1 Introduction and Background

Fluorinated molecules have received significant interest in recent years due to their wide ranging potential industrial and research applications.[36,216,217] For example, perfluoroalkanes, have increased solubility in carbon dioxide compared to their hydrocarbon equivalents,[37,38] giving them promising applications in removing carbon dioxide from gaseous effluents and in the design of carbon dioxide-philic surfactants. Other fluorinated molecules such as hydrofluoroethers (HFEs) also present exciting applications when mixed with carbon dioxide, notably, as a solution to replacing current industrial refrigerants, such as hydrochlorofluorocarbons (HCFCs) and hydrofluorocarbons (HFCs), which are being phased out due to environmental concerns. HFEs are an ideal greener replacement for current refrigerants due to their lower global warming potential, zero ozone depletion potential, and short atmospheric lifetimes.[39,40,230,238] However, due to their toxicity and flammability, HFEs alone cannot be used as refrigerants. Mixing HFEs with carbon dioxide has been shown to allow their beneficial environmental properties to remain, while helping eliminate their negative toxicity properties[43,45,47,50].

Due to the high interest in binary mixtures of perfluoroalkanes and carbon dioxide, there have been multiple experimental and theoretical studies performed on these systems. Perfluorohexane with carbon dioxide has been most widely considered both experimentally[42,252,273] and using theoretical methods such as the Statistical Associating Fluid Theory,[48] likely due to its high thermal stability. Limited experimental studies for perfluoroheptane[43,274] and perfluororooctane[41] with carbon dioxide have also been published, along with some theoretical

studies for perfluoroheptane and perfluorooctane using SAFT[48],[41]. Published work examining perfluorononane with carbon dioxide has been limited to experimental and correlative studies using methods such as the Peng-Robinson equation and the non-random two liquid (NRTL)[43] approach. However, none of the studies are comprehensive, including data from all available mixtures of perfluoroalkanes with carbon dioxide and a majority of the methods fit parameters to each molecule individually and are thus not predictive, making it difficult to expand on the current data. Therefore, a comprehensive overview of all the available experimental data for perfluoroalkane and carbon dioxide mixtures and a method to predict their phase behavior and expand upon the available data is needed.

Similarly, refrigerants and alternative refrigerants have been widely studied, but most of the studies have focused on HFCs[238,275–280] and hydrofluoroolefins (HFOs)[221,242,281,282]. Though the experimental and theoretical studies for HFCs are quite extensive, HFCs were phased out as industrial refrigerants by 2020, making HFCs of less interest in more recent years. Due to this, HFOs and HFEs have been of higher interest, largely driven by their use as possible alternative refrigerants to the current options[283,284]. HFOs have been more extensively studied by theoretical approaches as there is a larger set of experimental data against which to compare, in comparison to HFEs. Therefore, many of the theoretical HFE studies are limited due to the lack of experimental data to fit to and primarily focus on correlated data for a small group of HFEs, i.e., less than 5 HFEs at a time[19,46,98,220,225,285–288]. Though the agreement between the theoretical calculations and experimental data for the systems studied are reasonable, the parameters were adjusted to mixture data. Utilizing a model that could predict the thermodynamic properties of HFEs without having to fit to large sets of experimental data would greatly assist in the industrial adoption of HFEs. Finally, there have been some studies for mixtures of HFEs with other molecules[44,46,220,266,289],

however these studies center around the properties at atmospheric pressure, likely due to the difficulty of experimentally studying HFEs at high temperatures and pressures, making the higher temperature and pressure regime an area of interest, as little is currently known.

Herein a method to accurately represent pure fluid properties of HFEs utilizing the group contribution statistical associating fluid theory for potentials of variable range (GC-SAFT-VR) has been developed and their mixtures with carbon dioxide and some alcohols studied. GC-SAFT-VR is also used to study mixtures of perfluoroalkanes and carbon dioxide, including perfluorohexane, perfluoroheptane, perfluorooctane, and perfluorononane. While previous work utilized GC-SAFT-VR to study perfluorohexane and carbon dioxide,[47] other perfluoroalkanes with carbon dioxide were not considered.

GC-SAFT-VR combines SAFT-VR[99] with a group contribution[22] approach. This allows molecules to be built up from segments that have their own size and energy parameters and represent the different functional groups within each molecule. The chain retains the heterogeneity of the groups which allows for the location of association sites to be assigned to specific groups, which is not typically seen in other SAFT-based GC methods. The benefit of describing molecules by the functional groups that they are comprised is that parameters for each functional group and their cross interactions can typically be developed from a limited set of pure component data and used transferably to study other molecules containing the same functional groups, allowing the GC-SAFT-VR to be a highly predictive model. The only exception to determining model parameters from pure component data only, is for functional groups that are not contained within any pure components, such as carbon dioxide. Therefore, any cross interactions with carbon dioxide have to be fit to mixture data; however, this is typically done for one mixture at a single

temperature and used to describe the interactions with CO_2 in other systems of interest and at other state points in order to maintain the predictive power of the model.

GC-SAFT-VR parameters for a wide variety of functional groups that describe molecules including alkanes, alcohols, ketones, aromatics, esters, ethers and additional fluids, both associating and non-associating are available from previous work.[10,11,22,47,121,133] As a large set of functional groups have already been parameterized, here we introduce one new functional group to describe HFEs, the OCF_2 group. Additionally, we adjust the cross interaction between fluorinated molecules with carbon dioxide to more accurately represent mixtures of carbon dioxide and fluorinated molecules. All of the HFEs considered in this work are listed in Table 1 and have been numbered for ease of identification.

7.2 Models & Theory

The GC-SAFT-VR approach[22] represents the functional groups in a molecule as tangentially bonded segments that each have individual size and energy parameters. The entirety of this model and all expressions are outlined in Chapter 2.

We consider two different parameter sets for the HFE's studied in order to best describe all of the HFEs considered which are split into two groupings that we will refer to as linear and modular. Within these groupings, we fit a new OCF_2 functional group for each set of molecules. GC-SAFT-VR, like most GC methods, works very well for molecules that are built up from a base structure, like alkane or alcohols. As can be seen from Figure 7.1, the HFE molecules studied do not have a common base structure and so are expected to be more difficult to represent. In an effort to introduce some similarity between the molecules being studied the molecules were split into two groups. Parameters for the OCF_2 group were then fit to a small set of molecules in the linear

and nodular groups respectively, each with their own set of cross interactions. By splitting the HFEs we were able to develop two much more accurate parameter sets to describe HFEs. A comparison of the Average Absolute Deviations (%AAD) in vapor pressure and saturated liquid density for each step in the refitting process can be seen in Table 7.2. The modular and linear groups as well as their functional groupings are shown in Figure 7.1 with their full chemical name provided in Table 7.1. Additionally, we reconsider the cross interaction between carbon dioxide and fluorinated molecules as the previously documented cross interaction was ambiguous.[47] By refitting the interaction between carbon dioxide and fluorinated molecules, we are able to more accurately predict the properties of these binary mixtures.

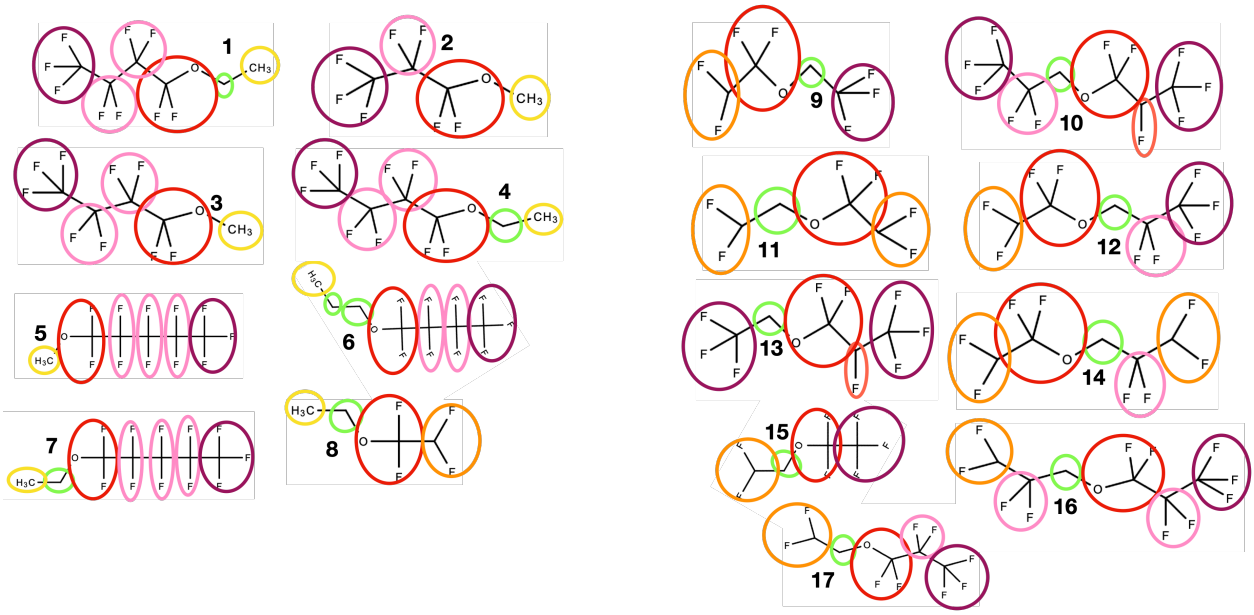

Figure 7.1. Schematic of molecular groupings for both linear (left) and modular (right) HFE molecules considered in this work

Table 7.1. Names of all HFEs included in this work with numbers to refer to them more easily throughout.

	Number	Name
Linear Molecules	1	1-ethoxy-1,1,2,2,3,3,4,4,4-nonafluorobutane (HFE-569mccc)
	2	heptafluoro-1-methoxypropane (HFE-7000)
	3	methoxy-nonafluorobutane (HFE-7100)
	4	1-ethoxy-1,1,2,2,3,3,4,4,4-nonafluorobutane (HFE-7200)
	5	1,1,1,2,2,3,3,4,4,5,5-undecafluoro-5-methoxypentane
	6	1,1,1,2,2,3,3,4,4-nonafluoro-4-propoxybutane
	7	1-ethoxy-1,1,2,2,3,3,4,4,5,5,5-undecafluoropentane
	8	1-ethoxy-1,1,2,2-tetrafluoroethane
Modular Molecules	9	1,1,2,2-tetrafluoroethyl 2,2,2-trifluoroethyl ether (HFE-347pc-f)
	10	2,2,3,3,3-pentafluoropropyl(1,1,2,3,3,3-hexafluoropropyl) ether (HFE-54-11mec-f)
	11	1-(2,2-difluoroethoxy)-1,1,2,2-tetrafluoroethane (HFE-356pc-f)
	12	1,1,1,2,2-pentafluoro-3-(1,1,2,2-tetrafluoroethoxy)propane (HFE-449mcf-c)
	13	1,1,1,2,3,3-hexafluoro-3-(2,2,2-trifluoroethoxy)propane (HFE-449mec-f)
	14	1,1,2,2-tetrafluoro-3-(1,1,2,2-tetrafluoroethoxy)propane (HFE-458pcf-c)
	15	1-(2,2-difluoroethoxy)-1,1,2,2,2-pentafluoroethane
	16	1,1,1,2,2,3,3-heptafluoro-3-(2,2,3,3-tetrafluoropropoxy)propane
	17	1-(2,2-difluoroethoxy)-1,1,2,2,3,3,3-heptafluoropropane

7.3 Results & Discussion

We first considered a large set of HFE molecules using previously published GC-SAFT-VR parameters for fluorinated molecules.[47] As the initial set of HFEs considered was smaller and the parameters only fit to vapor pressure data, refitting the parameters in order to more accurately represent HFE molecules was considered. The availability of a more comprehensive set of HFE data,[290–293] as well as expanding the number of HFEs considered, enabled more robust parameters for HFEs to be determined.

Refitting the cross interactions for the OCH_2 (ether) group was first attempted; however, this only minorly improved the representation of pure HFEs. Reexamining the grouping of the functional groups in the molecule was then considered and a new OCF_2 group defined for HFEs. The addition of the OCF_2 group was found to improve the accuracy of the theoretical calculations for pure HFEs (see Table 7.2); however, the results were inconsistent with some of the HFEs being

significantly better represented than others suggesting that a new functional group may be able to better represent these molecules. Upon examining these results and the structure of the molecules it became apparent that there were two classes of HFEs to consider. Specifically, about half of the HFEs considered were essentially linear, similar to alkanes, while the other half seemed to have no obvious building block pattern and were much denser structures in terms of the functional groups they contained (see Figure 7.1). Therefore, the HFEs were split into two groups: linear and modular, as described above.

Table 7.2. Comparison of the Average Absolute Deviations in Pressure and in liquid density for each step in the fits. The first column is when new cross interactions were introduced to the existing OCH_2 group. The second column was when we first introduced the OCF_2 group to the entire set of HFEs. The third column is the final fit for splitting the HFEs into linear and modular groups.

	OCH_2 Refit		**OCF_2 Group Introduced**		**Separate OCF_2 group for modular vs linear**	
Molecule	%AADP	%AADρ_{liq}	%AADP	%AADρ_{liq}	%AADP	%AADρ_{liq}
1	41.28	20.38	22.14	4.60	4.92	1.08
2	18.25	3.81	22.58	10.70	11.72	2.23
3	30.28	2.68	4.85	9.29	6.62	2.74
4	37.36	2.37	24.69	8.05	9.77	1.77
5	32.99	5.45	8.17	4.61	10.00	1.88
6	35.50	4.77	28.76	3.37	6.23	1.19
7	38.85	5.30	25.34	3.10	4.53	1.42
8	14.48	3.89	7.67	7.48	9.65	2.51
9	15.89	1.53	45.28	13.59	3.26	8.92
10	48.91	8.55	31.97	16.16	12.66	15.56
11	28.86	1.13	29.92	12.37	9.36	9.90
12	42.33	1.87	27.02	6.96	5.44	7.30
13	29.90	4.92	11.93	14.74	8.31	9.29
14	36.19	2.01	27.54	6.58	8.41	8.45
15	54.24	2.61	11.21	10.25	9.39	7.95
16	62.21	5.20	49.11	4.39	10.68	4.18
17	61.55	3.84	24.40	8.57	14.67	4.11
Average	37.00	4.72	23.68	8.52	8.57	5.32

For the linear group of HFEs, the parameters were fit to the vapor pressure and saturated liquid density data of HFE-569mccc (1) and HFE-7000 (2), while the modular parameter set was optimized against the vapor pressure and saturated liquid density data of HFE-347pc-f (9), HFE-54-11mec-f (10) and HFE-356pc-f (11) using the squared difference, where the numbers in parenthesis correspond to the HFE molecules listed in Table 7.1. As is customary in GC-SAFT-VR and in SAFT in general, the data close to the critical point was excluded from the fitting as it has been shown to skew the results.[294] All of the parameters used to describe HFEs, including the newly developed OCF_2 parameters for both modular and linear HFEs are summarized in Tables 7.3-7.5. Aside from the OCF_2 group, the remainder of the parameters for the HFEs in Tables 7.3 - 7.5 and other molecules represented in this work are taken from previous GC-SAFT-VR publications.[10,22,120,121,237] The association interactions for the OH functional group can be found in Table 7.6.

Table 7.3. GC-SAFT-VR parameters for the segment size, σ, and segment number, m, of each functional group studied.

Functional Group	**σ (Å)**	**m_i**
OCF_2 (linear)	3.450	1.010
OCF_2 (modular)	5.020	0.480
CF_3	4.618	0.685
CF_2	4.345	0.370
$CF_2\alpha$	4.345	0.370
CHF_2	3.076	1.577
CHF	3.962	0.548
CH_3	3.73	0.667
CH_2	4.041	0.333
OH (linear)	5.299	0.176
OH (branched)	6.474	0.102
CO_2	2.774	2.000

Table 7.4. GC-SAFT-VR segment-segment dispersion energy range parameters $\lambda_{ki,lj}$.

	OCF_2 (linear)	OCF_2 (modular)	CF_3	CF_2	$CF_2\alpha$	CHF_2	CHF	CH_3	CH_2	OH (linear)	OH (branched)	CO_2
OCF_2 (linear)	1.906	1.641	1.354	1.758	1.758	1.637	1.611	1.691	1.672	1.651	1.947	1.737
OCF_2 (modular)	1.641	1.459	1.393	1.543	0.991	1.667	1.413	1.473	1.552	1.472	1.746	1.483
CF_3	1.354	1.393	1.321	1.476	1.476	1.327	1.336	1.397	1.482	1.409	1.699	1.398
CF_2	1.758	1.543	1.476	1.641	1.641	1.515	1.504	1.572	1.660	1.555	1.837	1.597
$CF_2\alpha$	1.758	0.991	1.476	1.641	1.641	1.515	1.504	1.572	1.819	1.555	1.837	1.597
CHF_2	1.637	1.667	1.327	1.515	1.515	1.336	1.346	1.421	1.524	1.430	1.765	1.427
CHF	1.611	1.413	1.336	1.504	1.504	1.346	1.354	1.421	1.512	1.429	1.736	1.425
CH_3	1.691	1.473	1.397	1.572	1.572	1.421	1.421	1.492	1.583	1.488	1.795	1.507
CH_2	1.672	1.552	1.482	1.660	1.741	1.524	1.512	1.583	1.667	1.564	1.853	1.610
OH (linear)	1.651	1.472	1.409	1.555	1.555	1.430	1.429	1.488	1.564	1.485	1.751	1.499
OH (branched)	1.947	1.746	1.699	1.837	1.837	1.765	1.736	1.795	1.853	1.751	1.969	1.836
CO_2	1.737	1.483	1.398	1.597	1.597	1.427	1.425	1.507	1.610	1.499	1.836	1.527

Table 7.5 GC-SAFT-VR segment-segment dispersion energy well depth parameters $\varepsilon ki,lj/k_B$ (K).

	OCF_2 (linear)	OCF_2 (modular)	CF_3	CF_2	$CF_2\alpha$	CHF_2	CHF	CH_3	CH_2	OH (linear)	OH (branched)	CO_2
OCF_2 (linear)	116.57	205.02	287.69	154.87	159.73	182.10	232.06	165.25	166.30	249.69	198.81	115.66
OCF_2 (modular)	205.02	360.57	337.32	280.92	280.92	194.91	408.14	290.63	292.47	439.13	349.65	254.28
CF_3	287.69	337.32	315.56	262.81	262.81	299.60	381.81	271.88	273.61	410.81	327.10	237.88
CF_2	154.87	280.92	262.81	218.87	218.87	249.51	317.98	226.43	172.48	342.13	272.41	172.35
$CF_2\alpha$	159.73	280.92	262.81	218.87	218.87	249.51	317.98	226.43	227.87	342.13	272.41	172.35
CHF_2	182.10	194.91	299.60	249.51	249.51	284.45	362.51	258.13	259.77	390.03	310.56	225.85
CHF	232.06	408.14	381.81	317.98	317.98	362.51	461.98	328.97	331.05	497.06	395.77	287.82
CH_3	165.25	290.63	271.88	226.43	226.43	258.13	328.97	234.25	235.74	353.95	281.82	204.95
CH_2	166.30	292.47	273.61	172.48	227.87	259.77	331.05	235.74	237.23	356.19	283.61	206.25
OH (linear)	249.69	439.13	410.81	342.13	342.13	390.03	497.06	353.95	356.19	534.81	425.83	309.68
OH (branched)	198.81	349.65	327.10	272.41	272.41	310.56	395.77	281.82	283.61	425.83	339.06	246.57
CO_2	115.66	254.28	237.88	172.35	172.35	225.85	287.82	204.95	206.25	309.68	246.57	179.32

Table 7.6 GC-SAFT-VR Segment-segment site-site association energy parameters and bonding volume available to associate for the OH functional group.

$\varepsilon_{ki,lj}^{HB}/k_B\,(K)$	2797.000
$K_{ki,lj}^{HB}(\text{Å}^3)$	0.16014

7.3.1 Pure Fluids

For the OCF_2 functional group, each parameter set was fit to HFEs selected from the linear (HFE-569mccc (1) and HFE-7000 (2)) and modular (HFE-347pc-f (9), HFE-54-11mec-f (10) and HFE-356pc-f (11)) HFE groups. The two molecules chosen for each group were the two molecules that allowed for the most accurate representation of each set of HFEs after considering multiple combinations. While the addition of the OCF_2 functional group to better describe HFEs is the only new functional group that was introduced, cross interactions between the OCF_2 group and other known functional groups were also optimized as needed. Specifically, for linear molecules cross interactions between OCF_2 and CH_2, OCF_2 and CF_3, and OCF_2 and CF_2 were optimized, with the remaining interactions being described by Lorentz-Berthelot combining rules. For the modular molecules, interactions between OCF_2 and CHF_2 as well as OCF_2 and $CF_2\alpha$ were optimized. The difference in the cross interactions between the two classes of molecules is based on exploiting the differences in molecular structures between the two groups. For example, the linear molecules do not contain $CF_2\alpha$ groups where multiple modular molecules do, making a $CF_2\alpha$ cross interaction unnecessary in the linear molecules, but useful in the modular molecule set. Conversely, only one modular group contains a CF_2 group while almost all the linear molecules contain the CF_2 group making that cross interaction more effective in the linear molecules. It was also noted that in linear molecules, each of the CH_2 groups were directly next to a CH_3 group, whereas in the modular molecules the CH_2 groups were typically near fluorinated groups. As shown by Haley et al.,[47] the strong electronegativity difference between CH_2 and fluorinated molecules, results in different cross interactions leading us to optimize a cross interaction for the linear molecules between OCF_2 and CH_2.

It can be seen in Table 7.2 that the average %AADP for the linear molecules is only slightly lower than the %AADP for the modular molecules, while the linear molecule set %AADρ_{liq} is significantly lower than that for the modular molecule set. This can be attributed to the fact that typically GC-SAFT methods work best for molecules that build up linearly, similar to alkanes. Therefore, %AADP and %AADρ_{liq} values are both below 15% for the modular HFEs is considered reasonably accurate. For the linear HFE molecules, all of the %AADP values are below 12%, while the %AADρ_{liq} are below 3% which are considered good agreements for HFE molecules. Graphical representations for the linear and modular vapor pressure and saturated liquid density curves can be seen in Figures 7.2 and 7.3 respectively.

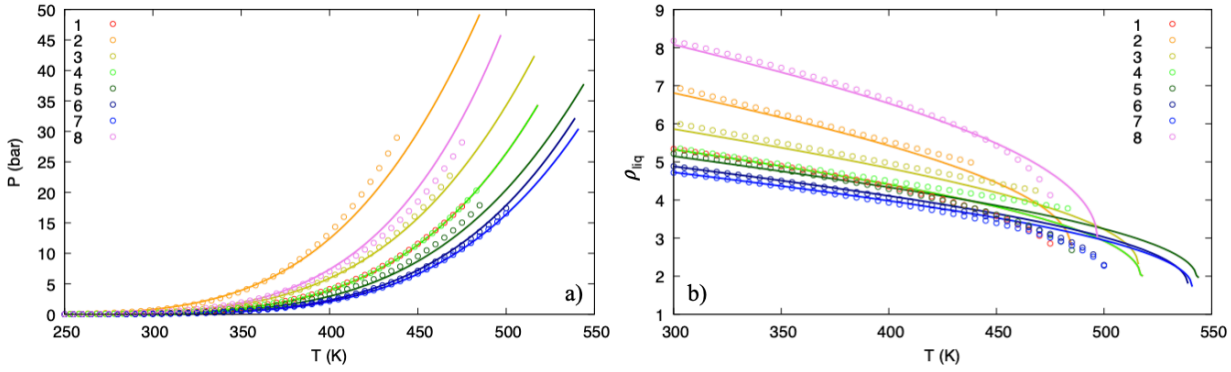

Figure 7.2. Comparison between theoretical results from the GC-SAFT-VR approach and experimental data[290–293] for a) the vapor pressure and b) the saturated liquid density data for the linear HFEs studied. The legends show which colors correspond to which linear HFEs, while the lines represent the fitted GC-SAFT-VR results for linear HFE and the symbols represent the experimental data.[290–293]

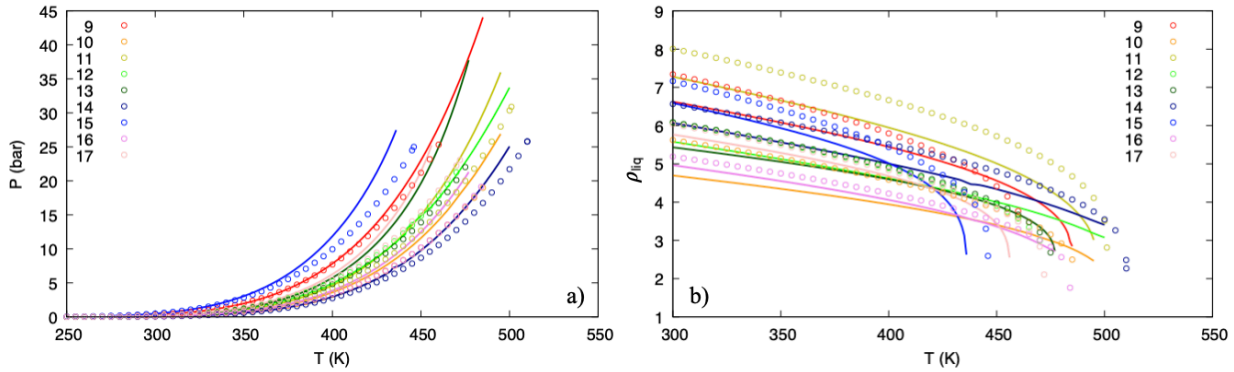

Figure 7.3. Comparison between the theoretical results from the GC-SAFT-VR approach and experimental data[290–293] for a) the vapor pressure and b) saturated liquid density data for the modular HFEs studied. The legends show which colors correspond to which modular HFEs, while the lines represent the fitted GC-SAFT-VR results for modular HFE molecules and the symbols represent the experimental data.[290–293]

In previous work,[45] two HFE molecules that are also included in this work, HFE-7200 (4) and HFE-449mec-f (13) were studied. The parameters used were the previously published parameters[47], that were developed before the expansion of the dataset and the subsequent splitting of the parameters into a set for modular versus linear HFE molecules. Therefore, a comparison of the results from this earlier work and those with the new parameters developed herein is included in Figure 7.4. As can be seen from the figure, the updated parameters are able to represent the experimental vapor pressure curves more accurately than the original parameters.

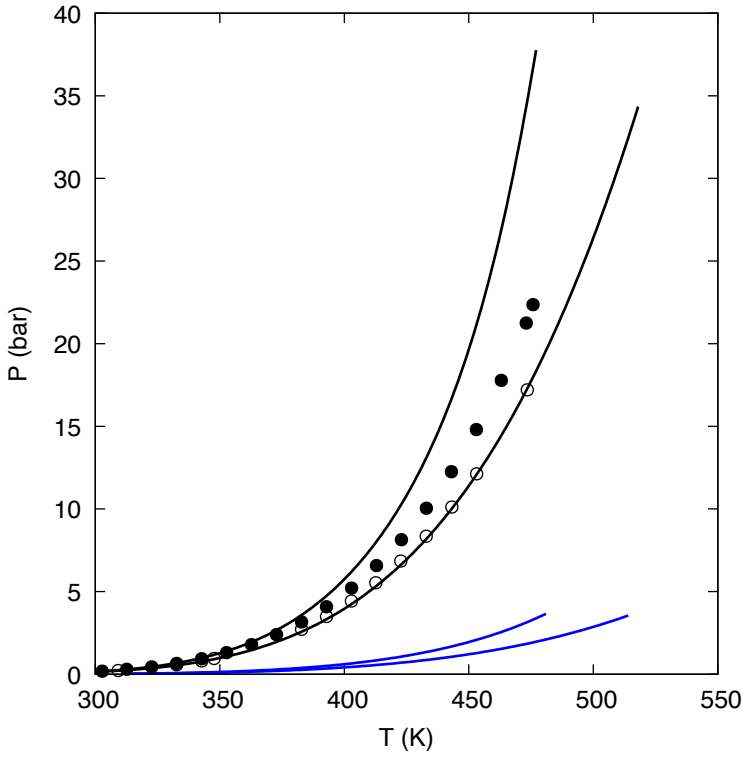

Figure 7.4. Comparing the vapor pressure curves of HFE-7200 (4) and HFE-449mec-f (13) utilizing the published parameters for HFEs (blue lines) to the new parameters for HFEs (black lines) with the experimental vapor pressure data[45] for (o) HFE-7200 and (•) HFE-449mec-f.

7.3.2 Binary Mixtures

Unfortunately, there is also minimal experimental mixture data available in the literature for binary mixtures involving HFEs. The primary mixtures of interest are fluorinated compounds mixed with carbon dioxide as they have promising applications as alternative refrigerants. Therefore, due to the lack of mixture data for HFEs, additional fluorinated molecules mixed with carbon dioxide are also considered. Due to an error in the cross interaction that was proposed between carbon dioxide and fluorinated functional groups in earlier work,[47] a new cross interaction with carbon dioxide was optimized. Typically, in order to maintain a predictive model, within the GC-SAFT approach cross interaction parameters are fitted only to pure fluid data, enabling purely predictive mixture calculations. However, since carbon dioxide is not a functional group that is contained within other molecules, and is itself a molecule, all cross interactions with carbon dioxide must be optimized

against experimental mixture data. In order to retain some predictive power, cross interaction between CO_2 and CF_2 are fitted to data for perfluorohexane at a single temperature and then utilized to study perfluorohexane at other temperatures and with larger perfluoroalkane molecules and the interactions between CO2 and other fluorinated molecules.

While, perfluoroalkanes have been studied by multiple groups[42,48,50,218,234,252] these studies did not consider multiple perfluoroalkanes with carbon dioxide comprehensively. At most each study only considered two perfluoroalkanes at a time, whereas herein we consider 4 perfluoroalkanes (perfluorohexane, perfluoroheptane, perfluorooctane, and perfluorononane). The cross interaction was fit to the vapor pressure and saturated liquid density data of the binary mixture of perfluorohexane and carbon dioxide by[42] at 303.15 K and can be seen in the Figure 7.5 with the predicted constant temperature slices at 313.15 K as well as 323.15 K. These results are comparable to those results of the correlated data using the SRK equation of state in Tochigi et al.[42]. An additional broader data set[252] for perfluorohexane that ranges from 273.14 K to 333.18 K can be seen in Figure 7.6. As seen in Figure 7.6, this theoretical predictions agree well with the experimental data, thought as the temperature increases the observed deviations increase. This could be explained by the fact that this specific set of experimental data has slightly lower pressure values compared to other experimental data sets at the higher temperatures, which can be seen in the original publication[252].

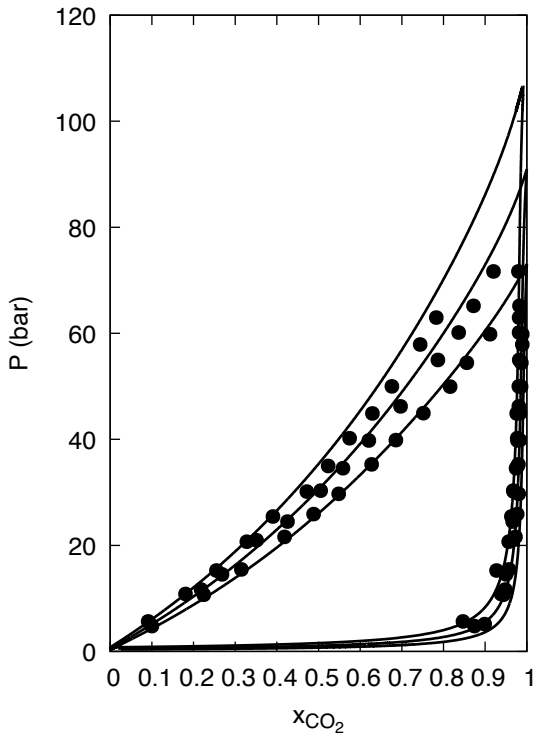

Figure 7.5. *Pxy* phase diagram for perfluorohexane + carbon dioxide at 303.15 K, 313.15 K, 323.15 K (bottom to top). The interaction between the CF_2 and CO_2 groups was fitted to experimental data at 303.15 K. The lines represent the GC-SAFT-VR calculations and the points the experimental data[42].

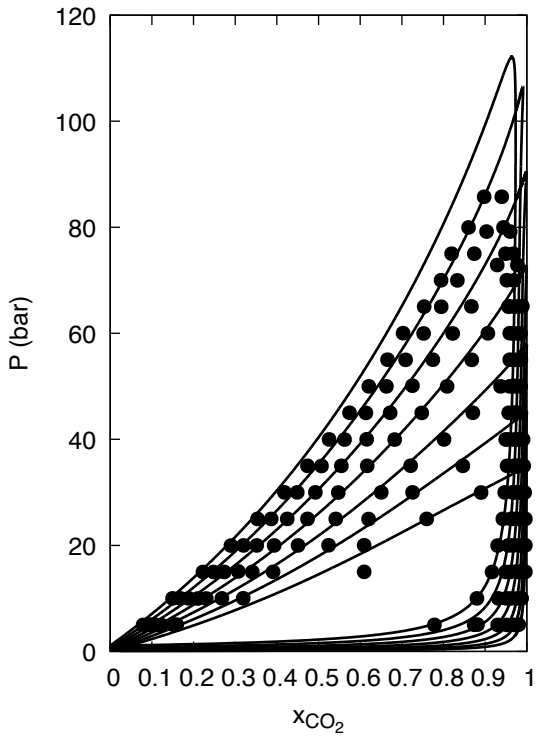

Figure 7.6. Predictions of the *Pxy* phase diagram for perfluorohexane + carbon dioxide at 273.14 K, 283.15 K, 293.16 K, 303.14 K, 313.16 K, 323.16 K, and 333.18 K (bottom to top). The lines correspond to the GC-SAFT-VR predictions and the symbols represent the experimental data[252].

Turning to longer perfluoroalkane molecules, the *Pxy* phase diagram of perfluoroheptane and carbon dioxide at 273.14 K, 293.13 K, and 313.13 K are shown in Figure 7.7 and compared to experimental data[43]. As seen in Figure 7.7, the agreement between the experimental data and GC-SAFT-VR data is quite accurate, even close to the critical point. In the *Pxy* phase diagram for the binary mixture of perfluorooctane and carbon dioxide at seven constant temperature slices ranging from 293.15 K to 353.15 K, shown in Figure 7.8, the typical overprediction of the critical point is seen, while phase behavior is quite accurately predicted. Finally, constant temperature slices of the binary mixture of the perfluorononane and carbon dioxide system at 273.15 K, 293.15 K, and 313.15K is studied, as shown in Figure 7.9. Good agreement between the theoretical predictions and the experimental data is seen, with the theory accurately capturing the shapes of the experimental constant temperature slices well.

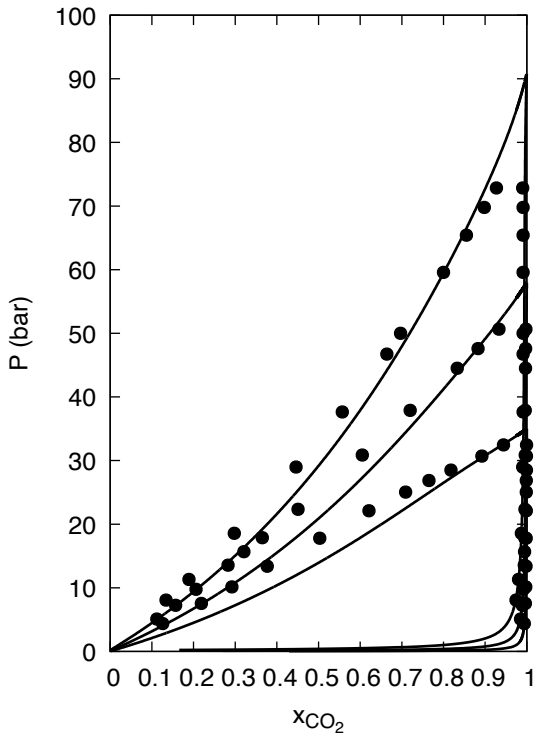

Figure 7.7. *Pxy* predictions of the perfluoroheptane + carbon dioxide binary mixture at 273.14 K, 293.13 K, and 313.13 K (bottom to top). The lines correspond to the GC-SAFT-VR predictions and the symbols the experimental data[43].

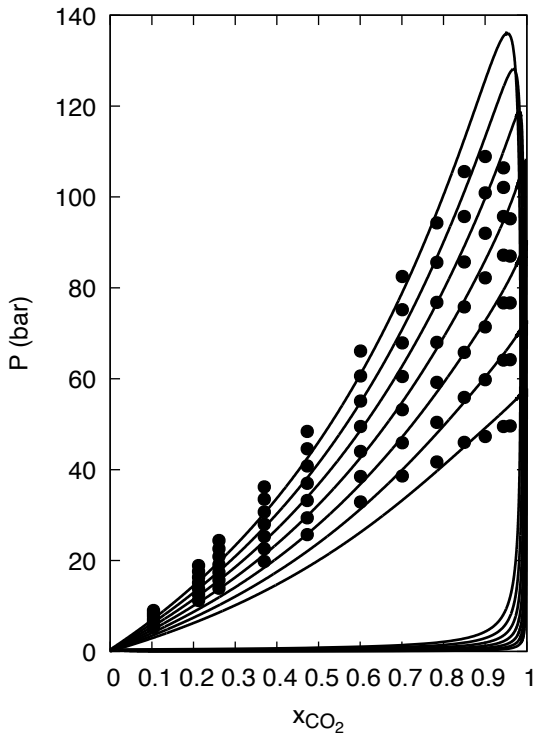

Figure 7.8. *Pxy* predictions of the perfluorooctane + carbon dioxide binary mixture at 293.15 K, 303.15 K, 313.15 K, 323.15 K, 333.15 K, 343.15 K, and 353.15 K (bottom to top). The lines correspond to the GC-SAFT-VR predictions and the symbols to the experimental data[41].

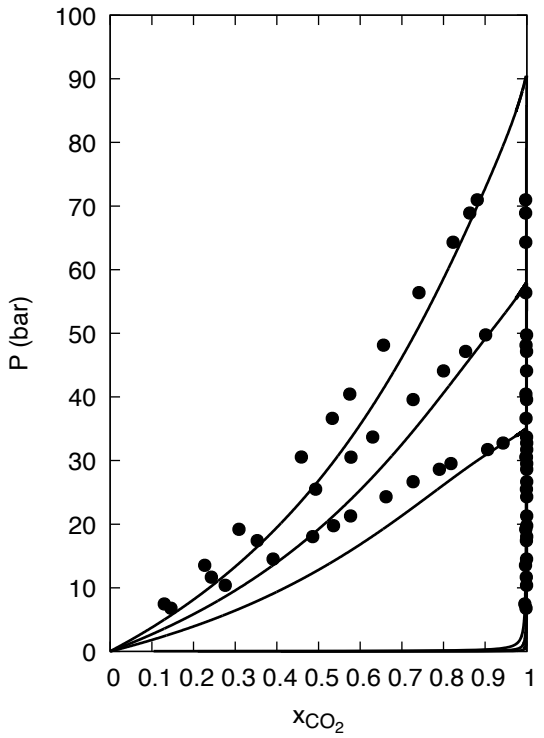

Figure 7.9. Predictions of the *Pxy* phase diagram for perfluorononane + carbon dioxide at 273.15 K, 293.15 K, and 303.15 K (bottom to top). The lines correspond to the GC-SAFT-VR predictions and the symbols the experimental data[43].

In addition to the perfluoroalkane systems studied, two other fluorinated molecules are considered in mixtures with carbon dioxide. The first, a binary mixture of 1,1,1,2,3,4,4,5,5,5-decafluoropentane and carbon dioxide, which can be seen in Figure 7.10. The theoretical predictions agree with the experimental data quite well. Data for 1,1,1,2,3,4,4,5,5,5-decafluoropentane was only available at one constant temperature slice of 298.15 K, but due to the accurate match at this point, it is within reason that additional constant temperature points could also be predicted as well where desired. The second fluorinated molecule considered is 2,2,2-trifluoroethanol with carbon dioxide at 298.15 K and 313.15 K, shown in Figure 7.11. 2,2,2-trifluoroethanol is an associating molecule due to its alcohol group, even so, the parameters and cross interactions for all other fluorinated molecules were still able to accurately represent the phase behavior of this mixture. As seen in the original publication for the experimental data[273],

this experimental dataset is slightly lower than those in other works, which may explain the slight overprediction as the mole fraction moves closer to pure carbon dioxide.

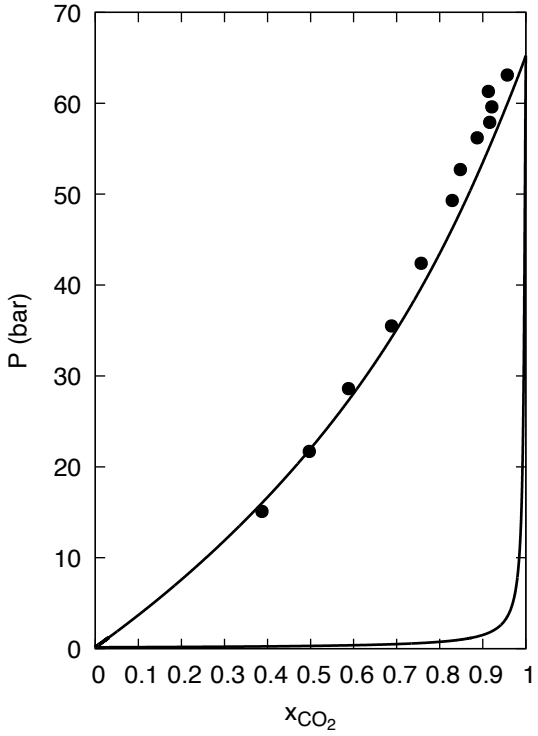

Figure 7.10. *Pxy* prediction of the 1,1,1,2,3,4,4,5,5,5-decafluoropentane + carbon dioxide binary mixture at 298.15 K. The lines correspond to the GC-SAFT-VR predictions and the symbols to the experimental data[295].

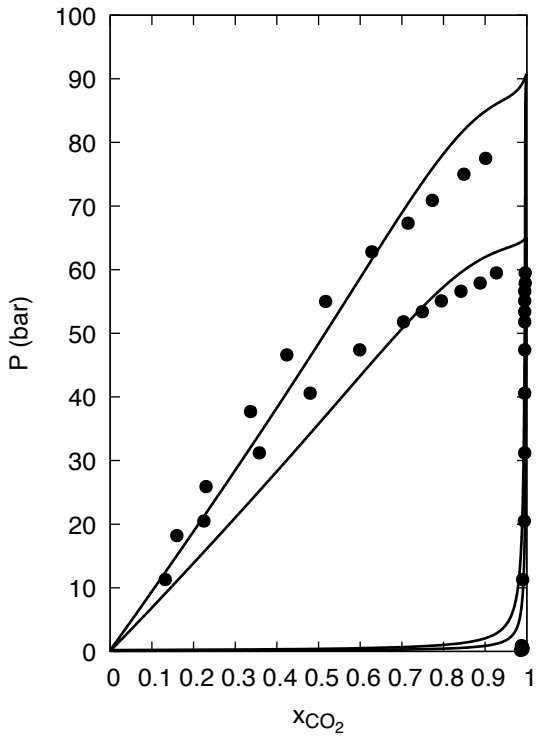

Figure 7.11. *Pxy* predictions of the 2,2,2-trifluoroethanol + carbon dioxide binary mixture at 298.15 K and 313.15 K. The lines correspond to GC-SAFT-VR predictions and the symbols represent the experimental data[273].

Binary mixtures of HFEs and carbon dioxide were then studied using the cross-interaction parameters derived for the simple fluorinated molecules presented thus far. It is worth noting here, that there is limited data available for HFE mixtures, so while we can predict mixture data for any HFE that we have represented here, there is a limit in the experimental data available for comparison. We first examine binary mixtures of linear HFEs with carbon dioxide, for which we found that an additional cross interaction with carbon dioxide greatly improved the theoretical predictions in comparison to the available experimental data. The cross interaction was optimized between the linear OCF_2 group and CO_2 using experimental data for HFE-7200 and carbon dioxide at 303.15 K. The modular molecules did not require any additional cross interactions in order to be well represented in mixtures with carbon dioxide. As each OCF_2 functional group has an independent full set of parameters for linear and modular molecules, the cross interactions needed

will differ. Additionally, the intermolecular polarity differences in the linear molecules are greater as they each have a non-fluorinated terminal side as opposed to the more uniformly polar fluorinated modular molecules. This may explain the need for the additional carbon dioxide cross interaction.

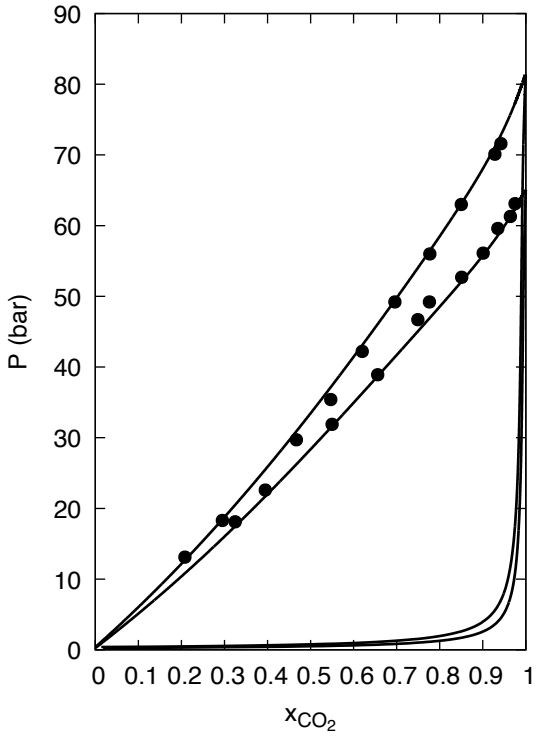

Figure 7.12. *Pxy* predictions of the HFE-7100 (3) + carbon dioxide binary mixture at 298.15 K and 308.15 K. The lines correspond to the GC-SAFT-VR predictions and the symbols to the experimental data[295].

The two linear HFEs considered here in binary mixtures with carbon dioxide are HFE-7100 (3) and HFE-7200 (4). In Figure 7.12, we show two constant temperature slices at 298.15 K and 308.15 K for HFE-7100 (3) and carbon dioxide. The agreement between the experimental data and predicted data for this mixture is extremely close, even up to the critical point. Considering that for the calculations for thus mixture are purely predictive, the agreement is impressive. Figure 7.13 shows the binary mixture of HFE-7200 (4) and carbon dioxide at 4 constant temperature slices

ranging from 298.15 K to 323.15 K. The results here were more accurate compared to the previous work of Matsuda et al.[45], which further shows the accuracy of the new parameter sets for HFEs.

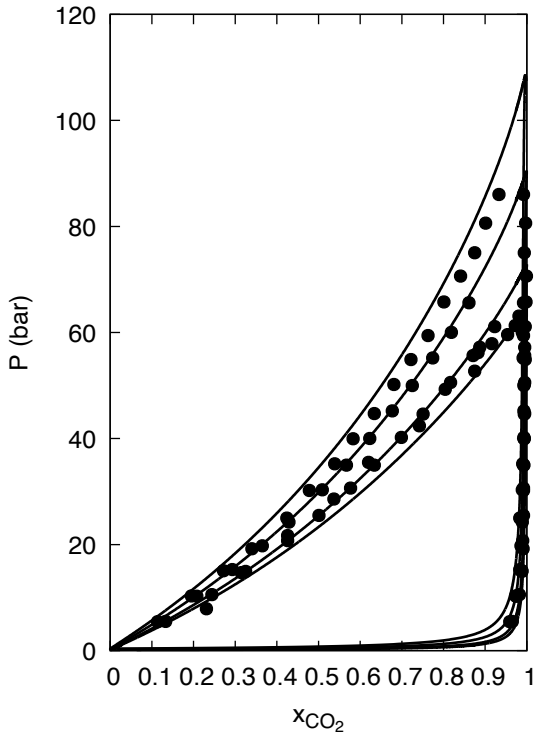

Figure 7.13 *Pxy* slices of the HFE-7200 (4) + carbon dioxide binary mixture at 298.15 K, 303.15 K, 313.15 K, and 323.15 K (bottom to top). The phase behavior at 303.15 K was used to fit the interaction between the OCF_2 (linear) and CO_2 groups, while the other 3 temperatures were predicted. The lines correspond to the GC-SAFT-VR results and the symbols correspond to the experimental data[45,295].

Furthermore, two modular HFEs were also considered in a binary mixture with carbon dioxide, HFE-458pcf-c (14) and HFE-449mec-f (13). For each of these, the only cross interaction between the HFE and carbon dioxide that is used is the one between CO_2 and $CF_2\alpha$, which was fit to perfluorohexane. To clarify, though the cross interaction was fit specifically to CF_2, $CF_2\alpha$ shares the same parameter set as CF_2 and was only developed to change the cross interactions between CH_2 and CF_2 in molecules that contained these functional groups directly next to one another due to a high electronegativity difference. Therefore, utilizing the same cross interactions to other functional groups outside of CH_2 is reasonable as these two functional groups are equivalent

outside of that singular interaction. Additionally, this only applies to HFE-458pcf-c (14), as HFE-449mec-f (13) does not contain the CF_2 or $CF_2\alpha$ functional groups. Figure 7.14 shows the constant temperature slices of HFE-458pcf-c (14) and carbon dioxide at 273.13 K, 293.16 K, and 313.16 K. The prediction for this data is quite reasonable compared to the experimental data, especially compared to the correlated data that was cited in initial publication[43]. In Figure 7.15, the binary mixture of HFE-449mec-f (14) and carbon dioxide at constant temperature slices of 303.15 K, 313.15 K, and 323.15 K is shown, and the accuracy of the predicted data is quite impressive compared to the experimental data. These results are also significantly closer to the experimental data than the original presentation of this data with the previous parameter sets for HFEs using GC-SAFT-VR in Matsuda et al.[45].

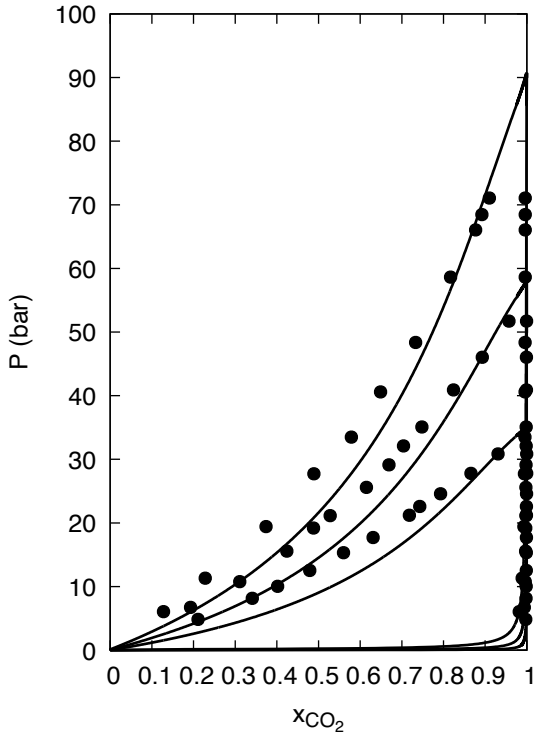

Figure 7.14. *Pxy* predictions of HFE-458pcf-c (14) + carbon dioxide binary mixtures at 273.13 K, 293.16 K, and 313.16 K (bottom to top). The lines correspond to GC-SAFT-VR and the symbols to the experimental data[43].

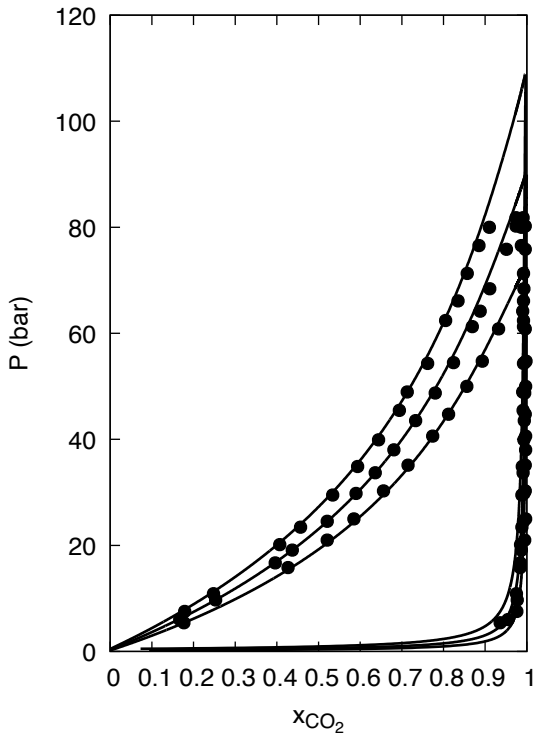

Figure 7.15. *Pxy* predictions of HFE-449mec-f (13) + carbon dioxide binary mixtures at 303.15 K, 313.15 K, and 323.15 K. The lines correspond to GC-SAFT-VR predictions and the symbols to the experimental data[45].

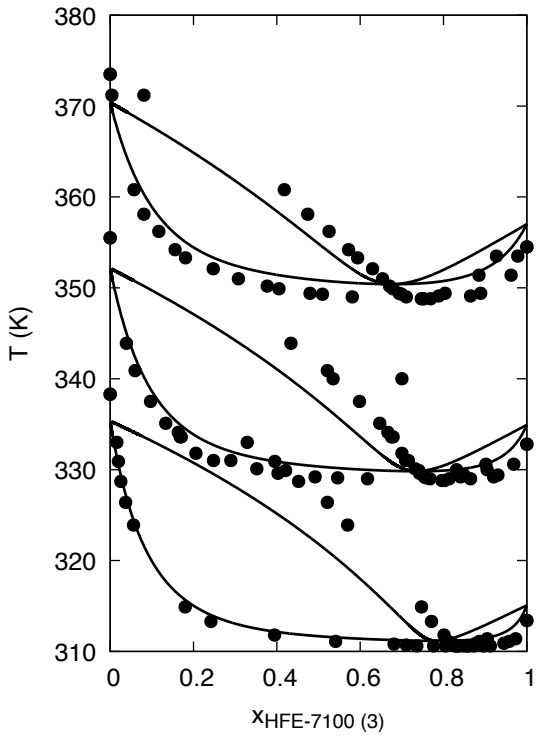

Figure 7.16. *Txy* predictions of HFE-7100 (3) + 2-propanol binary mixtures at 0.5 bar, 1.013 bar, and 2.0 bar (bottom to top). The lines correspond to the GC-SAFT-VR predictions and the symbols correspond to experimental data[219].

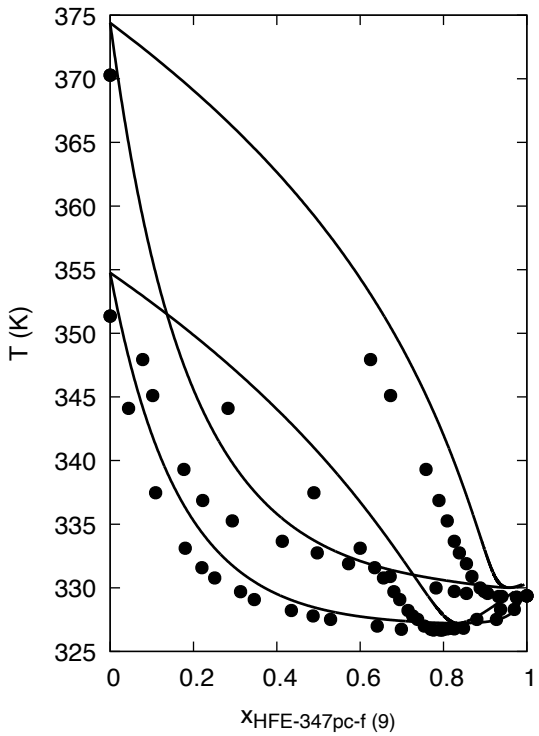

Figure 7.17. *Txy* predictions of the ethanol (bottom) and propanol (top) + HFE-347pc-f (9) binary mixtures at atmospheric pressure. The lines represent the GC-SAFT-VR predictions and the symbols represent the experimental data[220].

Finally, given the limited experimental mixture data for HFEs we were unable to compare to other datasets involving CO2; however, to further test the model parameters developed in Figures 7.16 and 7.17 we show comparisons of ethanol and propanol with a linear and modular HFE, respectively. In each of these systems, the alcohols contain associating groups, but the HFEs do not. We did consider adding association sites to the HFEs in order to allow for possible cross association; however, it did not improve the accuracy of the calculations. Additionally it has been documented in previous studies of HFEs using SAFT that association sites on HFEs is not necessary[49,98,224]. First, in Figure 7.16 constant pressure slices at 0.5 bar, 1.013 bar, and 2 bar for the binary mixture of HFE-7100 (3) and 2-propanol are shown. As can be seen from the figure, these match the experimental data quite well, especially considering the calculations are at a lower pressure than previously considered. Second, constant pressure slices at atmospheric pressure for

the binary mixture of HFE-347pc-f and ethanol and propanol are shown in Figure 7.17. Again, the agreement is quite reasonable, especially on the pure HFE side. The pure alcohol sides of the plots are slightly higher than the experimental data, which is most likely due to the small size of ethanol and propanol compared to the overall molecule set of alcohols of which the parameters were fit to.

7.4 Conclusions

In this work, the GC-SAFT-VR approach was expanded to better represent HFEs by introducing a new OCF_2 functional group parameterized for both modular and linear HFE molecules. By splitting the HFEs into linear and modular groups and fitting the parameter sets to vapor pressure and saturated liquid density data of selected HFEs from each of the linear and modular groups, much better agreement with the pure HFE data was achieved in comparison with the previous parameters used, allowing for additional HFEs to be represented than in the original works. These parameters were then used to accurately predict the properties of additional linear and modular HFEs both pure and in binary mixtures.

Additionally, new cross-interaction parameters between fluorinated molecules and carbon dioxide were proposed to better represent mixtures for a variety of fluorinated molecules. This not only allowed us to better represent perfluoroalkanes in a mixture with carbon dioxide, but also to represent HFE mixtures with carbon dioxide more accurately, especially compared to previously published results.[45] The ability to accurately represent a large set of HFEs has not been seen before as they are so structurally different from one another. Therefore, the ability to concisely represent these molecules by splitting them into two groups greatly improves the ability to predict the thermodynamic parameters of HFEs going forward. The HFE parameters developed can be used

in a transferable fashion to additional HFEs as more data becomes available as well, allowing for quicker and more accurate predictions going forward.

Chapter 8

Conclusions and Future Directions

With ever evolving environmental regulations and concern for lowering the human impact on the globe, the need for a reliable method to predict fluid properties is more present now than ever. In order to find greener alternatives to some of the highest polluting processes, knowledge of the physical properties for a large set of potential alternative chemicals is necessary. There are many potential alternatives to consider, but little is known about the properties of many of these fluids. In this thesis specifically, we consider confined fluids for filtration, fatty acid methyl ester molecules that compose biodiesel, the removal of sulfur pollutants from typical petroleum, and possible alternative refrigerants through fluorinated molecules. For each of these systems, there is a lack of thermodynamic and phase behavior information available, which significantly delays their potential implementation.

Due to the large range of possible alternative fluids and combinations of various fluid mixtures, experimental studies are infeasible. Additionally, some of the compounds are toxic, flammable, expensive, or difficult to synthesize, making experimental studies inefficient in propelling the use of these compounds forward. Furthermore, many simpler equation of state studies require extensive experimental data to fit to, making them also inefficient in studying a large range of these molecules. Therefore, we developed a GC-SAFT-VR based approach that can be used to predict the properties for a wide range of fluids and their mixtures that are of interest in the drive towards greener applications.

Recognizing that the theoretical approaches to describe confined fluids are significantly lacking in comparison to their bulk counterparts, in Chapter 3 we developed a fully analytical approach to describe confined fluids. We introduce a new an analytical theory that combines the

second-order Barker-Henderson perturbation theory and scaled particle theory in order to represent the properties of confined fluids in a random porous media. The random porous media is composed of hard-sphere obstacles that are randomly placed in a hard-sphere fluid quenched at equilibrium. This new approach was able to get reasonable results compared to Monte Carlo simulations under various size and energy constraints. To further this work, this method could be adjusted to predict the properties of more complex confined fluids. Namely, associating simple fluids were considered briefly after publishing this work, but the results were never compared to Monte Carlo methods to assure their validity. Associating fluids, in particular, would be interesting as it would include water which is broadly used in many aspects. Moreover, adjusting the expression to utilize a different potential instead of the Morse potential, such as the square-well potential to compare to the current model may illuminate which potential is better able to represent these systems. However, changing the potential would change the expressions significantly and depending on the potential used could take away from the analytical nature of the model.

For Chapters 4 – 7 we utilize the GC-SAFT-VR approach to predict the thermodynamic properties and phase behavior of various fluids and their mixtures, with a strong emphasis on complex fluorinated molecules. First in Chapter 4 we utilize GC-SAFT-VR to predict the properties of molecules that would allow for greener petroleum, through the removal of impurities and alternative fuels. Specifically, cyclic sulfur molecules, which are the main impurities in petroleum, and fatty acid methyl ester (FAME) molecules, which are the main components in biodiesel are considered. First, we utilize previously parametrized functional groups to represent fatty acid methyl ester (FAME) molecules. For the FAME molecules, no additional functional groups were parameterized or introduced, showing the true transferable nature of the GC-SAFT-VR equation. Using GC-SAFT-VR in a purely predictive fashion for FAME molecules, the

functional groups that were already parameterized could also be used to predict the properties of other molecules that are built up of functional groups that have already been introduced. The transferability shown here opens up a wide range of options on possible molecules that can be represented using GC-SAFT-VR with no experimental data needed to fit the parameters to. For sulfur molecules, new functional groups were fit to accurately represent multiple types of cyclic molecules. The main sulfur molecule considered was thiophene, which is one of the leading impurities in petroleum that causes pollution. Both pure thiophene and various binary mixtures with thiophene were considered and gave reasonable results compared to experimental data. Since the cyclic sulfur molecules were originally parameterized, there has been an emphasis on more complex cyclic sulfur molecules in the literature. As there are already a parameterized functional group for sulfur molecules, it would be reasonable to extend this work to include the groups needed to consider more complex cyclic sulfur molecules.

Chapter 5 is the beginning of an extensive study of fluorinated molecules. Multiple types of fluorinated molecules were considered including perfluoroalkanes, perfluoroalkylalkanes, branched fluorinated alkanes, 1,1-difluoroalkanes, 1-fluoroalkanes, and hydrofluoroethers. All fluorinated molecules were initially studied with functional group parameters from the literature and in general reasonable agreement with experimental data was found, except for hydrofluoroethers (HFEs) which were not well represented.

Mixtures of fluorinated molecules with alkanes, alkenes, alcohols, and carbon dioxide were also considered. The majority of these mixtures were reasonably represented, with the exception of the perfluorobutane and butane mixture. This may be due to the fact that both of these molecules are quite small. It is shown however that this mixture is reasonably represented within a certain temperature range. In future work, these molecules could be expanded upon to better home in on

the exact temperature range that these molecules can be represented well. Additionally, another set of experimental data to compare to might yield different results as often different experimental datasets vary slightly and the margin of pressures is small in this case.

Given the deviations observed in chapter 5, HFEs were reconsidered in Chapter 6. Two HFE molecules, HFE-449mec-f and HFE-7200, and their mixtures with carbon dioxide were examined. Chapter 6 was a collaborative project with an experimental group, which allowed us to reparametrize the functional groups needed to represent HFEs. The cross interaction between carbon dioxide and those HFEs was also re-fitted. The agreement to experimental data was considered reasonable, however, the AAD values for the pure and the mixtures were still higher than is typically acceptable for SAFT predictions. Therefore, further consideration of HFEs was needed, and presented in Chapter 7.

In Chapter 7 we expanded the set of HFE molecules studied using GC-SAFT-VR as well as introduced saturated liquid density to optimize the parameters against in order to develop better parameters for HFE molecules. The initial HFE parameters were fit to experimental vapor pressure data only, whereas fitting to both vapor pressure and saturated liquid density is customary and shown to improve parameter estimation. The AAD values when new HFE experimental data and new HFE molecules were considered were however still much higher than is acceptable. Therefore, a new functional grouping for HFE molecules was introduced in order to better represent these molecules. Much lower AAD values were obtained for the pure HFEs upon the introduction of the new functional group and the split of the HFEs into linear and modular molecules. Moreover, predictions for the HFEs mixtures were considerably more accurate in comparison to the available experimental data, especially compared to the previous work with HFEs. With the new functional group for HFEs and the splitting of molecules, an expansion of

this parameter set to represent additional HFE molecules would most likely show a similar improved agreement. Additional experimental data for HFE molecules is available, but they were not considered here due to the need for additional functional groups or an additional HFE molecule groups outside of the linear and modular molecule groups presented. As HFEs have promising possible applications as alternative refrigerants, the ability to predict more HFE properties would be an asset in evaluating their suitability.

In this thesis, additional functional groups for GC-SAFT-VR were introduced as well as other previous parameters clarified and revised. Upon the expansion of these functional groups, the possible molecules that are now able to be represented has grown, and as was shown with the FAME molecules, these parameters can be used transferably to represent molecules outside of these molecule classes. Additionally, all systems considered can be expanded to a broader range of temperatures and pressures than those that are included here.

Chapter 9

References

1. Molina, M. *et al.* Reducing abrupt climate change risk using the Montreal Protocol and other regulatory actions to complement cuts in CO2 emissions. *Proc. Natl. Acad. Sci. U. S. A.* **106**, 20616–20621 (2009).
2. Dobrzanski, C. D., Maximov, M. A. & Gor, G. Y. Effect of pore geometry on the compressibility of a confined simple fluid. *J. Chem. Phys.* **148**, (2018).
3. Bock, H. & Schoen, M. Phase behavior of a simple fluid confined between chemically corrugated substrates. *Phys. Rev. E - Stat. Physics, Plasmas, Fluids, Relat. Interdiscip. Top.* **59**, 4122–4136 (1999).
4. Hung, F. R. *et al.* Molecular modeling of freezing of simple fluids confined within carbon nanotubes. *J. Chem. Phys.* **122**, (2005).
5. Votyakov, E. V., Tovbin, Y. K., MacElroy, J. M. D. & Roche, A. Theoretical study of the phase diagrams of simple fluids confined within narrow pores. *Langmuir* **15**, 5713–5721 (1999).
6. Ford, D. M. & Glandt, E. D. Vapor-liquid phase equilibrium in random microporous matrices. *Phys. Rev. E* **50**, 1280–1286 (1994).
7. Kierlik, E., Rosinberg, M. L., Tarjus, G. & Monson, P. A. Phase diagrams of a fluid confined in a disordered porous material. *J. Phys. Condens. Matter* **8**, 9621–9625 (1996).
8. Kierlik, E., Rosinberg, M. L., Tarjus, G. & Monson, P. A. Phase diagrams of single-component fluids in disordered porous materials: Predictions from integral-equation theory. *J. Chem. Phys.* **106**, 264–279 (1997).
9. Nelson, A. K., Kalyuzhnyi, Y. V., Patsahan, T. & McCabe, C. Liquid-vapor phase equilibrium of a simple liquid confined in a random porous media: Second-order Barker-Henderson perturbation theory and scaled particle theory. *J. Mol. Liq.* **300**, (2020).
10. Haley, J. D. & McCabe, C. Modeling the thermodynamic properties and phase behaviour of organic sulfur molecules with a group contribution based statistical associating fluid theory approach (GC-SAFT-VR). *Fluid Phase Equilib.* (2017). doi:10.1016/j.fluid.2017.03.027
11. Haley, J. D. & McCabe, C. Predicting the phase behavior of fatty acid methyl esters and their mixtures using the GC-SAFT-VR approach. *Fluid Phase Equilib.* **411**, 43–52 (2016).
12. Colwell, R. R., Walker, J. D. & Cooney, J. J. Ecological aspects of microbial degradation of petroleum in the marine environment. *Crit. Rev. Microbiol.* **5**, 423–445 (1977).
13. Al-Hawash, A. B. *et al.* Principles of microbial degradation of petroleum hydrocarbons in the environment. *Egypt. J. Aquat. Res.* **44**, 71–76 (2018).
14. Adipah, S. Introduction of Petroleum Hydrocarbons Contaminants and its Human Effects. *J. Environ. Sci. Public Heal.* **03**, 1–9 (2018).
15. Hiyoshi, N. *et al.* Purification of hydrocarbons from aromatic sulfur compounds by supercritical carbon dioxide extraction. *J. Supercrit. Fluids* **55**, 122–127 (2010).
16. Elizalde-Solis, O. & Galicia-Luna, L. A. Solubility of thiophene in carbon dioxide and carbon dioxide + 1-propanol mixtures at temperatures from 313 to 363 K. *Fluid Phase Equilib.* **230**, 51–57 (2005).
17. Elizalde-Solis, O. & Galicia-Luna, L. A. Solubility of thiophene + pentane and thiophene + octane binary mixtures in supercritical carbon dioxide at temperatures from 333 to 383

K. *Ind. Eng. Chem. Res.* **44**, 5757–5760 (2005).
18. Mendo-Sánchez, R. P., Sánchez-García, C., Galicia-Luna, L. A. & Elizalde-Solis, O. Vapor-liquid equilibrium for the ternary carbon dioxide+ethanol+n-hexane and quaternary carbon dioxide+ethanol+n-hexane+thiophene systems. *Fluid Phase Equilib.* **315**, 40–45 (2012).
19. Gross, J. & Sadowski, G. Perturbed-chain SAFT: An equation of state based on a perturbation theory for chain molecules. *Ind. Eng. Chem. Res.* **40**, 1244–1260 (2001).
20. Khelassi-Sefaoui, A., Mutelet, F., Mokbel, I., Jose, J. & Negadi, L. Measurement and correlation of vapour pressures of pyridine and thiophene with [EMIM][SCN] ionic liquid. *J. Chem. Thermodyn.* **72**, 134–138 (2014).
21. Zúñiga-Moreno, A., Galicia-Luna, L. A. & Betancourt-Cárdenas, F. F. Compressed liquid densities and excess volumes of CO2 + thiophene binary mixtures from 313 to 363 K and pressures up to 25 MPa. *Fluid Phase Equilib.* **236**, 193–204 (2005).
22. Peng, Y., Goff, K. D., dos Ramos, M. C. & McCabe, C. Developing a predictive group-contribution-based SAFT-VR equation of state. *Fluid Phase Equilib.* **277**, 131–144 (2009).
23. Ma, F. & Hanna, M. A. Biodiesel production: a review1Journal Series #12109, Agricultural Research Division, Institute of Agriculture and Natural Resources, University of Nebraska–Lincoln.1. *Bioresour. Technol.* **70**, 1–15 (1999).
24. Schwab, A. W., Bagby, M. O. & Freedman, B. Preparation and properties of diesel fuels from vegetable oils. *Fuel* **66**, 1372–1378 (1987).
25. Saka, S. & Kusdiana, D. Biodiesel fuel from rapeseed oil as prepared in supercritical methanol. *Fuel* **80**, 225–231 (2001).
26. Omota, F., Dimian, A. C. & Bliek, A. Fatty acid esterification by reactive distillation. Part 1: Equilibrium-based design. *Chem. Eng. Sci.* **58**, 3159–3174 (2003).
27. Oliveira, M. B., Llovell, F., Cruz, M., Vega, L. F. & Coutinho, J. A. P. Phase equilibria description of biodiesels with water and alcohols for the optimal design of the production and purification process. *Fuel* **129**, 116–128 (2014).
28. Perdomo, F. A., Millán, B. M. & Aragón, J. L. Predicting the physical-chemical properties of biodiesel fuels assessing the molecular structure with the SAFT-γ group contribution approach. *Energy* **72**, 274–290 (2014).
29. Perdomo, F. A. & Gil-Villegas, A. Predicting thermophysical properties of biodiesel fuel blends using the SAFT-VR approach. *Fluid Phase Equilib.* **306**, 124–128 (2011).
30. Perdomo, F. A. & Gil-Villegas, A. Molecular thermodynamics of biodiesel fuel compounds. *Fluid Phase Equilib.* **293**, 182–189 (2010).
31. Oliveira, M. B., Freitas, S. V.D., Llovell, F., Vega, L. F. & Coutinho, J. A. P. Development of simple and transferable molecular models for biodiesel production with the soft-SAFT equation of state. *Chem. Eng. Res. Des.* **92**, 2898–2911 (2014).
32. Llovell, F. & Vega, L. F. Accurate modeling of supercritical CO2 for sustainable processes: Water + CO2 and CO2 + fatty acid esters mixtures. *J. Supercrit. Fluids* **96**, 86–95 (2015).
33. NguyenHuynh, D., Falaix, A., Passarello, J. P., Tobaly, P. & de Hemptinne, J. C. Predicting VLE of heavy esters and their mixtures using GC-SAFT. *Fluid Phase Equilib.* **264**, 184–200 (2008).
34. Barreau, A. *et al.* Measurements of liquid-liquid equilibria for a methanol + glycerol + methyl oleate system and prediction using group contribution statistical associating fluid

theory. *Ind. Eng. Chem. Res.* **49**, 5800–5807 (2010).
35. Nguyen Thi, T. X., Tamouza, S., Tobaly, P., Passarello, J. P. & De Hemptinne, J. C. Application of group contribution SAFT equation of state (GC-SAFT) to model phase behaviour of light and heavy esters. *Fluid Phase Equilib.* **238**, 254–261 (2005).
36. Lewandowski, G., Meissner, E. & Milchert, E. Special applications of fluorinated organic compounds. *J. Hazard. Mater.* **136**, 385–391 (2006).
37. Yee, G. G., Fulton, J. L. & Smith, R. D. Fourier transform infrared spectroscopy of molecular interactions of heptafluoro-1-butanol or 1-butanol in supercritical carbon dioxide and supercritical ethane. *J. Phys. Chem.* **96**, 6172–6181 (1992).
38. Iezzi, A., Bendale, P., Enick, R. M., Turberg, M. & Brady, J. 'Gel' Formation in Carbon Dioxide - Semifluorinated Alkane Mixtures and Phase Equilibira of a Carbon Dioxide Perfluorinated Alkane Mixture. *Fluid Phase Equilib.* **52**, 307–317 (1989).
39. Tsai, W. T. Environmental risk assessment of hydrofluoroethers (HFEs). *J. Hazard. Mater.* **119**, 69–78 (2005).
40. Sekiya, A. & Misaki, S. The potential of hydrofluoroethers to replace CFCs, HCFCs and PFCs. *J. Fluor. Chem.* **101**, 215–221 (2000).
41. Dias, A. M. A. *et al.* Vapor - Liquid equilibrium of carbon dioxide - Perfluoroalkane mixtures: Experimental data and SAFT modeling. *Ind. Eng. Chem. Res.* **45**, 2341–2350 (2006).
42. Tochigi, K. *et al.* Measurement and prediction of high-pressure vapor-liquid equilibria for binary mixtures of carbon dioxide + n-octane, methanol, ethanol, and perfluorohexane. *J. Supercrit. Fluids* **55**, 682–689 (2010).
43. Lubimbi, Z. THE INVESTIGATION OF FLUORINATED SOLVENTS FOR CARBON DIOXIDE ABSORPTION.
44. Hiaki, T., Nanao, M., Urata, S. & Murata, J. Vapor-liquid equilibria for 1,1,2,3,3,3-hexafluoropropyl, 2,2,2-trifluoroethyl ether with several organic solvents. *Fluid Phase Equilib.* **194**–**197**, 969–979 (2002).
45. Matsuda, H. *et al.* Vapor-liquid equilibria for binary systems carbon dioxide + 1,1,1,2,3,3-hexafluoro-3-(2,2,2-trifluoroethoxy)propane or 1-ethoxy-1,1,2,2,3,3,4,4,4-nonafluorobutane at 303.15–323.15 K. *Fluid Phase Equilib.* **524**, (2020).
46. Jovell, D., Gonzalez-Olmos, R. & Llovell, F. A computational drop-in assessment of hydrofluoroethers in Organic Rankine Cycles. *Energy* **254**, (2022).
47. Haley, J. D. & McCabe, C. Predicting the phase behavior of fluorinated organic molecules using the GC-SAFT-VR equation of state. *Fluid Phase Equilib.* **440**, 111–121 (2017).
48. Colina, C. M., Galindo, A., Blas, F. J. & Gubbins, K. E. Phase behavior of carbon dioxide mixtures with n-alkanes and n-perfluoroalkanes. *Fluid Phase Equilib.* **222**–**223**, 77–85 (2004).
49. Řehák, K., Klajmon, M., Strejc, M. & Morávek, P. Isothermal Vapor-Liquid Equilibria for Binary Mixtures of Methyl Nonafluorobutyl Ether + Acetone, Cyclopentyl Methyl Ether, Ethyl Acetate, n-Heptane, Methanol, and Toluene. *J. Chem. Eng. Data* **62**, 3878–3888 (2017).
50. Polishuk, I., Chiko, A., Cea-Klapp, E. & Garrido, J. M. Implementation of CP-PC-SAFT and CS-SAFT-VR-Mie for Predicting Thermodynamic Properties of C1-C3Halocarbon Systems. I. Pure Compounds and Mixtures with Nonassociating Compounds. *Ind. Eng. Chem. Res.* **60**, 9624–9636 (2021).
51. Chapman, W. G., Gubbins, K. E., Jackson, G. & Radosz, M. SAFT: Equation-of-state

solution model for associating fluids. *Fluid Phase Equilib.* **52**, 31–38 (1989).
52. Chapman, W. G., Gubbins, K. E., Jackson, G. & Radosz, M. New reference equation of state for associating liquids. *Ind. Eng. Chem. Res.* **29**, 1709–1721 (1990).
53. Wertheim, M. S. Fluids with highly directional attractive forces. I. Statistical thermodynamics. *J. Stat. Phys.* **35**, 19–34 (1984).
54. Wertheim, M. S. Fluids with highly directional attractive forces. II. Thermodynamic perturbation theory and integral equations. *J. Stat. Phys.* **35**, 35–47 (1984).
55. Wertheim, M. S. Fluids with highly directional attractive forces. III. Multiple attraction sites. *J. Stat. Phys.* **42**, 459–476 (1986).
56. Wertheim, M. S. Fluids with highly directional attractive forces. IV. Equilibrium polymerization. *J. Stat. Phys.* **42**, 477–492 (1986).
57. Huang, S. H. & Radosz, M. Equation of State for Small, Large, Polydisperse, and Associating Molecules. *Ind. Eng. Chem. Res.* **29**, 2284–2294 (1990).
58. Huang, S. H. & Radosz, M. Equation of State for Small, Large, Polydisperse, and Associating Molecules: Extension to Fluid Mixtures. *Ind. Eng. Chem. Res.* **30**, 1994–2005 (1991).
59. Chen, S. S. & Kreglewski, A. Applications of the augmented Van der Waals theory of fluids 1. Pure fluids. *J. Chim. Phys.* **81**, 1048–1052 (1977).
60. Lee, S. H., LoStracco, M. A. & McHugh, M. A. Cosolvent effect on the phase behavior of poly(ethylene-eo-acrylie acid)-butane mixtures. *Macromolecules* **29**, 1349–1358 (1996).
61. Najafloo, A., Zoghi, A. T. & Feyzi, F. Measuring solubility of carbon dioxide in aqueous blends of N-methyldiethanolamine and 2-((2-aminoethyl)amino)ethanol at low CO2 loadings and modelling by electrolyte SAFT-HR EoS. *J. Chem. Thermodyn.* **82**, 143–155 (2015).
62. Najafloo, A., Feyzi, F. & Zoghi, A. T. Modeling solubility of CO2 in aqueous MDEA solution using electrolyte SAFT-HR EoS. *J. Taiwan Inst. Chem. Eng.* **58**, 381–390 (2016).
63. Behme, S., Sadowski, G. & Arlt, W. Modeling of the separation of polydisperse polymer systems by compressed gases. *Fluid Phase Equilib.* **158**–**160**, 869–877 (1999).
64. Chen, S. J., Economou, I. G. & Rado. Density-Tuned polyolefin phase equilibria 2. multicomponent solutions of alternating poly(ethylene-propylene) in subcritical and supercritical olefins. Experiemental and SAFT model. *Macromolecules* **25**, 4987–4995 (1992).
65. Wiesmet, V., Weidner, E., Behme, S., Sadowski, G. & Arlt, W. Measurement and modelling of high-pressure phase equilibria in the systems polyethyleneglycol (PEG)-propane, PEG-nitrogen and PEG-carbon dioxide. *J. Supercrit. Fluids* **17**, 1–12 (2000).
66. Han, S. J., Gregg, C. J. & Radosz, M. How the Solute Polydispersity Affects the Cloud-Point and Coexistence Pressures in Propylene and Ethylene Solutions of Alternating Poly(ethylene-co-propylene). *Ind. Eng. Chem. Res.* **36**, 5520–5525 (1997).
67. Orbey, H., Bokis, C. P. & Chen, C. Polymer-solvent vapor-liquid equilibrium: equations of state versus activity coefficient models. **5885**, 1567–1573 (1998).
68. Najafloo, A., Feyzi, F. & Zoghi, A. T. Development of electrolyte SAFT-HR equation of state for single electrolyte solutions. *Korean J. Chem. Eng.* **31**, 2251–2260 (2014).
69. Hu, Z. Q., Yang, J. C. & Li, Y. G. Crossover SAFT equation of state for pure supercritical fluids. *Fluid Phase Equilib.* **205**, 1–15 (2003).
70. Chapman, W. G., Jackson, G. & Gubbins, K. E. Phase equilibria of associating fluids chain molecules with multiple bonding sites. *Mol. Phys.* **65**, 1057–1079 (1988).

71. Galindo, A., Whitehead, P. J., Jackson, G. & Burgess, A. N. Predicting the high-pressure phase equilibria of water + n-alkanes using a simplified SAFT theory with transferable intermolecular interaction parameters. *J. Phys. Chem.* **100**, 6781–6792 (1996).
72. Galindo, A., Whitehead, P. J., Jackson, G. & Burgess, A. N. Predicting the phase equilibria of mixtures of hydrogen fluoride with water, difluoromethane (HFC-32), and 1,1,1,2-Tetrafluoroethane (HFC-134a) using a simplified SAFT approach. *J. Phys. Chem. B* **101**, 2082–2091 (1997).
73. García-Lisbona, M. N., Galindo, A., Jackson, G. & Burgess, A. N. Predicting the high-pressure phase equilibria of binary aqueous solutions of 1-butnol, n-butoxyethanol and n-decylpentaoxyethylene ether (C10E5) using the SAFT-HS approach. *Mol. Phys.* **93**, 57–72 (1998).
74. García-Lisbona, M. N., Galindo, A., Jackson, G. & Burgess, A. N. An examination of the cloud curves of liquid-Liquid immiscibility in aqueous solutions of alkyl polyoxyethylene surfactants using the SAFT-HS approach with transferable parameters. *J. Am. Chem. Soc.* **120**, 4191–4199 (1998).
75. Andersen, J. G., Koak, N. & De Loos, T. W. Influence of pressure on the LLLE in water + n-alkyl polyoxyethylene ether + n-alkane systems. *Fluid Phase Equilib.* **163**, 259–273 (1999).
76. Clements, P. J., Hill, E. & McLure, I. A. Thermodynamics of ternary mixtures exhibiting tunnel phase behaviour: Part 2. - n-hexane-n-decane-propanenitrile. *J. Chem. Soc. - Faraday Trans.* **93**, 1325–1330 (1997).
77. Blas, F. J. & Vega, L. F. Associating Fluid Theory (SAFT) Equation of State. *Ind. Eng. Chem. Res.* **5885**, 660–674 (1998).
78. Oliveira, M. B. *et al.* Surface tension of binary mixtures of 1-alkyl-3-methylimidazolium bis(trifluoromethylsulfonyl)imide ionic liquids: Experimental measurements and soft-SAFT modeling. *J. Phys. Chem. B* **116**, 12133–12141 (2012).
79. Dowell, N. Mac *et al.* New Experimental Density Data and Soft-SAFT Models of Alkylimidazolium ([C. *J. Phys. Chem. B* **118**, 6206–6221 (2014).
80. Pena-Pereira, F. & Namieśnik, J. Ionic liquids and deep eutectic mixtures: Sustainable solvents for extraction processes. *ChemSusChem* **7**, 1784–1800 (2014).
81. Dias, A. M. A. *et al.* Densities and vapor pressures of highly fluorinated compounds. *J. Chem. Eng. Data* **50**, 1328–1333 (2005).
82. Dias, A. M. A., Llovell, F., Coutinho, J. A. P., Marrucho, I. M. & Vega, L. F. Thermodynamic characterization of pure perfluoroalkanes, including interfacial and second order derivative properties, using the crossover soft-SAFT EoS. *Fluid Phase Equilib.* **286**, 134–143 (2009).
83. Pedrosa, N., Pámies, J. C., Coutinho, J. A. P., Marrucho, I. M. & Vega, L. F. Phase equilibria of ethylene glycol oligomers and their mixtures. *Ind. Eng. Chem. Res.* **44**, 7027–7037 (2005).
84. Pàmies, J. C. & Vega, L. F. Vapor-liquid equilibria and critical behavior of heavy n-alkanes using transferable parameters from the soft-saft equation of state. *Ind. Eng. Chem. Res.* **40**, 2532–2543 (2001).
85. Blas, F. J. & Vega, L. F. Critical behavior and partial miscibility phenomena in binary mixtures of hydrocarbons by the statistical associating fluid theory. *J. Chem. Phys.* **109**, 7405–7413 (1998).
86. dos Ramos, M. C. & Blas, F. J. Theory of phase equilibria for model mixtures of n-

alkanes, perfluoroalkanes and perfluoroalkylalkane diblock surfactants. *Mol. Phys.* **105**, 1319–1334 (2007).
87. Llovell, F. & Vega, L. F. Phase equilibria, critical behavior and derivative properties of selected n-alkane/n-alkane and n-alkane/1-alkanol mixtures by the crossover soft-SAFT equation of state. *J. Supercrit. Fluids* **41**, 204–216 (2007).
88. Vega, L. F., Llovell, F. & Blas, F. J. Capturing the Solubility Minima of n-alkanes in water by soft-SAFT. *J.Phys.Chem.B* **113**, 7621–7630 (2009).
89. Pereira, L. M. C., Oliveira, M. B., Llovell, F., Vega, L. F. & Coutinho, J. A. P. Assessing the N2O/CO2 high pressure separation using ionic liquids with the soft-SAFT EoS. *J. Supercrit. Fluids* **92**, 231–241 (2014).
90. Pedrosa, N., Vega, L. F., Coutinho, J. A. P. & Marrucho, I. M. Modeling the phase equilibria of poly(ethylene glycol) binary mixtures with soft-SAFT EoS. *Ind. Eng. Chem. Res.* **46**, 4678–4685 (2007).
91. Liu, H. & Hu, Y. Molecular thermodynamic theory for polymer systems III. Equation of state for chain-fluid mixtures. *Fluid Phase Equilib.* **138**, 69–85 (1997).
92. Gross, J. & Sadowski, G. Application of the perturbed-chain SAFT equation of state to associating systems. *Ind. Eng. Chem. Res.* **41**, 5510–5515 (2002).
93. Paduszyński, K. & Domańska, U. Thermodynamic modeling of ionic liquid systems: Development and detailed overview of novel methodology based on the PC-SAFT. *J. Phys. Chem. B* **116**, 5002–5018 (2012).
94. Pavliš, J., Mathers, A., Fulem, M. & Klajmon, M. Can Pure Predictions of Activity Coefficients from PC-SAFT Assist Drug–Polymer Compatibility Screening? *Mol. Pharm.* (2023). doi:10.1021/acs.molpharmaceut.3c00124
95. Spyriouni, T., Krokidis, X. & Economou, I. G. Thermodynamics of pharmaceuticals: Prediction of solubility in pure and mixed solvents with PC-SAFT. *Fluid Phase Equilib.* **302**, 331–337 (2011).
96. Ruether, F. & Sadowski, G. Modeling the solubility of pharmaceuticals in pure solvents and solvent mixtures for drug process design. *J. Pharm. Sci.* **98**, 4205–4215 (2009).
97. Gonzalez, D. L., Vargas, F. M., Hirasaki, G. J. & Chapman, W. G. Modeling study of CO2-induced asphaltene precipitation. *Energy and Fuels* **22**, 757–762 (2008).
98. Vijande, J., Piñeiro, M. M., Bessières, D., Saint-Guirons, H. & Legido, J. L. Description of PVT behaviour of hydrofluoroethers using the PC-SAFT EOS. *Phys. Chem. Chem. Phys.* 766–770 (2004). doi:10.1039/b312223a
99. Gil-Villegas, A. *et al.* Statistical associating fluid theory for chain molecules with attractive potentials of variable range. *J. Chem. Phys.* **106**, 4168–4186 (1997).
100. McCabe, C. & Jackson, G. SAFT-VR modelling of the phase equilibrium of long-chain n-alkanes. *Phys. Chem. Chem. Phys.* **1**, 2057–2064 (1999).
101. McCabe, C., Galindo, A., García-Lisbona, M. N. & Jackson, G. Examining the adsorption (vapor-liquid equilibria) of short-chain hydrocarbons in low-density polyethylene with the SAFT-VR approach. *Ind. Eng. Chem. Res.* **40**, 3835–3842 (2001).
102. Dias, L. M. B., Filipe, E. J. M., McCabe, C. & Calado, J. C. G. Thermodynamics of liquid (xenon + methane) mixtures. *J. Phys. Chem. B* **108**, 7377–7381 (2004).
103. Morgado, P., McCabe, C. & Filipe, E. J. M. Modelling the phase behaviour and excess properties of alkane + perfluoroalkane binary mixtures with the SAFT-VR approach. in *Fluid Phase Equilibria* (2005). doi:10.1016/j.fluid.2004.08.002
104. Galindo, A., Gil-Villegas, A., Whitehead, P. J., Jackson, G. & Burgess, A. N. Prediction

of phase equilibria for refrigerant mixtures of difluoromethane (HFC-32), 1,1,1,2-tetrafluoroethane (HFC-134a), and pentafluoroethane (HFC-125a) using SAFT-VR. *J. Phys. Chem. B* **102**, 7632–7639 (1998).
105. Watson, G. *et al.* Volumetric and derivative properties under pressure for the system 1-propanol + toluene: A discussion of PC-SAFT and SAFT-VR. *Fluid Phase Equilib.* **247**, 121–134 (2006).
106. Clark, G. N. I., Galindo, A., Jackson, G., Rogers, S. & Burgess, A. N. Modeling and understanding closed-loop liquid-liquid immiscibility in aqueous solutions of polyethylene glycol using the SAFT-VR approach with transferable parameters. *Macromolecules* **41**, 6582–6595 (2008).
107. Valtz, A., Chapoy, A., Coquelet, C., Paricaud, P. & Richon, D. Vapour-liquid equilibria in the carbon dioxide-water system, measurement and modelling from 278.2 to 318.2 K. *Fluid Phase Equilib.* **226**, 333–344 (2004).
108. Clark, G. N. I., Haslam, A. J., Galindo, A. & Jackson, G. Developing optimal Wertheim-like models of water for use in Statistical Associating Fluid Theory (SAFT) and related approaches. *Mol. Phys.* **104**, 3561–3581 (2006).
109. Galindo, A. & Blas, F. J. Theoretical examination of the global fluid phase behavior and critical phenomena in carbon dioxide + n-alkane binary mixtures. *J. Phys. Chem. B* **106**, 4503–4515 (2002).
110. Sun, L., Zhao, H., Kiselev, S. B. & McCabe, C. Predicting mixture phase equilibria and critical behavior using the SAFT-VRX approach. *J. Phys. Chem. B* **109**, 9047–9058 (2005).
111. Blas, F. J. & Galindo, A. Study of the high pressure phase behaviour of CO2+n-alkane mixtures using the SAFT-VR approach with transferable parameters. *Fluid Phase Equilib.* **194**–**197**, 501–509 (2002).
112. Kouskoumvekaki, I. A., Von Solms, N., Lindvig, T., Michelsen, M. L. & Kontogeorgis, G. M. Novel method for estimating pure-component parameters for polymers: Application to the PC-SAFT equation of state. *Ind. Eng. Chem. Res.* **43**, 2830–2838 (2004).
113. Kouskoumvekaki, I. A., Von Solms, N., Michelsen, M. L. & Kontogeorgis, G. M. Application of the perturbed chain SAFT equation of state to complex polymer systems using simplified mixing rules. *Fluid Phase Equilib.* **215**, 71–78 (2004).
114. Kouskoumvekaki, I. A., Krooshof, G. J. P., Michelsen, M. L. & Kontogeorgis, G. M. Application of the Simplified PC-SAFT Equation of State to the Vapor-Liquid Equilibria of Binary and Ternary Mixtures of Polyamide 6 with Several Solvents. *Ind. Eng. Chem. Res.* **43**, 826–834 (2004).
115. Tamouza, S., Passarello, J. P., Tobaly, P. & De Hemptinne, J. C. Group contribution method with SAFT EOS applied to vapor liquid equilibria of various hydrocarbon series. *Fluid Phase Equilib.* **222**–**223**, 67–76 (2004).
116. Tamouza, S., Passarello, J. P., Tobaly, P. & De Hemptinne, J. C. Application to binary mixtures of a group contribution SAFT EOS (GC-SAFT). *Fluid Phase Equilib.* **228**–**229**, 409–419 (2005).
117. Lymperiadis, A., Adjiman, C. S., Galindo, A. & Jackson, G. A group contribution method for associating chain molecules based on the statistical associating fluid theory (SAFT- γ). *J. Chem. Phys.* **127**, (2007).
118. Lymperiadis, A., Adjiman, C. S., Jackson, G. & Galindo, A. A generalisation of the SAFT-γ group contribution method for groups comprising multiple spherical segments.

Fluid Phase Equilib. **274**, 85–104 (2008).
119. Papaioannou, V., Adjiman, C. S., Jackson, G. & Galindo, A. Simultaneous prediction of vapour-liquid and liquid-liquid equilibria (VLE and LLE) of aqueous mixtures with the SAFT-γ group contribution approach. *Fluid Phase Equilib.* **306**, 82–96 (2011).
120. Peng, Y., Goff, K. D., Dos Ramos, M. C. & McCabe, C. Predicting the phase behavior of polymer systems with the GC-SAFT-VR approach. *Ind. Eng. Chem. Res.* **49**, 1378–1394 (2010).
121. dos Ramos, M. C., Haley, J. D., Westwood, J. R. & McCabe, C. Extending the GC-SAFT-VR approach to associating functional groups: Alcohols, aldehydes, amines and carboxylic acids. *Fluid Phase Equilib.* **306**, 97–111 (2011).
122. Das, G., Ramos, M. C. dos & McCabe, C. Accurately modeling benzene and alkylbenzenes using a group contribution based SAFT approach. *Fluid Phase Equilib.* **362**, 242–251 (2014).
123. Carnahan, N. F. & Starling, K. E. Equation of state for nonattracting rigid spheres. *J. Chem. Phys.* **51**, 635–636 (1969).
124. Barker, J. A. & Henderson, D. What is 'liquid' ? Understanding the states of matter. *Rev. Mod. Phys.* **4**, (1976).
125. Leonard, P. J., Henderson, D. & Barker, J. A. Perturbation theory and liquid mixtures. *Trans. Faraday Soc.* **66**, 2439–2452 (1970).
126. Barker, J. A. & Henderson, D. Perturbation theory and equation of state for fluids. II. A successful theory of liquids. *J. Chem. Phys.* **47**, 4714–4721 (1967).
127. Barker, J. A. & Henderson, D. Perturbation theory and equation of state for fluids: The square-well potential. *J. Chem. Phys.* **47**, 2856–2861 (1967).
128. Patel, B. H., Docherty, H., Varga, S., Galindo, A. & Maitland, G. C. Generalized equation of state for square-well potentials of variable range. *Mol. Phys.* **103**, 129–139 (2005).
129. Rowlinson, J. S. Molecular Theory of Liquids and Liquid Mixtures. *Phys. Chem. Lab.* **85**, 970–979 (1981).
130. Smith, W. R., Henderson, D. & Barker, J. A. Approximate evaluation of the second-Order term in the perturbation theory of fluids. *J. Chem. Phys.* **53**, 508–515 (1970).
131. Boublik, T. Hard - Sphere Equation of State. *J. Chem. Phys.* **53**, 471–472 (1970).
132. Mansoori, G. A., Carnahan, N. F., Starling, K. E. & Leland, T. W. Equilibrium thermodynamic properties of the mixture of hard spheres. *J. Chem. Phys.* **54**, 1523–1526 (1971).
133. Ramos, M. C. Dos, Haley, J. D., Westwood, J. R. & McCabe, C. Extending the GC-SAFT-VR approach to associating functional groups: Alcohols, aldehydes, amines and carboxylic acids. *Fluid Phase Equilib.* **306**, 97–111 (2011).
134. Jackson, G., Chapman, W. G. & Gubbins, K. E. Phase equilibria of associating fluids spherical molecules with multiple bonding sites. *Mol. Phys.* **65**, 1–31 (1988).
135. Kirkpatrick, A. S. *et al.* Optimization by Simulated Annealing Published by : American Association for the Advancement of Science Stable URL : http://www.jstor.com/stable/1690046. **220**, 671–680 (1983).
136. Dolan, W. B., Cummings, P. T. & LeVan, M. D. Process optimization via simulated annealing: Application to network design. *AIChE J.* **35**, 725–736 (1989).
137. Goffe, W. L., Ferrier, G. D. & Rogers, J. Global optimization of statistical functions with simulated annealing. *J. Econom.* **60**, 65–99 (1994).
138. Metropolis, N., Rosenbluth, A. W., Rosenbluth, M. N., Teller, A. H. & Teller, E. Equation

of state calculations by fast computing machines. *J. Chem. Phys.* **21**, 1087–1092 (1953).
139. Haley, J. D. & McCabe, C. Modeling the thermodynamic properties and phase behaviour of organic sulfur molecules with a group contribution based statistical associating fluid theory approach (GC-SAFT-VR). *Fluid Phase Equilib.* **446**, 46–54 (2017).
140. Barton, T. J. *et al.* Tailored porous materials. *Chem. Mater.* **11**, 2633–2656 (1999).
141. Gelb, L., Radhakrishnan, R. & Sliwinska-Bartkowiak, M. Phase Separation in Confined Systems Article in Reports on Progress in Physics. (1999).
142. Lu, G. Q. M. & Zhao, X. S. *Nanoporous Materials: Science and Engineering*. (2004).
143. Pizio, O. Adsoprtion of Random Porous Media. in *Computational Methods in Surface and Colloid Science* 53 (2000).
144. Wong, A. P. Y. & Chan, M. H. W. Liquid-vapor critical point of He4 in aerogel. *Phys. Rev. Lett.* **65**, 2567–2570 (1990).
145. Wong, A. P. Y., Kim, S. B., Goldburg, W. I. & Chan, M. H. W. Phase separation, density fluctuation, and critical dynamics of N2 in aerogel. *Phys. Rev. Lett.* **70**, 954–957 (1993).
146. Zhuang, Z., Casielles, A. G. & Cannell, D. S. Phase diagram of isobutyric acid and water in dilute silica gel. *Phys. Rev. Lett.* **77**, 2969–2972 (1996).
147. Brennan, J. K. & Dong, W. Phase transitions of one-component fluids adsorbed in random porous media: Monte Carlo simulations. *J. Chem. Phys.* **116**, 8948–8958 (2002).
148. Madden, W. G. & Glandt, E. D. Distribution functions for fluids in random media. *J. Stat. Phys.* **51**, 537–558 (1988).
149. Madden, W. G. Fluid distributions in random media: Arbitrary matrices. *J. Chem. Phys.* **96**, 5422–5432 (1992).
150. Given, J. A. & Stell, G. Comment on: Fluid distributions in two-phase random media: Arbitrary matrices. *J. Chem. Phys.* **97**, 4573–4574 (1992).
151. Sarkisov, L. & Van Tassel, P. R. Theories of molecular fluids confined in disordered porous materials. *J. Phys. Condens. Matter* **20**, (2008).
152. Kovalenko, A. & Hirata, F. A replica reference interaction site model theory for a polar molecular liquid sorbed in a disordered microporous material with polar chemical groups. *J. Chem. Phys.* **115**, 8620–8633 (2001).
153. Chandler, D. RISM equations for fluids in quenched amorphous materials. *J. Phys. Condens. Matter* **3**, (1991).
154. Thompson, A. P. & Glandt, E. D. Adsorption of polymeric fluids in microporous materials. I. Ideal freely jointed chains. *J. Chem. Phys.* **99**, 8325–8329 (1993).
155. Trokhymchuk, A., Pizio, O., Holovko, M. & Sokolowski, S. Associative replica Ornstein-Zernike equations and the structure of chemically associating fluids in disordered porous media. *J. Mol. Liq.* **106**, 200–209 (1997).
156. Orozco, G. A., Pizio, O., Sokolowski, S. & Trokhymchuk, A. Replica Ornstein-Zernike theory for chemically associating fluids with directional forces in disordered porous media: Smith-Nezbeda model in a hard sphere matrix. *Mol. Phys.* **91**, 625–634 (1997).
157. Pizio, O., Duda, Y., Trokhymchuk, A. & Sokolowski, S. Associative replica Ornstein-Zernike equations and the structure of chemically associating fluids in disordered porous media. *J. Mol. Liq.* **76**, 183–194 (1998).
158. Padilla, P., Pizio, O., Trokhymchuk, A. & Vega, C. Adsorption of dimerizing and dimer fluids in disordered porous media. *J. Phys. Chem. B* **102**, 3012–3017 (1998).
159. Malo, B. M., Pizio, O., Trokhymchuk, A. & Duda, Y. Adsorption of a hard sphere fluid in disordered microporous quenched matrix of short chain molecules: Integral equations and

grand canonical Monte Carlo simulations. *J. Colloid Interface Sci.* **211**, 387–394 (1999).
160. Urbic, T., Vlachy, V., Pizio, O. & Dill, K. A. Water-like fluid in the presence of Lennard–Jones obstacles: predictions of an associative replica Ornstein–Zernike theory. *J. Mol. Liq.* **112**, 71–80 (2004).
161. Hribar, B., Pizio, O., Trokhymchuk, A. & Vlachy, V. Screening of ion-ion correlations in electrolyte solutions adsorbed in charged disordered matrices: Application of replica Ornstein-Zernike equations. *Condens. Matter Phys.* **107**, 6335–6341 (1997).
162. Hribar, B., Pizio, O., Trokhymchuk, A. & Vlachy, V. Ion-ion correlations in electrolyte solutions adsorbed in disordered electroneutral charged matrices from replica Ornstein-Zernike equations. *J. Chem. Phys.* **109**, 2480–2489 (1998).
163. Lukšic, M. & Hribar-Lee, B. Structure and thermodynamics of the primitive model electrolyte in a charged matrix: The evaluation of the Madden-Glandt approximation. *Condens. Matter Phys.* **16**, 1–8 (2013).
164. Hribar, B., Vlachy, V., Trokhymchuk, A. & Pizio, O. Structure and thermodynamics of asymmetric electrolytes adsorbed in disordered electroneutral charged matrices from replica Ornstein-Zernike equations. *J. Phys. Chem. B* **103**, 5361–5369 (1999).
165. Hribar, B., Vlachy, V. & Pizio, O. Structural and Thermodynamic Properties of Electrolyte Solutions in Hard-Sphere Confinement: Predictions of the Replica Integral Equation Theory. *J. Phys. Chem. B* **104**, 4479–4488 (2000).
166. Hribar, B., Vlachy, V. & Pizio, O. Equilibrium properties of a model electrolyte adsorbed in quenched disordered charged media: The ROZ theory and GCMC simulations. *J. Phys. Chem. B* **105**, 4727–4734 (2001).
167. Vlachy, V., Hribar, B. & Pizio, O. Replica integral equation theory for partly quenched electrolyte mixtures. *Phys. A Stat. Mech. its Appl.* **314**, 156–161 (2002).
168. Vlachy, V., Dominguez, H. & Pizio, O. Temperature effects in adsorption of a primitive model electrolyte in disordered quenched media: Predictions of the replica OZ/HNC approximation. *J. Phys. Chem. B* **108**, 1046–1055 (2004).
169. Lukšič, M., Hribar-Lee, B. & Vlachy, V. Electrolyte exclusion from charged adsorbent: Replica Ornstein-Zernike theory and simulations. *J. Phys. Chem. B* **111**, 5966–5975 (2007).
170. Hribar-Lee, B., Lukšiš, M. & Vlachy, V. Partly-quenched systems containing charges. Structure and dynamics of ions in nanoporous materials. *Annu. Reports Prog. Chem. - Sect. C* **107**, 14–46 (2011).
171. Lukšič, M., Vlachy, V. & Hribar-Lee, B. Modelling the ion-exchange equilibrium in nanoporous materials. *Condens. Matter Phys.* **15**, 1–12 (2012).
172. Pizio, O. & Sokolowski, S. Adsorption of fluids in confined disordered media from inhomogeneous replica Ornstein-Zernike equations. *Phys. Rev. E - Stat. Physics, Plasmas, Fluids, Relat. Interdiscip. Top.* **56**, R63–R66 (1997).
173. Kovalenko, A., Sokołowski, S., Henderson, D. & Pizio, O. Adsorption of a hard sphere fluid in a slitlike pore filled with a disordered matrix by the inhomogeneous replica Ornstein-Zernike equations. *Phys. Rev. E - Stat. Physics, Plasmas, Fluids, Relat. Interdiscip. Top.* **57**, 1824–1831 (1998).
174. Kierlik, E., Monson, P. A., Rosinberg, M. L., Sarkisov, L. & Tarjus, G. Capillary condensation in disordered porous materials: Hysteresis versus equilibrium behavior. *Phys. Rev. Lett.* **87**, 55701-1-55701–4 (2001).
175. Landers, J., Gor, G. Y. & Neimark, A. V. Density functional theory methods for

characterization of porous materials. *Colloids Surfaces A Physicochem. Eng. Asp.* **437**, 3–32 (2013).
176. Schmidt, M. Replica density functional theory: An overview. *J. Phys. Condens. Matter* **17**, (2005).
177. Kovalenko, A. & Pizio, O. The structure and adsorption of the four bonding sites model for associating fluids in disordered porous media from replica Ornstein-Zernike integral equation theory. *J. Chem. Phys.* **108**, 8651–8661 (1998).
178. Trokhymchuk, A. & Sokołowski, S. Phase coexistence and interface structure of a Lennard-Jones fluid in porous media. Application of Born-Green-Yvon equation. **109**, 5044–5049 (1998).
179. Trokhymchuk, A., Orozco, G. A., Pizio, O. & Vlachy, V. Liquid-vapor coexistence in the screened coulomb (Yukawa) hard sphere binary mixture in disordered porous media: The mean spherical approximation. *J. Colloid Interface Sci.* **207**, 379–385 (1998).
180. Krakoviack, V., Kierlik, E., Rosinberg, M. L. & Tarjus, G. Adsorption of a fluid in an aerogel: Integral equation approach. *J. Chem. Phys.* **115**, 11289–11298 (2001).
181. Patsahan, T., Trokhymchuk, A. & Holovko, M. Application of association theory to liquid/vapor coexistence in a simple fluid absorbed on porous media. *J. Mol. Liq.* **105**, 227–230 (2003).
182. Patsahan, T., Holovko, M. & Dong, W. Fluids in porous media. III. Scaled particle theory. *J. Chem. Phys.* **134**, (2011).
183. Dong, W. & Chen, X. S. Scaled particle theory for bulk and confined fluids: A review. *Sci. China Physics, Mech. Astron.* **61**, (2018).
184. Holovko, M., Patsahan, T. & Dong, W. Fluids in random porous media: Scaled particle theory. *Pure Appl. Chem.* **85**, 115–133 (2013).
185. Qiao, C. Z., Zhao, S. L., Liu, H. L. & Dong, W. Connect the Thermodynamics of Bulk and Confined Fluids: Confinement-Adsorption Scaling. *Langmuir* **35**, 3840–3847 (2019).
186. Holovko, M. F., Patsahan, T. M. & Shmotolokha, V. I. What is liquid in random porous media: The Barker-Henderson perturbation theory. *Condens. Matter Phys.* **18**, 1–17 (2015).
187. Hvozd, T. V. & Kalyuzhnyi, Y. V. Two- and three-phase equilibria of polydisperse Yukawa hard-sphere fluids confined in random porous media: high temperature approximation and scaled particle theory. *Soft Matter* **13**, 1405–1412 (2017).
188. Kalyuzhnyi, Y. V., Holovko, M., Patsahan, T. & Cummings, P. T. Phase behavior and percolation properties of the patchy colloidal fluids in the random porous media. *J. Phys. Chem. Lett.* **5**, 4260–4264 (2014).
189. Hvozd, T. V., Kalyuzhnyi, Y. V. & Cummings, P. T. Phase Equilibria of Polydisperse Square-Well Chain Fluid Confined in Random Porous Media: TPT of Wertheim and Scaled Particle Theory. *J. Phys. Chem. B* **122**, 5458–5465 (2018).
190. Holovko, M., Patsahan, T. & Patsahan, O. Effects of disordered porous media on the vapour-liquid phase equilibrium in ionic fluids: application of the association concept. *J. Mol. Liq.* **228**, 215–223 (2017).
191. Holovko, M. F., Patsahan, O. & Patsahan, T. Vapour-liquid phase diagram for an ionic fluid in a random porous medium. *J. Phys. Condens. Matter* **28**, (2016).
192. Page, K. S. & Monson, P. A. Monte Carlo calculations of phase diagrams for a fluid confined in a disordered porous material. *Phys. Rev. E - Stat. Physics, Plasmas, Fluids, Relat. Interdiscip. Top.* **54**, 6557–6564 (1996).

193. Page, K. S. & Monson, P. A. Phase equilibrium in a molecular model of a fluid confined in a disordered porous material. *Phys. Rev. E - Stat. Physics, Plasmas, Fluids, Relat. Interdiscip. Top.* **54**, R29–R32 (1996).
194. Álvarez, M., Levesque, D. & Weis, J. J. Monte Carlo approach to the gas-liquid transition in porous materials. *Phys. Rev. E - Stat. Physics, Plasmas, Fluids, Relat. Interdiscip. Top.* **60**, 5495–5504 (1999).
195. Sarkisov, L. & Monson, P. A. Computer simulations of phase equilibrium for a fluid confined in a disordered porous structure. *Phys. Rev. E - Stat. Physics, Plasmas, Fluids, Relat. Interdiscip. Top.* **61**, 7231–7234 (2000).
196. De Grandis, V., Gallo, P. & Rovere, M. Computer simulation of the phase diagram for a fluid confined in a fractal and disordered porous material. *Phys. Rev. E - Stat. Physics, Plasmas, Fluids, Relat. Interdiscip. Top.* **70**, 7 (2004).
197. Brennan, J. K. & Dong, W. Molecular simulation of the vapor-liquid phase behavior of Lennard-Jones mixtures in porous solids. *Phys. Rev. E - Stat. Physics, Plasmas, Fluids, Relat. Interdiscip. Top.* **67**, 6 (2003).
198. Kumar, A. N. & Singh, J. K. The effects of interaction range, porosity anf molecular association on the phase equilibrium of a fluid confined in a disordered porous media. *Mol. Phys.* **106**, 2277–2288 (2008).
199. Hvozd, T. V. & Kalyuzhnyi, Y. V. Second-order Barker-Henderson perturbation theory for the phase behavior of polydisperse Morse hard-sphere mixture. *Condens. Matter Phys.* **18**, 1–13 (2015).
200. Blum, L. & Høye, J. S. Mean spherical model for asymmetric electrolytes. 2. Thermodynamic properties and the pair correlation function. *J. Phys. Chem.* **81**, 1311–1316 (1977).
201. Allen, M. P. & Tildesley, D. J. *Computer Simulation of Liquid*. (Oxford University Press, 2017).
202. Vakarin, E. V., Dong, W. & Badiali, J. P. On the double phase-transition of fluids adsorbed in disordered porous media. *Phys. A Stat. Mech. its Appl.* **379**, 389–400 (2007).
203. Freitas, S. V.D. *et al.* Measurement and prediction of speeds of sound of fatty acid ethyl esters and ethylic biodiesels. *Fuel* **108**, 840–845 (2013).
204. Javadli, R. & de Klerk, A. Desulfurization of heavy oil. *Appl. Petrochem. Res.* **1**, 3–19 (2012).
205. Chen, Y., Mutelet, F. & Jaubert, J. N. Experimental measurement and modeling of phase diagrams of binary systems encountered in the gasoline desulfurization process using ionic liquids. *J. Chem. Eng. Data* **59**, 603–612 (2014).
206. DIPPR, B. Design Institute for Physical Property Data (U.S.) and Knovel (Firm). (2005).
207. Rose, A. & Schrodt, V. N. Vapor-Liquid Equilibria for the Methyl Oleate and Methyl Stearate Binary System. *J. Chem. Eng. Data* **9**, 12–16 (1964).
208. Bonhorst, C. W., Althouse, P. M. & Triebold, H. O. OF C6 TO C18 SATURATED FATTY ACIDS Esters of Naturally Occurring Fatty Acids. (1948).
209. Pratas, M. J. *et al.* Densities and viscosities of minority fatty acid methyl and ethyl esters present in biodiesel. *J. Chem. Eng. Data* **56**, 2175–2180 (2011).
210. Inomata, H. *et al.* Vapour-liquid equilibria for binary mixtures of carbon dioxide and fatty acid methyl esters. *Fluid Phase Equilib.* **46**, 41–52 (1989).
211. Sapei, E. *et al.* Vapor-liquid equilibrium for binary system of 1-propanethiol, thiophene, and diethyl sulfide with toluene at 90.03 kPa. *J. Chem. Eng. Data* **51**, 1372–1376 (2006).

212. Bai, J., Guo, B., Xia, S., Li, Y. & Ma, P. Isobaric vapor-liquid equilibrium for four binary systems of thiophene. *Fluid Phase Equilib.* **315**, 84–90 (2012).
213. Yamamuro, O., Suga, H., Usui, Y., Kimura, T. & Takagi, S. Thermodynamic functions of the thiophene-benzene system in their liquid and solid solutions. *J. Phys. Chem. B* **101**, 6541–6548 (1997).
214. Triday, J. O. Vapor-Liquid Equilibria in Binary Systems Formed by Thiophene and Light Alcohols. *J. Chem. Eng. Data* **28**, 307–310 (1983).
215. Toghiani, H., Toghiani, R. K. & Viswanath, D. S. Vapor-Liquid Equilibria for the Methanol-Benzene and Methanol-Thiophene Systems. 63–67 (1994).
216. Maciejewski, A. The application of perfluoroalkanes as solvents in spectral, photophysical and photochemical studies. *J. Photochem. Photobiol. A Chem.* **51**, 87–131 (1990).
217. Kirk, K. L. Fluorine in medicinal chemistry: Recent therapeutic applications of fluorinated small molecules. *J. Fluor. Chem.* **127**, 1013–1029 (2006).
218. Cui, S. T., Cochran, H. D. & Cummings, P. T. Vapor-liquid phase coexistence of alkane-carbon dioxide and perfluoroalkane-carbon dioxide mixtures. *J. Phys. Chem. B* **103**, 4485–4491 (1999).
219. Muñoz-Rujas, N., Rubio-Pérez, G., Montero, E. A. & Aguilar, F. Isobaric Vapor-Liquid Equilibria at 50.0, 101.3, and 200.0 kPa. Density and Speed of Sound at 101.3 kPa and 298.15 K of Binary Mixtures HFE-7100 + 2-Propanol. *J. Chem. Eng. Data* **65**, 4290–4298 (2020).
220. Hiaki, T., Nanao, M., Urata, S. & Murata, J. Vapor-liquid equilibrai for 1,1,2,2-tetrafluoroethyl, 2,2,2-trifluoroethyl ether with several organic compounds containing oxygen. **182**, 189–198 (2001).
221. Lai, N. A., Vrabec, J., Raabe, G., Fischer, J. & Wendland, M. Description of HFO-1234yf with BACKONE equation of state. *Fluid Phase Equilib.* **305**, 204–211 (2011).
222. McCabe, C., Galindo, A., Gil-Villegas, A. & Jackson, G. Predicting the high-pressure phase equilibria of binary mixtures of perfluoro-n-alkanes + n-alkanes using the SAFT-VR approach. *J. Phys. Chem. B* **102**, 8060–8069 (1998).
223. Morgado, P. *et al.* Liquid phase behavior of perfluoroalkylalkane surfactants. *J. Phys. Chem. B* **111**, 2856–2863 (2007).
224. Vinš, V. *et al.* Surface tension and density of dielectric heat transfer fluids of HFE type-experimental data at 0.1 MPa and modeling with PC-SAFT equation of state and density gradient theory. *Int. J. Refrig.* **131**, 956–969 (2021).
225. Blas, F. J. & Vega, L. F. Thermodynamic behavious of homonuclear and heteronuclear Lennard-Jones chains with association sites from simulation and theory. *Mol. Phys.* **92**, 135–150 (1997).
226. Westhaus, U., Droge, T. & Sass, R. DETHERM® - A thermophysical property database. *Fluid Phase Equilib.* **158**–**160**, 429–435 (1999).
227. Thomson, G. H. The DIPPR databases. *Int. J. Thermophys.* **17**, 223–232 (1996).
228. Morgado, P. *et al.* Systems involving hydrogenated and fluorinated chains: Volumetric properties of perfluoroalkanes and perfluoroalkylalkane surfactants. *J. Phys. Chem. B* **115**, 15013–15023 (2011).
229. Morgado, P., Barras, J., Galindo, A., Jackson, G. & Filipe, E. J. M. Modeling the Fluid-Phase Equilibria of Semifluorinated Alkanes and Mixtures of (n-Alkanes + n-Perfluoroalkanes) with the SAFT-γMie Group-Contribution Approach. *J. Chem. Eng. Data* **65**, 5909–5919 (2020).

230. Yasumoto, M., Yamada, Y., Murata, J., Urata, S. & Otake, K. Critical Parameters and Vapor Pressure Measurements of Hydrofluoroethers at High Temperatures. *J. Chem. Eng. Data* **48**, 1368–1379 (2003).
231. Duce, C., Tinè, M. R., Lepori, L. & Matteoli, E. VLE and LLE of perfluoroalkane + alkane mixtures. *Fluid Phase Equilib.* **199**, 197–212 (2002).
232. Simons, J. H. & Mausteller, J. W. The Properties of n -Butforane and Its Mixtures with n -Butane. *J. Chem. Phys.* **20**, 1516–1519 (1952).
233. Subramoney, S. C. *et al.* Experimental (vapour + liquid) equilibrium data and modelling for binary mixtures of decafluorobutane with propane and 1-butene. *J. Chem. Thermodyn.* **67**, 134–142 (2013).
234. Dias, A. M. A., Pàmies, J. C., Coutinho, J. A. P., Marrucho, I. M. & Vega, L. F. SAFT modeling of the solubility of gases in perfluoroalkanes. *J. Phys. Chem. B* **108**, 1450–1457 (2004).
235. De Melo, M. J. P. *et al.* Liquid-liquid equilibrium of (perfluoroalkane + alkane) binary mixtures. *Fluid Phase Equilib.* **242**, 210–219 (2006).
236. Bedford, R. G. & Dunlap, R. D. Solubilities and Volume Changes Attending Mixing for the System: Perfluoro-n-hexane–n-Hexane. *J. Am. Chem. Soc.* **80**, 282–285 (1958).
237. dos Ramos, M. C., Docherty, H., Blas, F. J. & Galindo, A. Application of the generalised SAFT-VR approach for long-ranged square-well potentials to model the phase behaviour of real fluids. *Fluid Phase Equilib.* **276**, 116–126 (2009).
238. Uchida, Y. *et al.* Critical properties of four HFE + HFC binary systems: Trifluoromethoxymethane (HFE-143m) + pentafluoroethane (HFC-125), + 1,1,1,2-tetrafluoroethane (HFC-134a), + 1,1,1,2,3,3,3-heptafluoropropane (HFC-227ea), and + 1,1,1,2,3,3-hexafluoropropane (HFC-236ea). *J. Chem. Eng. Data* **49**, 1615–1621 (2004).
239. Fang, D., Li, Y., Meng, X. & Wu, J. Liquid density of HFE-7200 and HFE-7500 from T = (283 to 363) K at pressures up to 100 MPa. *J. Chem. Thermodyn.* **69**, 36–42 (2014).
240. Rausch, M. H., Kretschmer, L., Will, S., Leipertz, A. & Fröba, A. P. Density, surface tension, and kinematic viscosity of hydrofluoroethers HFE-7000, HFE-7100, HFE-7200, HFE-7300, and HFE-7500. *J. Chem. Eng. Data* **60**, 3759–3765 (2015).
241. Albà, C. G., Vega, L. F. & Llovell, F. A consistent thermodynamic molecular model of n-hydrofluoroolefins and blends for refrigeration applications. *Int. J. Refrig.* **113**, 145–155 (2020).
242. Fouad, W. A. & Vega, L. F. Next generation of low global warming potential refrigerants: Thermodynamic properties molecular modeling. *AIChE J.* **64**, 250–262 (2018).
243. Nekså, P. CO2 heat pump systems. *Int. J. Refrig.* **25**, 421–427 (2002).
244. Poling, B. E., Prausnitz, J. M. & O'Connell, J. P. *The Properties of Gases and Liquids*. (McGraw-Hill, 2001).
245. Akasaka, R. Applications of the simple multi-fluid model to correlations of the vapor-liquid equilibrium of refrigerant mixtures containing carbon dioxide. *J. Therm. Sci. Technol.* **4**, 159–168 (2009).
246. Djebaili, K., El Ahmar, E., Valtz, A., Meniai, A. H. & Coquelet, C. Vapor-Liquid Equilibrium Data for the Carbon Dioxide (CO2) + 1,1,1,3,3-Pentafluorobutane (R365mfc) System at Temperatures from 283.15 to 337.15 K. *J. Chem. Eng. Data* **63**, 4626–4631 (2018).
247. Silva-Oliver, G. & Galicia-Luna, L. A. Vapor-liquid equilibria for carbon dioxide + 1,1,1,2-tetrafluoroethane (R-134a) systems at temperatures from 329 to 354 K and

pressures upto 7.37 MPa. *Fluid Phase Equilib.* **199**, 213–222 (2002).
248. Duran-Valencia, C., Pointurier, G., Valtz, A., Guilbot, P. & Richon, D. Vapor-liquid equilibrium (VLE) data for the carbon dioxide (CO2) + 1,1,1,2-tetrafluoroethane (R134a) system at temperatures from 252.95 K to 292.95 K and pressures up to 2 MPa. *J. Chem. Eng. Data* **47**, 59–61 (2002).
249. Lim, J. S., Jin, J. M. & Yoo, K. P. VLE measurement for binary systems of CO2 + 1,1,1,2-tetrafluoroethane (HFC-134a) at high pressures. *J. Supercrit. Fluids* **44**, 279–283 (2008).
250. Kim, S. A., Lim, J. S. & Kang, J. W. Isothermal vapor-liquid equilibria for the binary system of carbon dioxide (CO2) + 1,1,1,2,3,3,3-Heptafluoropropane (R-227ea). *J. Chem. Eng. Data* **55**, 4999–5003 (2010).
251. Raabe, G. Molecular simulation studies on the vapor-liquid phase equilibria of binary mixtures of R-1234yf and R-1234ze(E) with R-32 and CO2. *J. Chem. Eng. Data* **58**, 1867–1873 (2013).
252. Gornati, S. A., Di Bona, D. & Chiesa, P. New experimental VLE data for the binary mixture of carbon dioxide + perfluorohexane (CO2 + C6F14) from 273 K to 333 K. *Fluid Phase Equilib.* **498**, 94–103 (2019).
253. Urata, S., Takada, A., Uchimaru, T. & Chandra, A. K. Rate constants estimation for the reaction of hydrofluorocarbons and hydrofluoroethers with OH radicals. *Chem. Phys. Lett.* **368**, 215–223 (2003).
254. Deka, R. C. & Mishra, B. K. Theoretical studies on kinetics, mechanism and thermochemistry of gas-phase reactions of HFE-449mec-f with OH radicals and Cl atom. *J. Mol. Graph. Model.* **53**, 23–30 (2014).
255. 3M Novec 7200 Engineered Fluid Datasheet.
256. Peng, D. Y. & Robinson, D. B. A New Two-Constant Equation of State. *Ind. Eng. Chem. Fundam.* **15**, 59–64 (1976).
257. Wong, D. S. H. & Sandler, S. I. A theoretically correct mixing rule for cubic equations of state. *AIChE J.* **38**, 671–680 (1992).
258. H., R. & J.M., P. Local Compositions in Thermodynamic Excess Functions for Liquid Mixtures. *AICHE J.* **14**, 135–144 (1968).
259. Silva, G. M. C. *et al.* Vapor pressure and liquid density of fluorinated alcohols: Experimental, simulation and GC-SAFT-VR predictions. *Fluid Phase Equilib.* **425**, 297–304 (2016).
260. Emami, F. S., Vahid, A., Richard Elliott, J. & Feyzi, F. Group contribution prediction of vapor pressure with statistical associating fluid theory, perturbed-chain statistical associating fluid theory, and elliott-suresh-donohue equations of state. *Ind. Eng. Chem. Res.* **47**, 8401–8411 (2008).
261. Avendaño, C. *et al.* SAFT-γ force field for the simulation of molecular fluids: 2. Coarse-grained models of greenhouse gases, refrigerants, and long alkanes. *J. Phys. Chem. B* **117**, 2717–2733 (2013).
262. Muñoz-Rujas, N., Aguilar, F., García-Alonso, J. M. & Montero, E. A. Thermodynamics of binary mixtures 1-ethoxy-1,1,2,2,3,3,4,4,4-nonafluorobutane (HFE-7200) + 2-propanol: High pressure density, speed of sound and derivative properties. *J. Chem. Thermodyn.* **131**, 630–647 (2019).
263. Grubbs, G. S. & Cooke, S. A. Conformational energies of C4F9/OC2H 5 (HFE-7200). *Chem. Phys. Lett.* **495**, 182–186 (2010).

264. Bravo, I. *et al.* Atmospheric chemistry of C4F9OC2H 5 (HFE-7200), C4F9OCH3 (HFE-7100), C3F7OCH3 (HFE-7000) and C3F 7CH2OH: Temperature dependence of the kinetics of their reactions with OH radicals, atmospheric lifetimes and global warming potentials. *Phys. Chem. Chem. Phys.* **12**, 5115–5125 (2010).
265. Shiflett, M. B. & Yokozeki, A. Liquid-liquid equilibria of hydrofluoroethers and ionic liquid 1-ethyl-3-methylimidazolium bis(trifluoromethvlsulfonvl)imide. *J. Chem. Eng. Data* **52**, 2413–2418 (2007).
266. Tochigi, K. *et al.* Vapor-liquid equilibrium data for the six binaries heptafluoropropyl methyl ether (HFE-347mcc) or 1,1,1,2,3,3-hexafluoro-3-propane (HFE-449mec-f) with 1-propanol, 2-butanone, or ethyl acetate. *J. Chem. Eng. Data* **47**, 830–834 (2002).
267. The Dortmund Data Bank (DDB), DDBST Software and Separation Technology.
268. Peng, Y., Zhao, H. & McCabe, C. On the thermodynamics of diblock chain fluids from simulation and heteronuclear statistical associating fluid theory for potentials of variable range. *Mol. Phys.* **104**, 571–586 (2006).
269. Scott, R. L. & van Konynenburg, P. H. Van der Waals and Related Models for Hydrocarbon Mixtures. *Discuss. Faraday Soc.* **49**, 87–97 (1970).
270. Kiselev, S. B. & Ely, J. F. Crossover SAFT equation of state: Application for normal alkanes. *Ind. Eng. Chem. Res.* **38**, 4993–5004 (1999).
271. McCabe, C. & Kiselev, S. B. A crossover SAFT-VR equation of state for pure fluids: Preliminary results for light hydrocarbons. *Fluid Phase Equilib.* **219**, 3–9 (2004).
272. McCabe, C. & Kiselev, S. B. Application of crossover theory to the SAFT-VR equation of state: SAFT-VRX for pure fluids. *Ind. Eng. Chem. Res.* **43**, 2839–2851 (2004).
273. Lazzaroni, M. J., Bush, D., Brown, J. S. & Eckert, C. A. High-pressure vapor-liquid equilbria of some carbon dioxide + organic binary systems. *J. Chem. Eng. Data* **50**, 60–65 (2005).
274. Kobatake, B. Y. & Hildebrand, J. H. Solubility and entropy of solution of He, N2, A, O2, CH4, C2H6, CO2 and SF6 in various solvents: Regularity of gas solubilities. *J. Phys. Chem.* **65**, 331–335 (1961).
275. Zhang, N., Hu, P., Chen, L. X., Liu, M. H. & Chen, Q. Measurements of Critical Properties of the Binary Mixture of 1,1,1-Trifluoroethane (HFC-143a) +trans-1,3,3,3-Tetrafluoropropene (HFO-1234ze(E)). *J. Chem. Eng. Data* **66**, 2717–2722 (2021).
276. Gruzdev, V. A., Khairulin, R. A., Komarov, S. G. & Stankus, S. V. Thermodynamic Properties of HFC-227ea. **23**, (2002).
277. Gruzdev, V. A., Khairulin, R. A., Komarov, S. G. & Stankus, S. V. Thermodynamic properties of HFC-236ea. *Int. J. Thermophys.* **29**, 546–556 (2008).
278. Maezawa, Y., Sato, H. & Watanabe, K. Liquid Densities and Vapor Pressures of 1-Chloro-1,1-dlfluoroethane (HCFC 142b). *J. Chem. Eng. Data* **36**, 148–150 (1991).
279. Maezawa, Y., Sato, H. & Watanabe, K. Saturated Liquid Densities of HCFC 123 and HFC 134a. *J. Chem. Eng. Data* **35**, 225–228 (1990).
280. Defibaugh, D. R. *et al.* Thermodynamic Properties of HFC-338mccq, CF3CF2CF2CH2F, 1,1,1,2,2,3,3,4-Octafluorobutane. **42**, 488–496 (1997).
281. Tanaka, K. & Higashi, Y. Thermodynamic properties of HFO-1234yf (2,3,3,3-tetrafluoropropene). *Int. J. Refrig.* **33**, 474–479 (2010).
282. Katsuyuki, T. Measurements of Vapor Pressure and Saturated Liquid Density for HFO-1234ze(E) and HFO-1234ze(Z). *J. Chem. Eng. Data* **61**, 1645–1648 (2016).
283. Devotta, S., Gopichand, S. & Rao Pendyala, V. Comparative assessment of some HCFCs,

HFCs and HFEs as alternatives to CFC11. *Int. J. Refrig.* **17**, 32–39 (1994).
284. Devotta, S. & Rao Pendyala, V. Thermodynamic screening of some HFCs and HFEs for high-temperature heat pumps as alternatives to CFC114. *Int. J. Refrig.* **17**, 338–342 (1994).
285. Tochigi, K. *et al.* Determination of ASOG parameters for selecting azeotropic mixtures containing hydrofluoroethers. *Fluid Phase Equilib.* **194**–**197**, 653–662 (2002).
286. Tochigi, K. *et al.* Prediction of vapor-liquid equilibrium for systems containing hydrofluoroethers using ASOG group contribution method. *Fluid Phase Equilib.* **183**–**184**, 173–182 (2001).
287. Goharshadi, E. K. & Moosavi, F. Prediction of thermodynamic properties of some hydrofluoroether refrigerants using a new equation of state. *Fluid Phase Equilib.* **238**, 112–119 (2005).
288. Urata, S., Takada, A., Murata, J., Hiaki, T. & Sekiya, A. Prediction of vapor-liquid equilibrium for binary systems containing HFEs by using artificial neural network. *Fluid Phase Equilib.* **199**, 63–78 (2002).
289. Hou, S. X., Duan, Y. Y. & Wang, X. D. Vapor-liquid equilibria predictions for alternative working fluids at low and moderate pressures. *Ind. Eng. Chem. Res.* **47**, 7501–7508 (2008).
290. Linstrom, P. J. & Mallard, W. G. *NIST Webbook, NIST Standard Reference Database Number 69*. (National Institute of Standards and Technology). doi:https://doi.org/10.18434/T4D303
291. Company, 3M. Technical Data 3M Novec 7000 engineered fluid product information. Available at: https://multimedia.3m.com/mws/media/121372O/3m-novec-7000-engineered-fluid-tds.pdf. (Accessed: 15th September 2022)
292. Company, 3M. Technical Data 3M Novec 7100 engineered fluid product information. Available at: https://multimedia.3m.com/mws/media/199818O/3m-novec-7100-engineered-fluid.pdf. (Accessed: 15th September 2022)
293. Company, 3M. Technical Data 3M Novec 7200 engineered fluid product information.
294. Lafitte, T., Bessieres, D., Piñeiro, M. M. & Daridon, J. L. Simultaneous estimation of phase behavior and second-derivative properties using the statistical associating fluid theory with variable range approach. *J. Chem. Phys.* **124**, (2006).
295. Kho, Y. W., Conrad, D. C. & Knutson, B. L. Phase equilibria and thermophysical properties of carbon dioxide-expanded fluorinated solvents. *Fluid Phase Equilib.* **206**, 179–193 (2003).